Quantum interference effects in attosecond photoionization dynamics

Busto, David

2020

Quantum interference effects in attosecond photoionization dynamics

DAVID BUSTO
PHYSICS DEPARTMENT | FACULTY OF ENGINEERING | LUND UNIVERSITY

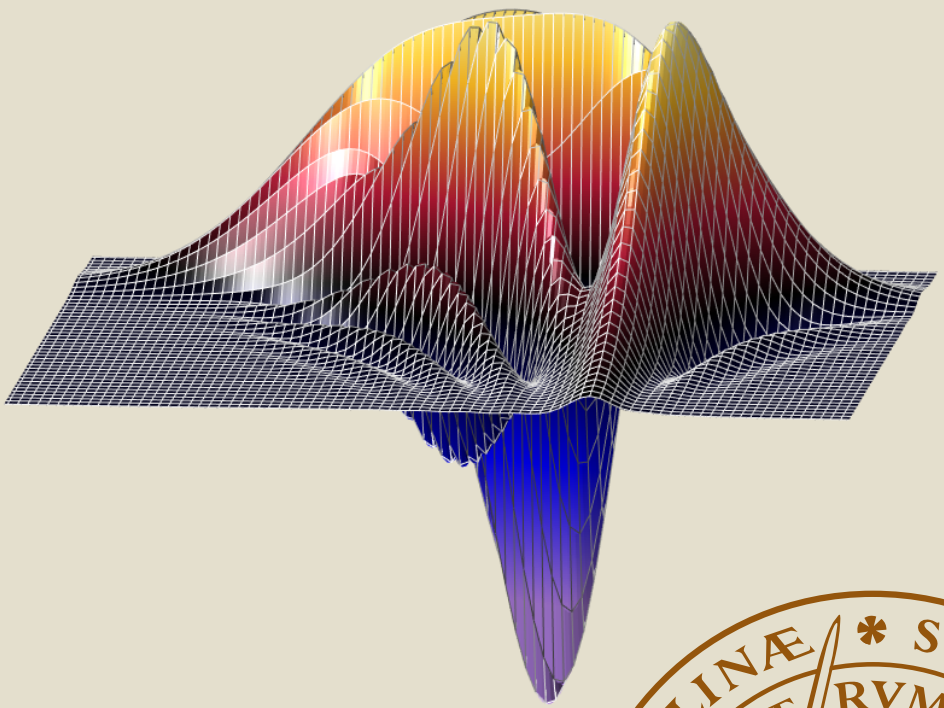

Quantum interference effects in attosecond photoionization dynamics

Quantum interference effects in attosecond photoionization dynamics

by David Busto

LUND
UNIVERSITY

Thesis for the degree of Doctor of Philosophy
Thesis advisors: Prof. Anne L'Huillier, Dr. Mathieu Gisselbrecht,
Dr. Jan Marcus Dahlström
Faculty opponent: Prof. Lars Bojer Madsen

To be presented, with the permission of the Faculty of Engineering, LTH of Lund University, for public criticism in the Rydberg lecture hall (Rydbergsalen) at the Physics Department on Friday, the 28th of August 2020 at 9:00.

Quantum interference effects in attosecond photoionization dynamics

by David Busto

LUND
UNIVERSITY

Organization	Document name
LUND UNIVERSITY Physics Department Box 118 SE–221 00 LUND Sweden	**DOCTORAL DISSERTATION** Date of disputation 2020-08-28 Sponsoring organization
Author(s) David Busto	

Title and subtitle
Quantum interference effects in attosecond photoionization dynamics:

Abstract
The interaction of extreme ultraviolet light with matter can lead to the emission of an electron in a process known as photoionization. The electron wavepacket (EWP) created in the continuum propagates on the ionic potential, resulting in a delay compared to an EWP propagating freely. The development of extreme ultraviolet attosecond light sources in recent years has opened the possibility to probe photoionization on the attosecond time scale (10^{-18} s).

In this thesis, atomic photoionization is investigated in both resonant and non-resonant conditions via the attosecond photoelectron interferometric technique RABBIT (Reconstruction of Attosecond Beating By Interference of Two-photon transitions). Atoms are photoionized by an attosecond pulse train (APT), creating an EWP in the continuum. The EWP is then made to interfere with itself using a weak delayed infrared (IR) probe pulse. Recording the photoelectron signal as a function of the delay between the IR and the APT allows us to characterize the EWP in the spectral domain.

In this thesis we investigate experimentally and theoretically photoionization dynamics in various atoms (He, Ne, Ar and Xe) as well as in the N_2 molecule. These studies focus on understanding how the presence of multiple ionization channels affects the ionization dynamics. On the one hand, we study the situation in which different ionization channels are excited incoherently resulting in overlapping photoelectron peaks in the spectrum. In this case, we show that the RABBIT technique allows us to measure photoionization time delays with a few tens of attosecond resolution while maintaining the high spectral resolution needed to disentangle contributions from different ionization channels. On the other hand, we investigate the case where several ionization channels are excited coherently leading to interference between different quantum paths. Using the RABBIT technique, we study the interference between direct photoionization and autoionization in the vicinity of Fano resonances. Measuring the amplitude and phase of photoelectrons emitted via these resonances, we characterize the EWPs in time-frequency domain. By pushing the spectral resolution of our measurements we are able to observe signatures of quantum decoherence and to quantify it. In addition, using angle-resolved measurements, we investigate the effect of the coherent superposition of final states with different angular momenta. We show that it results in angular interference which lead to an angle-dependence of the photoionization time delays and to a modification of the photoelectron angular distribution with pump-probe delay.

Key words
Attosecond, Photoionization, Interferometry

Classification system and/or index terms (if any)

Supplementary bibliographical information		Language English
ISSN and key title 0281-2762		ISBN 978-91-7895-559-6 (print) 978-91-7895-560-2 (pdf)
Recipient's notes	Number of pages 280	Price
	Security classification	

A doctoral thesis at a university in Sweden takes either the form of a single, cohesive research study (monograph) or a summary of research papers (compilation thesis), which the doctoral student has written alone or together with one or several other author(s).

In the latter case the thesis consists of two parts. An introductory text puts the research work into context and summarizes the main points of the papers. Then, the research publications themselves are reproduced, together with a description of the individual contributions of the authors. The research papers may either have been already published or are manuscripts at various stages (in press, submitted, or in draft).

Cover illustration front: Wigner distribution of an electron wavepacket emitted via an autoionizing resonance in helium

Cover illustration back: Raw VMI image of the XUV+IR photoelectron angular distribution when harmonic 15 is resonant with a Rydberg state in helium.

Funding information: Swedish Research Council, European Research Council, Knut and Alice Wallenberg Foundation

Faculty of Engineering, LTH, Physics Department

ISBN: 978-91-7895-559-6 (print)
ISBN: 978-91-7895-560-2 (pdf)
ISSN : 0281-2762

Printed in Sweden by Media-Tryck, Lund University, Lund 2020

Abstract

The interaction of extreme ultraviolet light with matter can lead to the emission of an electron in a process known as photoionization. The electron wavepacket (EWP) created in the continuum propagates on the ionic potential, resulting in a delay compared to an EWP propagating freely. The development of extreme ultraviolet attosecond light sources in recent years has opened the possibility to probe photoionization on the attosecond time scale (10^{-18} s).

In this thesis, atomic photoionization is investigated in both resonant and non-resonant conditions via the attosecond photoelectron interferometric technique RABBIT (Reconstruction of Attosecond Beating By Interference of Two-photon transitions). Atoms are photoionized by an attosecond pulse train (APT), creating an EWP in the continuum. The EWP is then made to interfere with itself using a weak delayed infrared (IR) probe pulse. Recording the photoelectron signal as a function of the delay between the IR and the APT allows us to characterize the EWP in the spectral domain.

In this thesis we investigate experimentally and theoretically photoionization dynamics in various atoms (He, Ne, Ar and Xe) as well as in the N_2 molecule. These studies focus on understanding how the presence of multiple ionization channels affects the ionization dynamics. On the one hand, we study the situation in which different ionization channels are excited incoherently resulting in overlapping photoelectron peaks in the spectrum. In this case, we show that the RABBIT technique allows us to measure photoionization time delays with a few tens of attosecond resolution while maintaining the high spectral resolution needed to disentangle contributions from different ionization channels. On the other hand, we investigate the case where several ionization channels are excited coherently leading to interference between different quantum paths. Using the RABBIT technique, we study the interference between direct photoionization and autoionization in the vicinity of Fano resonances. Measuring the amplitude and phase of photoelectrons emitted via these resonances, we characterize the EWPs in time-frequency domain. By pushing the spectral resolution of our measurements we are able to observe signatures of quantum decoherence and to quantify it. In addition, using angle-resolved measurements, we investigate the effect of the coherent superposition of final states with different angular momenta. We show that it results in angular interference which lead to an angle-dependence of the photoionization time delays and to a modification of the photoelectron angular distribution with pump-probe delay.

Popular scientific summary

Quantum interference effects in attosecond photoionization dynamics... "Great! I don't even understand the title." If that's what you are thinking, this section is for you.

Shooting at atoms with light

All matter around us is made of the same thing: atoms. These atoms, whose size is of the order of 0.1 nanometers, are themselves made of a tiny nucleus around which orbit electrons, a bit like the planets orbit around the sun. Now, if you shoot at the atom with high energy light, such as extreme ultraviolet light or X-rays, an electron might absorb the light and be ejected from the atom. This is what is called photoelectric effect or photoionization. This thesis aims at studying how electrons are ejected from atoms following the absorption of light. The problem is that this process is extremely fast, millions of times faster than the fastest electronics. The time scale of electronic motion is that of attoseconds, where one attosecond is a billionth of a billionth of a second, or 10^{-18} seconds. In addition to this, contrary to the planets orbiting the sun, the laws that describe how electrons move are not the laws of classical physics that we all experience in our everyday life. The microcosm of electrons and atoms is described by quantum mechanics.

There are two concepts of quantum mechanics that are essential to this thesis. The first one is the superposition principle. This principle states that an electron does not have be here *or* there, it can be here *and* there, at the same time. The second concept is that of wave-particle duality. It means that particles like electrons can also behave like waves. Waves are characterized by three quantities: amplitude, phase and frequency. The frequency describes how fast the wave oscillates. The amplitude corresponds to the height of the wave. Finally, the phase indicates the position of the crests of the wave [see Fig.1(a)]. As a result of the wave-particle duality and the superposition principle, sometimes, when an electron is ejected from the atom, it can be in a superposition of two or more waves. If two waves have the same phase, they add up to form a wave with a bigger amplitude as shown in Fig.1(b). This is called constructive interference. However, if the two waves are out of phase, they cancel each other as shown in Fig.1(c), leading to what is called destructive interference. In general, the interference of two or more waves with arbitrary amplitude and phase results in a new wave with a different amplitude and phase [Fig.1(d)]. By modifying the amplitude and phase of the waves, quantum interference affect the electron emission.

With all these concepts, you can understand the title of the thesis. Basically it means that I studied how the fact that the electrons are quantum objects, which can be in a superposition of states and interfere, affects the way they are ejected from the atom. And because photoionization is so fast, I had to investigate these processes with attosecond precision.

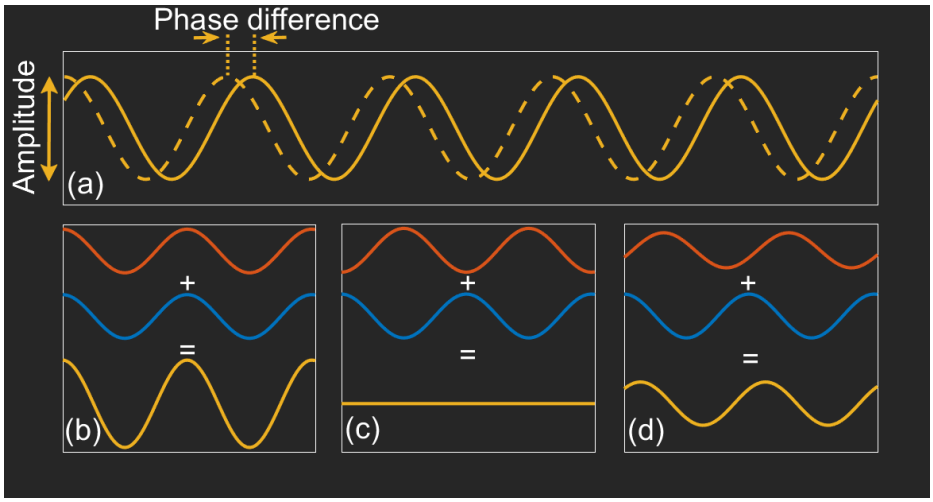

Figure 1: (a) Two waves with the same amplitude and frequency but different phases. (b) Two waves (red and blue) oscillating in phase interfere constructively, resulting in a wave with a larger amplitude and the same phase (yellow). (c) Two waves oscillating out of phase interfere destructively, resulting in a cancellation of the two waves. (d) The interference of two waves with arbitrary amplitude and phase gives rise to a third wave with an amplitude and phase different from the first two.

What is it good for?

All chemical reactions are based on the exchange of electrons between atoms or molecules. In addition, many of the properties of molecules or materials depend on the way electrons move and interact with each other. For example, it is known that, very often, charge migration, meaning electronic motion, plays an important role in radiation damage of biological molecules. Understanding electronic dynamics in matter is hence of great importance for physics, chemistry, material science and biology. However, our understanding of these processes is still very limited such that we must investigate electronic dynamics in simple atomic systems before we can study complex molecules.

A second interesting aspect has to do with the quantum nature of the photoionization process. While we know that the microscopic world is governed by quantum mechanics and that the macroscopic world obeys the laws of classical physics, the frontier between the two is not clear. For example, recently, physicists demonstrated that large molecules such as antibiotics can behave as waves and interfere [1]. The most popular concept used to explain the transition from quantum physics to classical physics is called decoherence. It predicts that the interaction of a quantum system with its environment results in a loss of the "quantum character", leading to a more classical system. The bigger the system is, the more it is likely to be subject to decoherence, which is a big challenge for the development of technology

based on quantum information and nano electronics. In our case, by studying how the interference between electrons evolves on the attosecond time scale, we hope to gain a better understanding on how fast the quantum to classical transition occurs.

Résumé vulgarisé

Effets des interférences quantiques dans la dynamique de photoionisation attoseconde... "Super ! Je comprends même pas le titre." Si c'est ce que vous pensez, cette section est pour vous.

Tirer sur des atomes avec de la lumière

Toute la matière qui nous entoure est faite de la même chose : des atomes. Ces atomes, dont la taille est de l'ordre de 0,1 nanomètres, sont eux-mêmes constitués d'un petit noyau autour duquel orbitent des électrons, un peu comme les planètes gravitent autour du soleil. Si maintenant vous tirez sur un atome avec de la lumière énergétique telle que des rayons ultraviolet extrêmes ou des rayons X, un électron peut absorber la lumière et être éjecté de l'atome. C'est ce qu'on appelle effet photoélectrique ou photoionisation. Cette thèse vise à étudier comment les électrons sont éjectés des atomes suite à l'absorption de lumière. Le problème est que ce processus est extrêmement rapide, des millions de fois plus rapide que l'électronique la plus rapide. L'échelle de temps sur laquelle les électrons bougent est l'échelle attoseconde, où une attoseconde est un milliardième de milliardième de seconde, ou 10^{-18} secondes. De plus, contrairement aux planètes en orbite autour du soleil, les lois qui décrivent le déplacement des électrons ne sont pas les lois de la physique classique auxquelles nous sommes soumis dans notre vie quotidienne. Le microcosme des électrons et des atomes est décrit par la mécanique quantique.

Il y a deux concepts de la mécanique quantique qui sont essentiels à cette thèse. Le premier est le principe de superposition. Ce principe stipule qu'un électron n'est pas forcement ici *ou* là, il peut également être ici *et* là, en même temps. Le deuxième concept est celui de la dualité onde-corpuscule. Cela signifie que les particules telles que les électrons peuvent également se comporter comme des ondes. Les ondes sont caractérisées par trois quantités : amplitude, phase et fréquence. La fréquence décrit la vitesse à laquelle l'onde oscille. L'amplitude correspond à la hauteur de l'onde. Enfin, la phase indique la position des crêtes de l'onde [voir Fig. 2(a)]. En raison de la dualité onde-corpuscule et du principe de superposition, lorsqu'un électron est éjecté de l'atome, il peut se trouver dans une superposition de deux ondes ou plus. Si les deux ondes ont la même phase, elles s'ajoutent pour former une onde avec une plus grande amplitude comme le montre la figure 2(b). C'est ce que l'on appelle des interférences constructives. Cependant, si les deux ondes sont en opposition de phase, elles s'annulent comme indiqué sur la Fig. 2(c), conduisant à ce que l'on appelle des interférences destructives. En général, l'interférence de deux ondes ou plus avec des phases arbitraires donne lieu à une nouvelle onde avec une amplitude et une phase différente [Fig. 2(d)]. En modifiant l'amplitude et la phase des ondes, les interférences quantiques affectent l'émission de l'électron.

Avec tous ces concepts, vous pouvez comprendre le titre de la thèse. En gros, cela veut dire

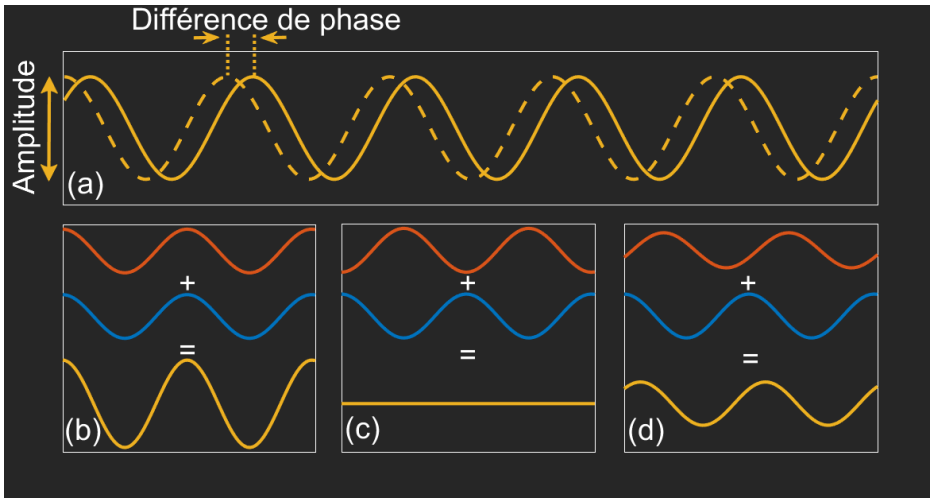

Figure 2: (a) Deux ondes de même amplitude et de même fréquence mais avec différentes phases (b) Deux ondes (rouge et bleue) oscillant en phase interfèrent de manière constructive, ce qui donne une onde de plus grande amplitude et de même phase (jaune). (c) Deux ondes oscillant en opposition de phase interfèrent de manière destructrice, entraînant une annulation des deux ondes. (d) L'interférence de deux ondes d'amplitude et de phase arbitraires donne lieu à une troisième onde dont l'amplitude et la phase sont différentes des deux premières.

que j'ai étudié comment le fait que les électrons sont des objets quantiques, qui peuvent être dans une superposition d'états et interférer, affecte la façon dont ils sont éjectés de l'atome. Et parce que la photoionization est si rapide, j'ai dû étudier ces processus avec une résolution attoseconde.

À quoi ça sert ?

Toutes les réactions chimiques sont basées sur l'échange d'électrons entre atomes ou molécules. De plus, de nombreuses propriétés des molécules ou des matériaux dépendent de la façon dont les électrons se déplacent et interagissent les uns avec les autres. Par exemple, il est connu que, très souvent, la migration de charge, c'est à dire le mouvement des électrons, joue un rôle important dans les dommages causés par les radiations dans les molécules biologiques. La compréhension des dynamiques électroniques dans la matière est donc d'une grande importance pour la physique, la chimie, la science des matériaux et la biologie. Cependant, notre compréhension de ces processus est encore très limitée, de sorte que l'on doit étudier les dynamiques électroniques dans des systèmes atomiques simples avant de pouvoir étudier des molécules complexes.

Un deuxième aspect intéressant concerne la nature quantique du processus de photoionisation. Alors que l'on sait que le monde microscopique est régi par la mécanique quantique et que le monde macroscopique obéit aux lois de la physique classique, la frontière entre ces deux mondes n'est pas claire. Par exemple, récemment, des physiciens ont démontré que de grosses molécules telles que des antibiotiques peuvent se comporter comme des ondes et interférer [1]. Le concept le plus populaire permettant d'expliquer le passage de la physique quantique à la physique classique s'appelle la décohérence. Il prédit que l'interaction d'un système quantique avec son environnement entraîne une perte du "caractère quantique", conduisant à un système plus classique. Plus le système est grand, plus il est susceptible d'être soumis à la décohérence, ce qui constitue un des principaux défis pour le développement de technologies basées sur l'information quantiques et la nanoélectronique. Dans notre cas, en étudiant comment les interférences entre les électrons évoluent à l'échelle attoseconde, on espère mieux comprendre à quelle vitesse se produit la transition quantique-classique.

Resumen divulgativo

Efectos de interferencias cuánticas en la dinámica de fotoionización attosegundo ... " ¡ Genial ! Ni siquiera entiendo el título." Si eso es lo que estás pensando, esta sección es para ti.

Disparar a átomos con luz

Toda la materia que nos rodea está hecha de lo mismo: átomos. Estos átomos, cuyo tamaño es del orden de $0{,}1$ nanómetros están formados por un pequeño núcleo alrededor del cual orbitan electrones, un poco como los planetas orbitan alrededor del sol. Si ahora, disparas a un átomo con luz de alta energia, como rayos ultravioletas extremos o rayos X, un electrón puede absorber la luz y ser expulsado del átomo. Esto es lo que se llama efecto fotoeléctrico o fotoionización. Esta tesis tiene como objetivo estudiar cómo se expulsan los electrones de los átomos tras haber absorbido luz. El problema es que este proceso es extremadamente rápido, millones de veces más rápido que la electrónica más rápida. La escala de tiempo en la que se mueven los electrones es la de attosegundos, donde un attosegundo es una billonésima parte de una billonésima de segundo, o 10^{-18} segundos. Además, al contrario de los planetas que orbitan alrededor del sol, las leyes que describen cómo se mueve el electrón no son las leyes de la física clásica que todos experimentamos en nuestra vida cotidiana. El microcosmos de los electrones y átomos esta descrito por la mecánica cuántica.

Hay dos conceptos de mecánica cuántica que son esenciales para esta tesis. El primero es el principio de superposición. Este principio establece que un electrón no tiene por que estar aquí *o* allí, sino que tambien puede estar aquí *y* allí, al mismo tiempo. El segundo concepto es el de la dualidad onda-partícula. Significa que partículas como los electrones también pueden comportarse como ondas. Las ondas se caracterizan por tres cantidades: amplitud, fase y frecuencia. La frecuencia describe la rapidez con la que oscila la onda. La amplitud corresponde a la altura de la onda. Finalmente, la fase indica la posición de las crestas de la onda [Fig. 3(a)]. Como resultado de la dualidad onda-partícula y del principio de superposición, cuando un electrón es expulsado del átomo, puede estar en una superposición de dos ondas o más. Si dos ondas tienen la misma fase, se suman para formar una onda con una amplitud mayor como se muestra en la figura 3(b). Esto se llama interferencias constructivas. Sin embargo, si dos ondas están en oposición de fase, se cancelarán entre sí como se muestra en la figura 3(c), lo que lleva a interferencias destructivas. En general, la interferencia de dos o más ondas con fases arbitrarias da como resultado una nueva onda con amplitud y fase diferentes. Modificando la amplitud y la fase de las ondas, las interferencias cuánticas afectan la emisión del electron.

Con estos concéptos, podéis entender el título de la tesis. Básicamente, lo que significa es que he estudiado cómo el hecho de que los electrones sean objetos cuánticos, que pueden estar en una superposición de estados e interferir, afecta la forma en que son expulsados del átomo.

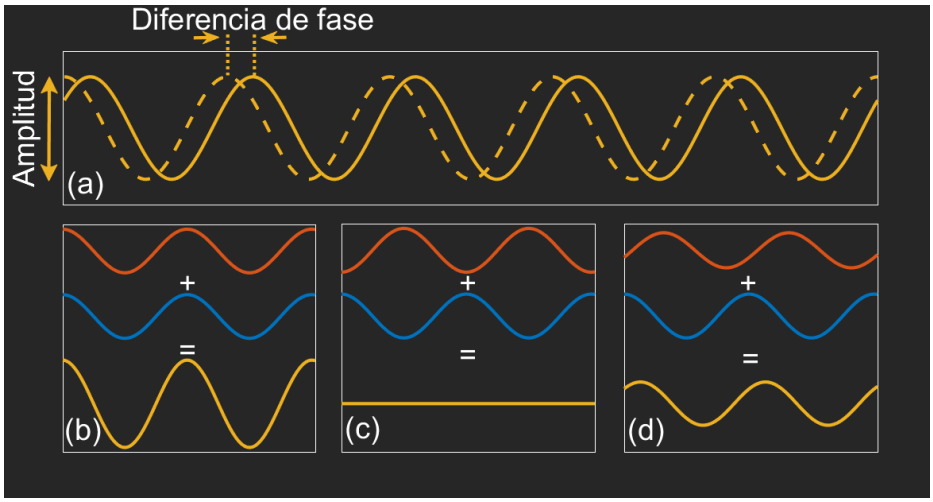

Figura 3: (a) Dos ondas de misma amplitud y frecuencia pero con fases diferentes (b) Dos ondas (roja y azul) que oscilan en fase interfieren de manera constructiva, resultando una onda de mayor amplitud y de misma fase (amarilla). (c) Dos ondas que oscilan en la oposición de fase interfieren de forma destructiva, dando lugar a la cancelación de ambas ondas. (d) La interferencia de dos ondas de amplitud y fase arbitrarias da lugar a una tercera onda de amplitud y fase diferentes de las dos primeras.

Y debido a que la fotoionización es tan rápida, he tenido que investigar estos procesos con resolución attosegundo.

¿Para que sirve ?

Todas las reacciones químicas se basan en el intercambio de electrones entre átomos o moléculas. Además, muchas de las propiedades de las moléculas o de los materiales dependen de la forma en la que los electrones se mueven e interaccionan entre sí. Por ejemplo, se sabe que, muy a menudo, la migración de cargas, es decir el movimiento electrónico, juega un papel importante en el daño por radiación de las moléculas biológicas. Por lo tanto, entender las dinámicas electrónicas en la materia es de gran importancia para la física, la química, la ciencia de los materiales y la biología. Sin embargo, nuestra comprensión de estos procesos todavía es muy limitada, por lo que tenemos que investigar las dinámicas electrónicas en sistemas atómicos simples antes de poder estudiar moléculas complejas.

Un segundo aspecto interesante tiene que ver con la naturaleza cuántica del proceso de fotoionización. Si bien sabemos que el mundo microscópico se rige por la mecánica cuántica y el mundo macroscópico obedece las leyes de la física clásica, la frontera entre los dos mundos no está clara. Por ejemplo, recientemente, unos físicos demostraron que grandes moléculas

como antibióticos pueden comportarse como ondas e interferir [1]. El concepto más popular que explica la transición de la física cuántica a la física clásica se llama decoherencia. Predice que la interacción de un sistema cuántico con su entorno da lugar a una pérdida del çarácter cuántico", lo que conduce a un sistema más clásico. Cuanto más grande sea el sistema, más probable es que esté sujeto a la decoherencia, lo cual es uno de los principales desafíos para el desarrollo de tecnologías basadas en la información cuántica y la nanoelectrónica. En nuestro caso, estudiando cómo evoluciona la interferencia entre electrones en la escala de tiempo del attosegundo, esperamos obtener una mejor comprensión de la rapidez con la un sistema pasa de ser cuántico a ser clásico.

List of publications

This thesis is based on the following publications, referred to by their Roman numerals:

I **Photoionization in the time and frequency domain**

M.Isinger, R. J. Squibb, **D. Busto**, S. Zhong, A. Harth, D Kroon, S. Nandi, C. L. Arnold, M. Miranda, J. M. Dahlström, E. Lindroth, R. Feifel, M. Gisselbrecht, A. L'Huillier
Science, **358**, 893 (2017)

II **Time-frequency representation of autoionization dynamics in helium**

D. Busto, L. Barreau, M. Isinger, M. Turconi, C. Alexandridi, A. Harth, S. Zhong, R. J. Squibb, D. Kroon, S. Plogmacker, M. Miranda, Á Jiménez-Galán, L. Argenti, C. L. Arnold, R. Feifel, F. Martín, M. Gisselbrecht, A. L'Huillier, P. Salières
J. Phys. B: At. Mol. Opt. Phys.,**51**, 044002 (2018)

III **Anisotropic photoemission time delays close to a Fano resonance**

C. Cirelli, C. Marante, S. Heuser, C. L. M. Petersson, Á Jiménez-Galán, L. Argenti, S. Zhong, **D. Busto**, M. Isinger, S. Nandi, S. Maclot, L. Rading, P. Johnsson, M. Gisselbrecht, M. Lucchini, L. Gallmann, J. M. Dahlström, E. Lindroth, A. L'Huillier, F. Martín, U. Keller
Nat. Commun., **9**, 955 (2018)

IV **Accuracy and precision of the RABBIT technique**

M. Isinger, **D. Busto**, S. Mikaelsson, S. Zhong, C. Guo, P. Salières, C. L. Arnold, A. L'Huillier, M. Gisselbrecht
Phil. Trans. R. Soc. A, **377**, 20170474 (2019)

V **Fano's propensity rule in angle-resolved attosecond pump-probe photoionization**

D. Busto, J. Vinbladh, S. Zhong, M. Isinger, S. Nandi, S. Maclot, P. Johnsson, M. Gisselbrecht, A. L'Huillier, E. Lindroth, J. M. Dahlström
Phys. Rev. Lett., **123**, 133201 (2019)

VI **Propensity rules and interference effects in laser-assisted photoionization of helium and neon**

M. Bertolino, **D. Busto**, F. Zapata, J. M Dahlström
accepted in J. Phys. B: At. Mol. Opt. Phys.

VII **Attosecond timing of electron emission from a molecular shape resonance**

S. Nandi, E. Plésiat, S. Zhong, A. Palacios, **D. Busto**, M. Isinger, L. Neoričić, C. L. Arnold, R. J. Squibb, R. Feifel, P. Decleva, A. L'Huillier, F. Martín, M. Gisselbrecht
submitted to Sci. Adv.

VIII **Spin-orbit resolved spectral phase measurements around a Fano resonance**

M. Turconi, L. Barreau, **D. Busto**, M. Isinger, C. Alexandridi, A. Harth, R. J. Squibb, D. Kroon, C. L. Arnold, R. Feifel, M. Gisselbrecht, L. Argenti, F. Martín, A. L'Huillier, P. Salières
submitted to J. Phys. B: At. Mol. Opt. Phys.

IX **Attosecond photoionization dynamics in the vicinity of the Cooper minima in argon**

C. Alexandridi, D. Platzer, L. Barreau, **D. Busto**, S. Zhong, M. Turconi, L. Neoričić, H. Laurell, C. L. Arnold, A. Borot, J.-F. Hergott, O. Tcherbakoff, M. Gisselbrecht, E. Lindroth, A. L'Huillier, J. M. Dahlström, P. Salières
in manuscript

X **Attosecond electron–spin dynamics in Xe 4d photoionization**

S. Zhong, J. Vinbladh, **D. Busto**, R. J. Squibb. M. Isinger, L. Neoričić, H. Laurell, R. Weissenbilder, C. L. Arnold, R. Feifel, J. M. Dahlström, G. Wendin, M. Gisselbrecht, E. Lindroth, A. L'Huillier
submitted to Nat. Phys.

Abbreviations

AOPDF	Acousto-Optical Programmable Dispersive Filter
APT	Attosecond Pulse Train
CC	Continuum-Continuum
CM	Cooper Minimum
EWP	Electron Wavepacket
GDD	Group Delay Dispersion
HHG	High-order Harmonic Generation
IR	Infrared
MBES	Magnetic Bottle Electron Spectrometer
MCP	Microchannel Plate
PAD	Photoelectron Angular Distribution
PES	Photoelectron Spectrum
QST	Quantum State Tomography
RABBIT	Reconstruction of Attosecond Beating By Interference of Two-photon transitions
RRPA	Relativistic Random Phase Approximation
S-O	Spin-Orbit
TOF	Time Of Flight
VMIS	Velocity Map Imaging Spectrometer
XUV	Extreme Ultraviolet

Contents

Chapter 1

Introduction

1 Introduction to attosecond science

The observation of the photoelectric effect by Hertz [2] and its explanation by Einstein [3] paved the way to the development of quantum mechanics. When high frequency light is absorbed by an atom, a molecule or a solid, one or several electrons can be emitted in a process known as photoionization or photoelectric effect. The frequency of the light, ν, must be high enough for the photon energy $h\nu$ to be larger than the electron binding energy I_p. Studying the kinetic energy of the emitted electron, $E_k = h\nu - I_p$, provides detailed information on the internal structure of matter. This is known as photoelectron spectroscopy and was developed by Kai Siegbahn, for which he was awarded the Nobel Prize.

The development of femtosecond laser technology (1 fs = 10^{-15} s) in the 80's led to a revolution in time-resolved spectroscopy, providing a way to study nuclear dynamics in molecules on their natural time scale. Ahmed Zewail, the founding father of this new field of research called femtochemistry, was awarded the Nobel prize in 1999. While it was then possible to probe the motion of the nuclei in a molecule, electronic dynamics, which govern nuclear dynamics, were still out of reach since they occur on the attosecond time scale (1 as = 10^{-18} s).

The discovery of high-order harmonic generation (HHG) at the end of the 80's [4, 5] and the demonstration in 2001 and that the extreme ultraviolet (XUV) radiation emitted by this process corresponds to a train of attsoecond pulses [6] revolutionized the study of electron dynamics in matter. This field of research, called attosecond science, has quickly developped in the last two decades and has led to numerous studies regarding electron dynamics in matter (see Refs. [7, 8] for a review of the field). A large number of attosecond measurement techniques have been developped over the years, most of them using an XUV attosecond

pulse or pulse train to trigger the dynamics and an infrared (IR) pulse acting as a probe. In this thesis, we use the interferometric technique called reconstruction of attosecond beating by interference of two-photon transitions (RABBIT)[1] which uses the combination of XUV attosecond pulse trains with femtosecond IR pulses [6]. This technique takes advantage of the wave-particle duality of electrons. When an electron is emitted after absorption of an XUV photon, it can be seen as a wave, or wavepacket, characterized by a spectral amplitude and a spectral phase. The IR pulse is used to make the electron waves interfere in order to measure their phase. In analogy with optical pulse characterization techniques, using the measurements of the electron amplitude and phase in the spectral domain, we can access information on the temporal dynamics of photoionization. The RABBIT technique, initally used to characterized the attosecond pulse trains, has since then been applied to investigate photoionization dynamics in atoms [9–14] molecules [15–19] and solids [20, 21].

2 Scope of this work

In 2010 Schultze *et al.* showed that photoionization from the $2p$ shell in neon is delayed compared to photoionization from the $2s$ shell [22]. This measurement was shortly followed by the measurement of a relative delay between electrons photoemitted from the $3s$ and $3p$ shells in argon [9]. These two results triggered a lot of interest from both experimentalists and theorists as it was the first time that it was possible to access information on photoionization dynamics on the time scale of a few tens of attoseconds.

When an electron is promoted to the continuum, the electron wavepacket (EWP) propagates on an attractive ionic potential. As a result, the EWP is delayed compared to the same EWP propagating in free space. The measurement of photoionization time delays is particularly interesting because it is very sensitive to the interaction of the escaping electron with the remaining ion. As such, these measurements constitute important benchmarks for theoretical calculations since electron correlations must be taken into account very accurately in order to reproduce the experimental observations.

At the beginning of this thesis, most of the work done on attosecond photoionization dynamics had consisted in *demonstrating* the capability of the two major techniques, RABBIT and attosecond streaking [23], to measure photoionization time delays. Here, this thesis focuses on *applying* the RABBIT technique to investigate the role of quantum interference in photoionzation dynamics. We investigate photoionization dynamics in a variety of systems (He, Ne, Ar, Xe, N_2), where the presence of several ionization channels results in the emission of EWPs which are in a superposition of states. An important part of this thesis aims at

[1] Despite this technique being close to 20 years old, there is no concensus on how it should be abreviated. We follow the tradition of the ultrafast optics community of naming ultrashort pulse characterization techniques after animal names. The spellings RABBITT and RABITT can also be found in the literature.

studying experimentally and theoretically the effect of the interplay of the different ionization channels on the ionization dynamics, with the aim of fully characterizing the quantum state of the emitted EWPs.

3 Papers and outline

This thesis is based on 10 papers. In paper IV, we present an in-depth study of the RABBIT technique. The other papers focus on the study of photoionization dynamics in different systems.

In papers I and IX, we study angle-integrated non-resonant photoionization. In paper I, we investigate photoionization time delays between $2s$ and $2p$ electrons in Ne, solving a 7-year old puzzle raised by the first measurements of photoionization time delays [22] and demonstrating the accuracy of the RABBIT technique. In paper IX we measure time delays between electrons emitted from the $3s$ and $3p$ shells of Ar in the challenging energy region of the $3s$ and $3p$ Cooper minima. In both papers we identify the presence of competing ionization mechanisms (shake-up processes) which must be taken into account to obtain good agreement with theory.

In papers II and VIII, we use the RABBIT technique to investigate angle-integrated photoionization via Fano resonances, where the interference of direction ionization and autoionization results in a modification of the ionization dynamics. In paper II, we measure the amplitude and phase of the EWPs emitted via the $sp2^+$ and $sp3^+$ autoionizing resonances in He and characterize them in the time-frequency domain. This allows us to disentangle the ionization dynamics associated to the direct and autoionizing channels and to follow in time the formation of the quantum interference between the two ionization paths. In paper VIII, we study the EWPs emitted via the $3s^{-1}4p$ Fano resonance in Ar. In this case, the spin-orbit splitting of the ion results in an incoherent superposition of EWPs which makes the analysis more difficult. We present a method that allows the characterization of the individual spin-orbit components.

In papers VII and X, we apply the RABBIT technique to study angle-integrated photoionization in the vicinity of shape resonances. In paper VII, we probe vibrationally resolved photoionization time delays in N_2 in the vicinity of the $3\sigma_g^{-1}$ resonance. These measurements show that the transient trapping of the photoelectron by the shape resonance allows the molecule to vibrate during photoionization, indicating a break-down of the Franck-Condon approximation. In paper X, we investigate the photoionization from the $4d$ shell in Xe, in the low energy part of the giant dipole resonance, close to the $4d$ threshold. We measure a large time delay difference close to threshold between electrons associated to the two spin-orbit split states of Xe^+. We attribute this observation to the interference of the giant dipole

resonance with narrow resonances at threshold due to spin-orbit interaction.

Finally, in papers III, V and VI, we extend our photoionization studies to investigate how the ionization dynamics depend on the emission angle of the photoelectron. In paper III, we use the angle-resolved RABBIT technique to investigate the photoionization via the $3s^{-1}4p$ resonance in Ar. We show that the presence of two resonant channels with different angular momenta leads to a complex energy and angle dependence of the photoionization time delays. In addition, we observe that even in non-resonant conditions, the photoionization time delays are strongly angle-dependent and the photoelectron angular distribution are delay-dependent. In papers V and VI, we investigate non-resonant angle-resolved photoionization. In paper V, we study the strength of the different angular channels and we show that Fano's propensity rule can be extended to laser-assisted photoionization. Applying it to the RABBIT scheme, we demonstrate that it provides a fundamental explanation to both the angle-dependence of the photoionization time delays and the delay-dependence of the photoelectron angular distributions reported in paper III. In paper VI, we investigate angle-resolved laser assisted photoionization and discuss the cases where both one and two IR photons interact with the EWP.

The outline of the thesis is the following. In chapter 2, we discuss the generation of the attosecond pulse trains and their spectral and temporal properties. In chapter 3, we introduce laser-assisted photoionization and discuss the propensity rules in channel-resolved photoionization. We then present in detail the RABBIT technique, its advantages and limitations. In chapter 4, we introduce the concept of photoionization time delays and present our results on non-resonant photoionization in neon and argon (papers I and IX). In chapter 5 we first introduce Fano's theory of autoionization resonances and present the results on the characterization of EWPs emitted via resonances in He (paper II) and Ar (paper VIII). We also discuss new results obtained in helium with high spectral resolution, which have not yet been published. Finally, we discuss photoionization via shape resonances in both N_2 and Xe. In chapter 6, we introduce the angle-resolved RABBIT technique and present the results obtained on angle-resolved photoionization time delays in the vicinity of an autoionizing resonance in Ar (paper III). We then discuss the theory of angle-resolved RABBIT measurements and explain how Fano's propensity rule explains the results reported in paper III regarding non-resonant photoionization. Finally chapter 7 gives a summary and an outlook.

Chapter 2

Generation of attosecond pulse trains

The photoionization dynamics studied in this thesis are triggered by the absorption of attosecond pulse trains. These pulse trains are generated via the extremely non-linear interaction of intense femtosecond laser pulses with noble gas atoms. The aim of this chapter is to explain how these extremely short light pulses are generated and controlled. We first introduce the basic concepts behind the generation of intense femtosecond pulses before describing the interaction of these pulses with an atomic gas and discussing in detail the spectral and temporal properties of the emitted radiation, the attosecond pulse trains.

1 Introduction to ultrafast optics

1.1 Generation of femtosecond pulses

Light is an electromagnetic wave characterized by the frequency, ν, at which the electric and magnetic fields oscillate. If light is monochromatic, it is made of a single infinitely long wave oscillating at a specific frequency. In order to produce short light bursts, it is necessary to have multiple frequencies interfering with each other as shown in Fig 2.1(a). The duration of these light bursts, $\Delta\tau$, is inversely proportional to the number of different frequencies in the light, i.e. its spectral width $\Delta\nu$, as stipulated by the the time-bandwidth product,

$$\Delta\tau\Delta\nu \geq \gamma, \tag{2.1}$$

where $\gamma = 0.44$ for Gaussian pulses. In order to produce ultra-short pulses, it is hence important to find a process that can produce light with a broad bandwidth. In addition, all

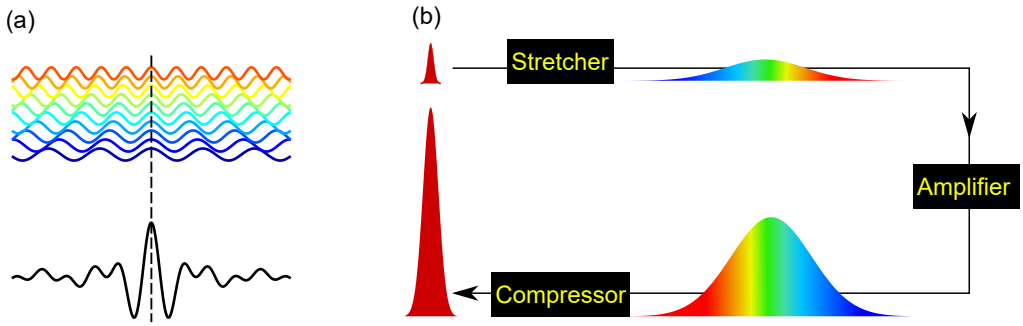

Figure 2.1: Working principle of intense femtosecond lasers. (a) The sum of multiple phase-locked waves with different frequencies results in a short light pulse (black curve). (b) Schematic representation of chirped pulse amplification.

the waves with different frequencies must be emitted synchronously, meaning that all the waves should have the same phase, as illustrated by the dashed line in Fig. 2.1(a). These two principles are at the basis of ultrafast laser technology. The first requirement, regarding the spectral width of the light, sets the type of crystals used as lasing medium. Titanium doped sapphire (Ti:Sapphire) crystals are, so far, the most widespread type of crystal used in femtosecond lasers. The second requirement, regarding the synchronous emission of the different frequencies, is more complicated to achieve. Since spontaneous emission, which is the starting point of the lasing process, is intrinsically stochastic, different frequencies are in general not synchronized. In order to generate short pulses, it is necessary to force the oscillator to only amplify pulses for which all frequencies are synchronized. This can be achieve using various modelocking techniques [24]. The duration of the laser pulses going out of the cavity can be below 10 fs, however, the energy per pulse is extremely low, of the order of nJ/pulse. Many applications require much higher pulse energies and hence it is necessary to further amplify the laser pulses.

1.2 Chirped pulse amplification

Laser pulses can be amplified by sending them into multi-pass or regenerative amplifiers. However, if no precaution is taken, due to their short duration, the laser pulses quickly reach a critical intensity beyond which amplification crystals can be damaged. If one needs to amplify further the laser pulses, a "trick" must be used. This "trick" is chirped pulse amplification (CPA) which was pioneered by Donna Strickland and Gérard Mourou [25], an achievement for which they were awarded the 2018 physics Nobel prize. The key idea consists in stretching temporally the pulses using, for example, a pair of gratings, thereby reducing the peak power while maintaining the pulse energy. For technical reasons, it is preferable to stretch the pulses by delaying higher frequencies with respect to lower ones, which requires additional

imaging optics [26]. After stretching the pulse, the different frequencies are not synchronized any more as shown in Fig. 2.1(b) and the pulses are said to be chirped. The pulses can then be amplified in several stages before being compressed temporally using a pair of gratings spaced by a distance such that all the frequencies are synchronized again. This technique hence allows generating short intense pulses without damaging the amplification medium. The principle of this amplification technique is schematically presented in Fig. 2.1(b).

2 High-order harmonic generation and attosecond pulse trains

As described above, the shortest duration to which a light pulse can be compressed is inversely proportional to its spectral bandwidth. Therefore, the pulse duration is limited by the bandwidth that the amplifying crystals can support. While the spectral bandwidth can be additionally broadened via self-phase modulation in gas-filled hollow-core fibres, it is, in any case, impossible to reach pulse durations below the single cycle limit which is ≈ 2.67 fs at 800 nm. To reach the attosecond timescale, the central wavelength has to be shifted to the extreme ultraviolet (XUV). This is impossible with traditional laser systems. However, it was discovered in the late 80's that by focusing an intense laser pulse in a gas, very high odd-order harmonics of the fundamental laser frequency are generated [4, 5]. After a quick decrease of intensity as a function of harmonic order, a plateau appears, followed by another sharp decrease of intensity. The generation of such high order harmonics and the presence of a plateau in the harmonic spectrum is impossible to explain within the work frame of perturbative non-linear optics according to which the intensity of the different harmonics should decrease exponentially with increasing harmonic order. In this case, the electric field is so strong that it can significantly distort the atomic potential. Therefore, a non-perturbative treatment of the light-matter interaction is necessary.

2.1 The 3-step model

The first model to explain HHG was developped by Kulander and coworkers [27] and Corkum [28] using a semi-classical approach. This model can be decomposed in three steps presented in Fig. 2.2. A more advanced, fully quantum mechanical, model was developed a year later [29]. Here we only discuss the semi-classical approach which can explain most of the spectral and temporal features of HHG. In the first step, the laser electric field is strong enough to bend the Coulomb potential of the atom, creating a potential barrier through which a valence electron can tunnel out. In the second step, the electron is accelerated away from the ion by the laser field. When the electric field changes sign, the electron is driven back to the parent ion. Finally, in the last step, the electron can recombine with the ion, leading to the emission of an XUV photon whose energy is given by $\hbar\Omega = I_p + E_k$, where I_p is the ionization potential of the neutral atom, E_k is the kinetic energy accumulated by the

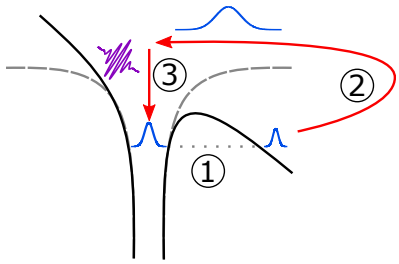

Figure 2.2: Schematic representation of the 3-step model. 1) The atomic potential (dashed gray curve) is distorted by the laser field, giving rise to a potential barrier (black curve) through which the electron can tunnel. 2) The electron is accelerated away and then driven back to the ion. 3) The electron recombines with the ion and emits an attosecond XUV pulse.

electron during its trajectory in the continuum and Ω is the angular frequency of the XUV light.

When the electron tunnels through the barrier, it appears in the continuum at time t_i and position $x(t_i) = 0$ with no kinetic energy. Neglecting the influence of the ionic potential, the electron's trajectory in a linearly polarized laser field, $E(t) = E_0 \sin(\omega t)$, calculated classically using Newton's equation of motion, is given by

$$x(t_i, t) = \frac{eE_0}{m_e\omega^2}\left[\sin(\omega t) - \sin(\omega t_i) - \omega(t - t_i)\cos(\omega t_i)\right], t \leq t_i \tag{2.2}$$

with ω the angular frequency of the IR field, e the electron charge and m_e its mass. Fig. 2.3(a) shows the trajectories followed by the electron for different ionization times. Depending on the ionization time, some trajectories return to the parent ion (coloured trajectories) while others do not (dashed grey trajectories), leading to the ionization of the atom. The kinetic energy of the returning electron as a function of the recombination time is shown in Fig. 2.3(b). The maximal kinetic energy that can be achieved is given by $E_{\text{cutoff}} \approx 3.17U_p$, U_p being the ponderomotive energy defined as:

$$U_p = \frac{E_0^2 e^2}{4m_e\omega^2} \propto \lambda^2 I, \tag{2.3}$$

with I the laser intensity and λ the central wavelength. Since the maximal kinetic energy is limited to $3.17U_p$, this explains the origin of the cutoff frequency observed in HHG at $I_p + 3.17U_p$. As a result, the generation of high energy photons requires high intensities and long wavelengths. Photon energies in the keV range have been demonstrated using mid-IR lasers [30, 31]. Figure 2.3(b) also shows that there are two sets of the trajectories leading to the same return kinetic energy. There are long trajectories that tunnel at an early time and spend a long time in the continuum and short trajectories, which tunnel at a later time and

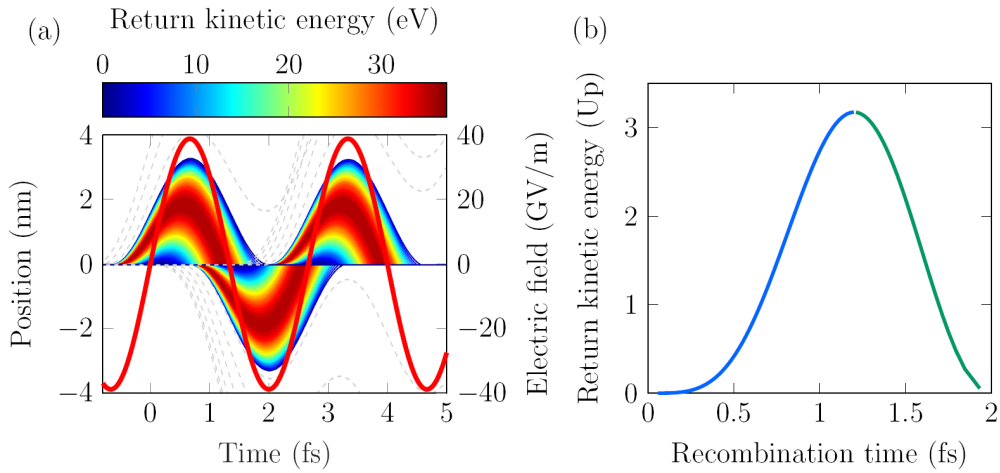

Figure 2.3: (a) Classical electron trajectories in a laser field. The color of the curves indicates the kinetic energy of the electron when it recombines with the ion. A few trajectories for which the electron cannot recombine with the ion are plotted in dashed grey. (b) Return kinetic energy of the electron as a function of the recombination time for long (green) and short (blue) trajectories.

spend a shorter time in the continuum. While both trajectories lead to the same range of kinetic energies, the properties of the light emitted by these two trajectories is different and is discussed in section 2.2.

Finally, as shown in Fig 2.3(a), the 3-step process occurs twice per cycle. As a result, the XUV spectrum corresponds to a comb of odd harmonics[1]. The spectral and temporal properties of the generated XUV field are discussed in sections 2.3 and 2.4

2.2 Phase matching

The model presented so far describes only the response of a single atom to the laser field. However, in practice, the laser is focused in a gas and multiple atoms emit XUV radiation. If the phase of the XUV emitted from different atoms is random, the macroscopic XUV flux will be close to zero due to destructive interference. In order to improve the XUV flux, it is necessary to phase match the radiation from all the atoms as shown in Fig. 2.4. The total wavevector mismatch, $\Delta k = qk - k_q$, has four contributions:

$$\Delta k = \Delta k_e + \Delta k_n + \Delta k_g + \Delta k_d, \tag{2.4}$$

[1]It is possible to generate both even and odd harmonics by breaking the symmetry between two consecutive sub-cycles using two-color fields or asymmetric molecules.

Figure 2.4: Illustration of phase matching. On the left, the radiation emitted from the different atoms is not phase matched, yielding a low XUV intensity. On the right, all the waves are in phase and interfere constructively.

where Δk_e and Δk_n account respectively for the plasma and neutral gas dispersion, Δk_g originates from the geometrical phase, called Gouy phase, due to the focusing of the laser and Δk_d is the dipole phase acquired by the electron during its propagation in the continuum in the 3-step model. As a result, the dipole phase is different for long and short trajectories. Experimentally, the main parameters that we can tune are the laser intensity, the gas pressure and the focus position. In the following, we review from an experimental perspective the main effects of these parameters on phase matching. A formal discussion of phase matching can be found in Ref. [32].

The intensity is probably the most complicated parameter to tune. It affects mostly Δk_e, Δk_n and Δk_d. The higher the intensity, the more free electrons are created and the less neutral atoms are available. It is necessary to have a small amount of free electrons in the medium, however a too high intensity can destroy the phase matching due to a too high plasma dispersion. While high intensities are needed to reach high XUV photon energies, plasma dispersion puts a limit on the intensity that can be used. In addition, the optimal intensity depends on the gas used for generation. Low atomic number noble gases such as helium and neon have a relatively low polarizability which allows us to use higher intensities and hence reach higher photon energies. Nonetheless, this comes at the price of the conversion efficiency which is significantly lower in these gases compared to heavier noble gases such as argon or xenon. It is also worth mentioning that the generation of free electrons results in a blue-shift of the fundamental frequency [33]. This effect can lead to a significant energy shift of the highest harmonic orders. For example a blue-shift of 0.05 eV of the IR central frequency results in a shift of 2.55 eV of harmonic 51.

The intensity also affects the dipole phase [34–38]. Importantly, because the long trajectories spend more time in the continuum than the short ones, their dipole phase varies faster as a function of intensity. As a consequence, for a given intensity, the phase mismatch Δk_d, is different for long and short trajectories. This means that it is possible to optimize the generation

conditions to preferentially phase match one class of trajectories or the other. In addition, the strong intensity dependence of the long trajectories results in a larger divergence compared to short trajectories. In practice, we always try to phase match the short trajectories.

The gas pressure affects the plasma and neutral dispersion linearly so that a small modifications of the pressure affects them similarly. Since the plasma and neutral contributions, Δk_e and Δk_n have opposite signs, this small change of pressure does not have a significant impact on the phase matching conditions. However, it can lead to a modifications of the spectral envelope of the harmonics and a temporal walk-off [39]. In addition, increasing the pressure can increase the XUV flux due to the larger number of emitters. However, a too high pressure can lead to re-absorption of the generated XUV in the gas, decreasing the XUV generation efficiency [40].

Finally, the focus position mostly affects the Gouy phase and the dipole phase. By adjusting the focus position it is possible to phase match either the long or short trajectories. Harmonic generation from the short trajectories is usually optimized by focusing the laser slightly after the gas cell. It has also been shown that the position of the focus has a significant impact on the divergence and temporal properties of the harmonics as a result of strong spatio-temporal couplings [36, 38]. Focusing close to the gas cell helps minimizing these effects [38].

At this point, it is important to emphasize that these few paragraphs are more of a beginners guide to generate reasonably good harmonics rather than a secret recipe for perfect harmonics. In practice, generating harmonics is an iterative process where one changes one parameter at the time and looks at the effect on the yield and shape of harmonics, trying to optimize the harmonic spectrum in the region of interest. Indeed, because phase matching depends on the harmonic order, it is often impossible to simultaneously optimize all the harmonic orders, especially when generating in neon, where the HHG spectrum spans more than 100 eV.

2.3 Attosecond pulse trains

Very little time after the discovery of HHG, it was suggested that the broad bandwidth of the harmonic comb could support pulses of attosecond duration [41, 42]. However, as is also the case for the generation of femtosecond IR pulses, it is necessary that all the harmonics are synchronized. Here we discuss in more detail the spectral and temporal properties of attosecond pulse trains. This discussion is restricted to the short trajectories.

As can be seen in Fig. 2.3, within one half cycle, the different photon energies are emitted at different times, resulting in the emission of a chirped pulse. The phase of the XUV pulse is given by the dipole phase. Based on the semi-classical 3-step model, an expression of the dipole phase can be calculated by approximating the return kinetic energy of the electron to

a linear function of the recombination time [37]

$$\Phi(\Omega) = \frac{\gamma}{I}(\Omega - \Omega_p)^2, \tag{2.5}$$

where $\Omega_p = I_p/\hbar$ and $\gamma = 1.03 \times 10^{-18}\text{s}^2\text{Wcm}^{-2}$ at 800 nm. The resulting group delay, τ_{XUV}, is then simply given by the frequency derivative of the spectral phase:

$$\tau_{XUV} = \frac{\partial\Phi}{\partial\Omega} = \frac{2\gamma}{I}(\Omega - \Omega_p). \tag{2.6}$$

This chirp, called attochirp, is typically of the order of 10^{-2} fs^2 so that, while the XUV pulses are not Fourier limited, their duration still lies in the attosecond range.

In addition to the attochirp, since the intensity of the IR field is time-dependent, the dipole phase also depends on time. For long enough driving pulses, the variation of the temporal envelope of the laser field during a half-cycle is negligible such that this effect does not affect the phase of individual attosecond pulses in the train. However, the variation of the dipole phase from one attosecond pulse to the other, often cannot be neglected. As a result, the individual harmonics, which result from the interference of all the attosecond pulses in the train, experiences a chirp called femtochirp. Assuming a Gaussian envelope of the generating IR field $I(t) = I_0 \exp(-at^2/\tau^2)$, with $a = 4\ln(2)$ and τ the pulse duration (full width at half maximum), we show in paper IV that the time dependence of the dipole phase in Eq. 2.5 can be approximated by

$$\Phi(\Omega, t) \approx \frac{\gamma(\Omega - \Omega_p)^2}{I_0}\left(1 + \frac{at^2}{\tau^2}\right). \tag{2.7}$$

The chirp rate of the q^{th} harmonic, b_q, is given by the second time derivative of the dipole phase:

$$b_q = -\frac{\partial^2\Phi}{\partial t^2} \approx -\frac{2a\gamma(q\omega - \Omega_p)^2}{\tau^2 I_0}. \tag{2.8}$$

The absolute value of the chirp rate increases as the pulse duration of the IR decreases because the intensity varies faster for short pulses. In addition, as can be seen from Eq. 2.8, the chirp rate always increases with harmonic order [see Fig 2.5(a)]. However, as will be discussed in chapter 3, the RABBIT technique gives access to the spectral phase of the high-order harmonic spectrum, not the temporal one. It is hence interesting to link the chirp rate to the group delay dispersion (GDD), ϕ_q'', defined as the second derivative of the spectral phase with respect to the frequency. The GDD is linked in a non trivial way to the chirp rate via [35]

$$\phi_q'' = -\frac{b_q\tau_q^4/2}{a^2 + b_q^2\tau_q^4}. \tag{2.9}$$

Assuming that all the harmonics have the same duration $\tau_q \approx \tau/2$ we show in Fig. 2.5(b) the variation of the GDD with harmonic order. Unintuitively, the GDD has an opposite

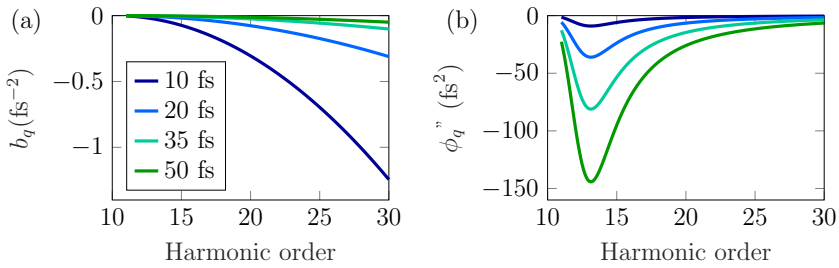

Figure 2.5: Harmonic chirp in the spectral and temporal domains. (a) Chirp rate and (b) GDD as a function of harmonic order. Figure adapted from paper IV.

pulse duration dependence compared to the chirp rate. Figure 2.5(b) shows that high-order harmonics have a small GDD and a rather small pulse duration dependence compared to low-order harmonics. While both the chirp rate and the GDD can be used to characterize the femtochirp, they do not measure the same thing. The chirp rate measures how the instantaneous frequency varies as a function of time while the GDD measures how the group delay varies across the spectrum.

These results can be physically understood as follows. Low-order harmonics are generated during most of the IR pulse duration and are spectrally narrow. As a consequence, the chirp rate of these harmonics is small, since the variation of the instantaneous frequency is stretched over a long time, while their GDD is large due to the large variation of the group delay over a narrow spectrum. On the contrary, the generation of the highest-order harmonics is confined to the maximum of the generating IR pulse. These harmonics are temporally short and spectrally broad, which means that, compared to low-order harmonics, the chirp rate of these harmonics will be bigger and the GDD will be smaller.

2.4 Time-frequency representation of attosecond pulse trains

As is clear from the previous discussion, one of the characteristics of HHG and attosecond pulse trains is that there are two time and energy scales at play (eV↔as ; meV↔fs), which are easy to confuse. Rather than switching from one domain to the other, it can be interesting to find a unique representation in the time-frequency domain.

One of the most famous time-frequency representation is the Wigner distribution[2] [43–45],

[2] It is sometimes also referred to as Wigner-Ville distribution in reference of the french physicist Jean Ville.

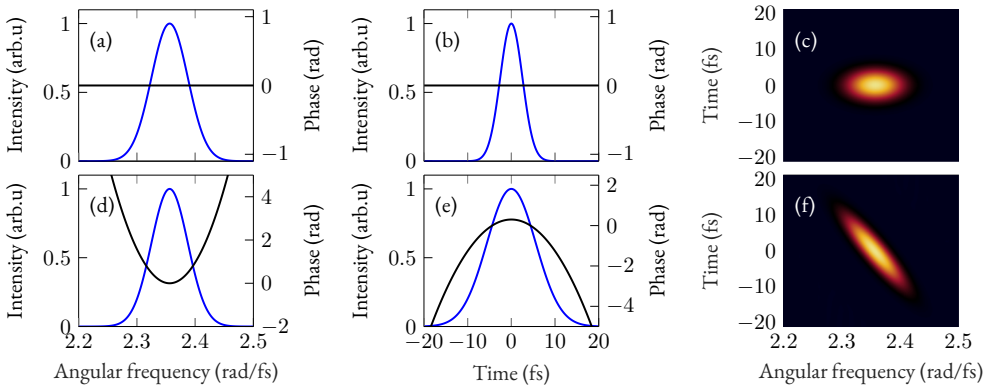

Figure 2.6: Femtosecond pulses in the time and frequency domains. The top row (a,b,c) corresponds to a Fourier limited pulse. The bottom row (d,e,f) corresponds to a chirped pulse. (a,d) Spectral amplitude and phase. (b,e) Temporal amplitude and phase. (c,f) Time-frequency representation of the pulses using the Wigner distribution.

which is defined as:

$$\begin{aligned} W(\Omega, t) &= \int_{-\infty}^{+\infty} E(\Omega - \frac{\omega}{2}) E^*(\Omega + \frac{\omega}{2}) e^{i\omega t} \mathrm{d}\omega \\ &= \int_{-\infty}^{+\infty} \tilde{E}(t - \frac{\tau}{2}) \tilde{E}^*(t + \frac{\tau}{2}) e^{-i\Omega\tau} \mathrm{d}\tau \end{aligned} \tag{2.10}$$

where $E(\Omega)$ and $\tilde{E}(t)$ are the complex amplitude of the light field in the spectral and temporal domains respectively. The particularity of this distribution is that its projections (also called marginals) on the time or frequency axes yield respectively the temporal or spectral intensity.

Before discussing the time-frequency representation of attosecond pulses, let us discuss that of isolated femtosecond pulses. First, we consider a Fourier limited Gaussian pulse whose spectral amplitude and phase is given in Fig. 2.6(a). Taking its Fourier transform yields its temporal amplitude and phase as shown in Fig. 2.6(b). Since the pulse is Fourier limited, both spectral and temporal phases are flat[3] and the pulse duration corresponds to that defined by the time-bandwidth limit. Figure 2.6(c) shows the Wigner distribution of the femtosecond pulse. It shows that all frequencies come at the same time, resulting in the shortest pulse possible. We now investigate the case of a chirped pulse. We consider a pulse with the same spectrum as in the first case but with a quadratic phase variation [see Fig. 2.6(d)]. Its Fourier transform yields a longer pulse than in the first case as can be seen in Fig. 2.6(e). The Wigner distribution of this pulse, displayed in Fig. 2.6(f), shows that, due to the quadratic spectral

[3]In principle, because the spectrum is not centered around 0, the temporal phase increases linearly with time with a slope equal to the central frequency of the pulse. Here this linear phase has been subtracted.

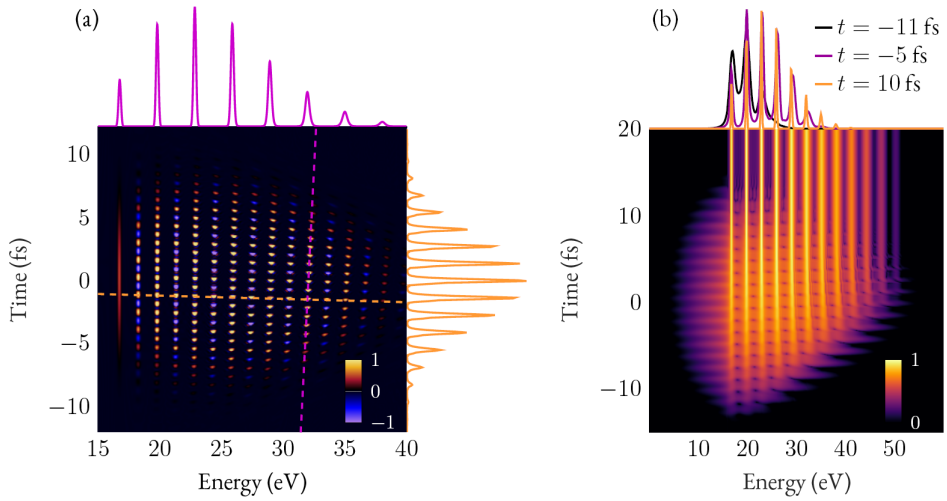

Figure 2.7: Time-frequency analysis of an attosecond pulse train. (a) Wigner distribution of an APT generated by a 20 fs IR pulse and its marginals. The orange dashed line shows the attochirp across a single attosecond pulse in the train. The magenta dashed line shows the femtochirp across one of the harmonics. (b) Build-up of the XUV spectrum in a logarithmic scale together with lineouts of the transient XUV spectrum for different delays in a linear scale. Both the Wigner distribution and the transient XUV spectrum are given in arbitrary units.

phase, high frequencies arrive before low frequencies, resulting a tilted Wigner distribution. This tilt in the time-frequency domain is characteristic of a chirp.

Let us now discuss the Wigner distribution of attosecond pulses. Figure 2.7(a) shows the Wigner distribution of a simulated attosecond pulse train, generated by a 20 fs laser pulse, and its projections in the time (orange) and frequency (magenta) domains. Compared to the isolated femtosecond pulse, here the Wigner distribution is more complex. If we look at a given harmonic on the projection, we can see that it corresponds to a long structure in time. If instead we look at an individual attosecond pulse, we see that it corresponds to a broad structure in frequency. However, in both cases these signals are modulated as a result of interference characteristic of the Wigner distribution. This effect is, for example, at the origin of the structure observed at the position of even harmonics. These interference terms can take negative values such that, once integrated over time, the oscillations observed at the position of the even harmonics disappear. One of the advantages of this representation is that the two time and energy scales discussed previously are visible in a single representation. In particular both atto- and femtochirps are visible as a slight tilt of the structures discussed above. The attochirp, in dashed orange, spans the entire HHG spectrum but varies only very slightly from one attosecond pulse to the other. The femtochirp, in dashed magenta, spans the whole pulse train duration and is different from one harmonic to the other. In particular, Fig. 2.7(a)

shows that the femtochirp rate increases with harmonic order as discussed in section 2.3.

The Wigner distribution provides a representation of the "final" attosecond pulse train in the time-frequency domain and reveals the different time and energy scales at play. However, it does not provide information on the build up of the spectrum during HHG. Information on how the harmonic spectrum dynamically builds-up as a function of time can be obtained using the cumulative Fourier transform defined as [13, 46]:

$$S(\Omega, t) = \int_{-\infty}^{\infty} \tilde{E}(\tau)\Theta(\tau - t)e^{-i\Omega\tau}\mathrm{d}\tau, \tag{2.11}$$

where $\Theta(\tau - t)$ is the Heaviside function. Figure 2.7(b) shows the build-up of the XUV spectrum on a logarithmic scale as a function of time. The time zero corresponds to the maximum of the generating IR pulse. This figure shows that, every half cycle, an attosecond pulse with a continuous broad spectrum is emitted. As time progresses, constructive interference at odd harmonic orders lead to a build-up of the XUV intensity while at even orders, destructive interference from pulse to pulse result in an absence of build-up. We can also see that, on the rising slope of the IR pulse ($t < 0$), the spectral bandwidth of the individual attosecond pulses increases with time due to the increase of U_p as a function of time. After the maximum of the IR field passes, U_p decreases and so does the bandwidth of the individual pulses. This also shows that the highest harmonics are emitted later and for a shorter time than the lower harmonics. The line-outs on top of Fig.2.7(b) show that the spectral width of the individual harmonics decreases as a function of time. The more attosecond pulses are emitted and interfere, the sharper the harmonics get.

3 The attosecond light source

The attosecond light source used during this thesis is driven with a femtosecond Ti:Sapphire CPA laser system. We start with a *Rainbow* oscillator from *Femtolasers*, which delivers 7 fs pulses with an energy of 2.5 nJ at a repetition rate of 76 MHz. The pulses are stretched using a single grating as in [47] and sent through an acousto-optical programmable dipersive filter (AOPDF) [48], *Dazzler* from *Fastlite*, which is used to compensate for phase distortions during the subsequent amplification process, in order to obtain a Fourier limited pulse at the end of the laser chain. In addition, it allows shaping the spectrum of the laser pusles. By reducing the bandwidth of the stretched pulse sent in the following amplification stages, the *Dazzler* can be used to tune the central wavelength of output pulse between approximately 780 nm to 820 nm. After this shaping step, the pulses are sent to four amplification stages: a multi-pass amplifier, a regenerative amplifier, a 3-pass amplifier and a final 3-pass amplifier cryogenically cooled with liquid helium. The Ti:Sapphire crystals in the amplification stages are pumped by frequency doubled Nd:YLF (Neodymium-doped yttrium lithium fluoride) lasers, a *Photonics DM30-527* for the first three stages and a *Continuum Terra laser* for the

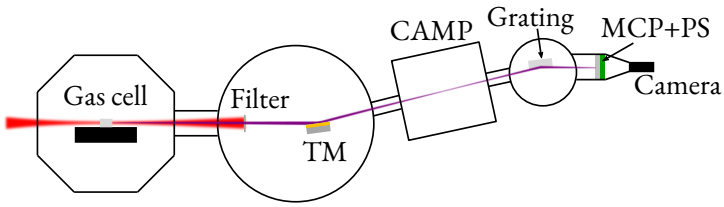

Figure 2.8: Schematic representation of the HHG setup. High-order harmonics are generated in a gas cell, after which the IR is filtered out with a metallic filter. The XUV radiation is focused in the multi-purpose chamber for atomic and molecular physics (CAMP) with a toroidal mirror (TM). The XUV spectrum is measured after the CAMP using a flat field grating which images the harmonics on a MCP plus phosphor screen (PS).

last stage. The regenerative amplifier includes a second AOPDF, *Mazzler* from *Fastlite*, to compensate for gain narrowing during the amplification process. The pulses are finally compressed with a grating pair [49], resulting in 3.5 mJ pulses with a duration of 20 fs, when the full bandwidth is used, at 1 kHz repetition rate. When needed, for wavelength tuning or for reducing the width of the high-order harmonics, the bandwidth can be decreased to 70 nm or 50 nm resulting in pulses with a duration up to 45 fs. In order to reduce fluctuations and long-term drifts of the laser output, the pulses are characterized after the compressor with a *Wizzler* from Fastlite, based on self-referenced spectral interferometry [50, 51], and the result is fed back to the *Dazzler* to correct the phase of the pulses. In general this feed-back is performed manually when needed. However, for very long measurements, it is possible to do this automatically.

After the compressor, the pulses are transported over several meters in air until our experimental setup. Due to the large distance, the beam position is very sensitive to all sorts of environment fluctuations. To reduce this effect we use a beam-pointing stabilization system *Aligna* from *TEM Messtechnik*, which corrects the beam position at 100 Hz repetition rate. In addition, if short pulses are used, the propagation in air can slightly chirp the pulses. This can be pre-compensated by adding an additional negative dispersion with the *Dazzler*. The beam is then focused with a 50 cm focal length spherical mirror on a gas cell of varying length (usually 6 mm or 10 mm) filed with a noble gas (Ne, Ar, Xe) by a 1 kHz pulsed *Attotech* valve. The position of the gas cell can be adjusted in three dimensions with translation stages. The intensity of the laser in the cell is controlled using an iris before the focusing mirror. The XUV APT is then sent through a metallic filter in order to filter out the remaining IR. Different metallic filters have different transmission curves in the XUV which allows us to shape the spectrum and select which harmonic orders we want to use. Furthermore, the filters have negative dispersion in the XUV which partly compensates the attochirp. The HHG spectrum is measured using a flat field grating which directs the first diffraction order on a micro channel plate (MCP) detector behind which a phosphor screen is installed. Figure 2.8 shows a schematic representation of the HHG setup.

Chapter 3

Attosecond photoelectron interferometry

Light in the XUV spectral range is very strongly absorbed by matter. The development of synchrotron radiation light sources in the 60's allowed detailed studies of atoms and molecules using photoelectron spectroscopy. However, in traditional spectroscopy, only the spectrum, *i.e.* the modulous square of the electron wavepacket, is measured. As a consequence, phase information is lost. In this thesis, we use the interferometric technique, RABBIT, to measure both amplitude and phase of the emitted electrons. Initially introduced by Paul and coworkers [6] to measure the duration of the attosecond pulses produced by HHG, attosecond photoelectron interferometry has been, since then, successfully applied to investigate photoionization dynamics on the attosecond time scale. This chapter introduces the theory of laser-assisted photoionization, which is at the core of photoelectron interferometry, before introducing the RABBIT technique itself and how it is implemented experimentally.

1 Laser-assisted photoionization

All pulse characterization techniques in the visible and IR are based on the non-linear interaction of a short pulse with matter. In the case of XUV attosecond pulses, this is much more challenging due to the low efficiency of HHG and the low cross-section of XUV-XUV non-linear interaction [52–56]. It is, however, much easier to observe two-photon processes where one of the photons is in the XUV domain and the other photon is in the IR spectral range. An atom or molecule can absorb an XUV photon, followed by further absorption or emission of n additional IR photons: $A + \gamma_{XUV} \pm n\gamma_{IR} \rightarrow A^+ + e^-$. This process, called

laser-assisted photoionization, is a cornerstone of attosecond science.

1.1 Two-photon transitions

For moderate IR intensities, of the order of 10^{11} W/cm^2, only one XUV and one IR photon interact, resulting in a photoelectron spectrum (PES) composed of three peaks: a central peak corresponding to one-photon transition induced by the XUV and two smaller peaks, refered to as sidebands, corresponding to two-photon transitions where an XUV photon is absorbed and an IR photon is either absorbed or emitted.

Single channel

When the electron is ionized it reaches the continuum. As a first step, we consider that there is only one state accessible for a given energy in the continuum . In the following, we further restrict our discussion to the case where the XUV photon has an energy above the ionization threshold. In a two-photon transition, an XUV photon is absorbed, taking an electron from the ground state $|g\rangle$ to an intermediate continuum state $|\nu\rangle$, followed by further absorption or emission of an IR photon[1] taking the electron to a final continuum state $|f\rangle$. If both XUV and IR fields are linearly polarized along the $\hat{z}$ axis, the two-photon transition matrix element, calculated using second-order perturbation theory, can be defined as:

$$M_{fg}^{(\pm)}(\Omega) = \lim_{\varepsilon \to 0^+} \sum_{\nu} \frac{\langle f|\hat{z}|\nu\rangle \langle \nu|\hat{z}|g\rangle}{\hbar\Omega - E_\nu + E_g + i\varepsilon}. \tag{3.1}$$

In the following, the dependency of $M_{fg}^{(\pm)}$ on the XUV angular frequency Ω will not always be written explicitly in order to simply notations. The sum integral in Eq. 3.1 runs over both continuum states and real discrete states. This means that there is an infinite number of quantum paths leading to the final state $|f\rangle$. Nonetheless, if there is no discrete state (a resonance) in the vicinity of the intermediate states, only the state $|\nu\rangle$ that conserves energy, $E_\nu = E_g + \hbar\Omega$, contributes significantly. The two-photon transition can be decomposed in two steps: first the transition from the ground state to the intermediate continuum state and then the continuum-continuum (CC) transition between the intermediate and final states [9, 57, 58]. The $(\pm)$ superscript in the matrix element indicates whether the IR photon is absorbed $(+)$ or emitted $(-)$ in the second step.

[1] It is in principle possible that the IR interacts first, taking the electron to a virtual intermediate state, however, this process is in general very improbable and we do not consider it in the following.

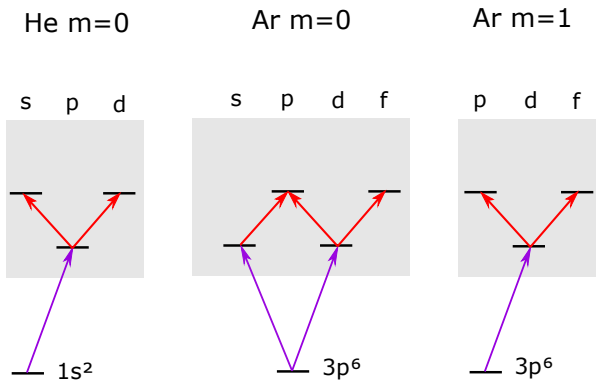

Figure 3.1: Example of channel-resolved two-photon transitions in He and Ar when the IR photon is absorbed.

Multiple channels

In reality, one cannot consider that for a given energy there is only one state in the continuum. Continuum states are scattering states and are characterized by the electron wave vector $\mathbf{k}$ such that we write the final state as $|f\rangle \equiv |\mathbf{k}\rangle$. Decomposing the scattering states into a sum of partial waves, the two-photon transition matrix element can be expressed as

$$M_{\mathbf{k}g}^{(\pm)} = \sum_{\lambda,L} M_{\lambda Lm}^{(\pm)} Y_{Lm}(\theta,\phi), \tag{3.2}$$

where λ and L are the angular momenta of the intermediate and final states, m is the magnetic quantum number of the ground state $|g\rangle$ and $Y_{Lm}(\theta,\phi)$ are the spherical harmonics, θ being the polar angle and ϕ the azimuthal angle. According to the selection rules for an electric dipole transition, the angular momenta of the final, intermediate and ground states are linked via $L = \lambda \pm 1$, and $\lambda = \ell \pm 1$, ℓ being the angular momentum of the ground state and $\ell, \lambda, L \geq 0$. In addition, for linearly polarized light, only intermediate and final states with the same magnetic quantum number as the ground state are accessible. Figure 3.1 shows examples of channel-resolved two-photon transitions in helium and argon where s, p, d and f refer to the angular momenta $\ell = 0, 1, 2, 3$ respectively.

Fano's propensity rule

In 1985, Ugo Fano showed that for one-photon transitions, from the ground state to the continuum, the channel in which the angular momentum increases dominates over the channel in which angular momentum decreases [59]. For example, this means that in argon, for $m = 0$, the transition $|3p^6\rangle \rightarrow |\epsilon d\rangle$ dominates over the transition $|3p^6\rangle \rightarrow |\epsilon s\rangle$. As with

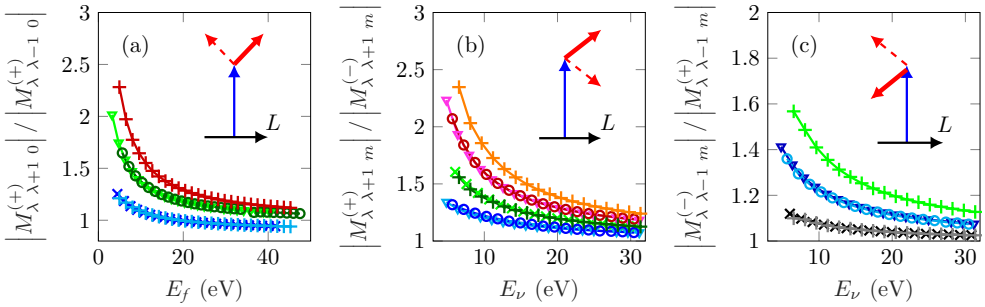

Figure 3.2: Propensity rules in laser-assisted photoionization in He $1s$ ($\times$), Ne $2p$ ($\triangledown$), Ar $3p$ ($\bigcirc$) and Kr $3d$ ($+$). The color of the curves indicates the angular momentum of the intermediate state in (a) and final state in (b), (c) [shades of grey s, shades of blue p, shades of green d, shades of red f, orange g]. (a) Probability ratio between increasing ($L = \lambda + 1$) and decreasing angular momentum ($L = \lambda - 1$) in the case of absorption of a photon from the intermediate state. (b) Probability ratio between absorbing and emitting a photon in the case of increasing angular momentum. (c) Probability ratio between emitting and absorbing a photon in the case of decreasing angular momentum. The insets present an energy and angular momentum diagram illustrating the propensity rule in each case. Figure from paper v.

most simple rules, there are also some notable exceptions for which the propensity rule does not work such as the $3p$ Cooper minimum in Ar [60]. However, in the case of CC transitions, there was, until recently, no study investigating the validity of this propensity rule. In addition, contrary to bound-continuum transitions, in CC transitions, the IR photon can also be emitted, which, due to time reversal symmetry, should result in the channel decreasing angular momentum dominating over the one increasing it.

In paper v, we investigate this problem theoretically. We calculate channel-resolved 2-photon transition matrix elements by solving the Dirac-Fock equation for noble gas atoms, (He, Ne, Ar outer shells and Kr $3d$ inner shell) and compare the moduli of the different matrix elements. First, we investigate the problem in the same way that Fano did, by comparing whether it is more probable to increase or decrease angular momentum when a photon is absorbed between two continuum states. We find that for CC transitions, Fano's propensity still holds true, since the ratio $|M^{(+)}_{\lambda(\lambda+1)m}|/|M^{(+)}_{\lambda(\lambda-1)m}|$ is larger than one [see Fig. 3.2(a)]. In addition, for a given energy, this ratio is universal, i.e. independent of the atomic species. It only depends on the angular momentum of the intermediate state. As the energy of the photoelectron increases, the ratio decreases, resulting in both channels having comparable amplitudes. We then compare, for a given angular channel in the continuum $|\lambda m\rangle \to |Lm\rangle$, whether it is more likely to absorb or emit a photon in the case where we increase angular momentum ($L = \lambda + 1$) or decrease angular momentum ($L = \lambda - 1$). As shown in Figs. 3.2(b) and (c), in the former case, absorption is dominant while in the latter case it is emission that

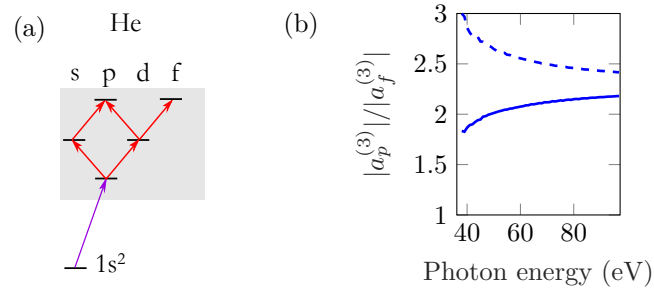

Figure 3.3: (a) Channel resolved three-photon transition in He, where both IR photons are absorbed. (b) Probability ratio between the transition amplitude to the p and f final states in the case absorption (solid curve) or emission (dashed curve) of two IR photon in the continuum.

is stronger. Again, the curves are universal and only depend on the intermediate angular momentum and energy.

The physical origin of this propensity rule is relatively simple. The local momentum of the electron in the continuum is given by

$$\hbar k(r) = \sqrt{2m_e[E - V(r)]} \tag{3.3}$$

where E is the photoelectron energy and $V(r) = V_0(r)+V_\ell(r)$, with $V_0(r)$ an atom specific potential and $V_\ell(r)$ the centrifugal potential defined as

$$V_\ell(r) = \frac{\hbar^2\ell(\ell+1)}{2m_e r^2}. \tag{3.4}$$

The strength of the transition between the intermediate and final states is highest when the difference in local momentum is the smallest. As a result, when the IR photon is absorbed, resulting in a higher total energy E, increasing angular momentum is favoured as it increases the centrifugal potential. In the case where the IR photon is emitted, the total energy decreases thus favouring the transition to a lower angular momentum state. It is worth mentioning that another contribution can affect these results. Indeed, one also needs to take into account the angular part of the matrix elements. At low energy this contribution is small relative to the radial matrix element. However, at high energy, when $E \gg V(r)$, the radial part becomes negligible and the angular part dominates. This results in the fact that in He, above 20 eV, when an IR photon is absorbed, it is slightly more probable to decrease angular momentum than to increase it [see Fig. 3.2(a)]. This means that, in this energy range, both absorption and emission processes favour decreasing angular momentum. However, the probability of increasing angular momentum remains stronger for absorption than for emission as shown in Fig. 3.2(b).

Finally, in paper VI we also investigate, in the high energy limit, three-photon transitions in which two IR photons are absorbed or emitted in the continuum, leading to a more com-

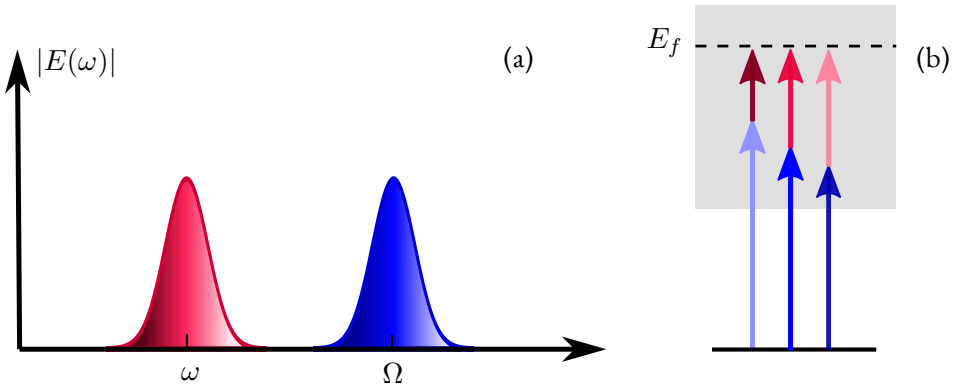

Figure 3.4: (a) Both XUV (blue) and IR (red) fields have a Gaussian distribution of their spectral amplitude. (b) A given final state with energy E_f can be reached via multiple combinations of IR and XUV frequencies.

plex energy diagram as showed in Fig. 3.3(a) for helium. In particular, starting from the first intermediate state in the p continuum, there are two interfering paths leading to the final state with angular momentum $L = 1$ and only one path leading to the final state with angular momentum $L = 3$. In this situation, it is not clear which final state will the electron most likely reach. One the one hand, according the Fano's propensity rule, individually, the transitions $p \to d$ and $d \to f$ are the most likely in the case of photon absorption and the least likely in the case of emission. On the other hand, two, individually weaker, paths lead to the p final state. Figure 3.3(b) shows that these two paths interfere constructively such that the electron is more than twice as likely to end in the p state than in the f state, and this both in the absorption and emission cases. Nonetheless, we still observe that the p state is more favoured in the case of emission than in the case of absorption, as expected from Fano's propensity rule.

1.2 Effects of the spectral properties of the light fields

So far we have restricted the discussion of laser-assisted photoionization to the intrinsic properties of the atoms. However, the photoelectron signal also depends on the spectrum of the XUV and IR fields.

In the case where both XUV and IR pulses are long, we can assume that their spectra are monochromatic and the total transition probability amplitude to reach the final state is then simply given by

$$\mathcal{A}_{\mathbf{k}g}^{(\pm)}(\tau) = -\frac{ie^2}{\hbar} E_{\mathrm{XUV}}(\Omega) E_{\mathrm{IR}}(\omega) e^{\pm i\omega\tau} M_{\mathbf{k}g}^{(\pm)}, \tag{3.5}$$

where τ is the delay between the pump and the probe pulses. Here the phase of the IR field is written explicitly in order to easily differentiate between absorption and emission processes. In our experiments, the light pulses are short such that the monochromatic approximation is not always good [61, 62]. Instead, as shown in Fig. 3.4(a), both XUV and IR pulses are composed of a distribution of frequencies. As a result, several final states with different energies are accessible. In addition, as shown in Fig. 3.4(b), each final energy can be reached via multiple paths combining different XUV and IR photon energies. The total transition probability amplitude to reach the final state is hence given by the coherent addition of all these paths [62]

$$\mathcal{A}_{\mathbf{k}g}^{(\pm)}(\Omega_{\mathbf{k}g},\tau) = -\frac{ie^2}{\hbar}\int_0^\infty E_{\mathrm{IR}}(\Omega_{\mathbf{k}g}-\Omega)e^{i(\Omega_{\mathbf{k}g}-\Omega)\tau}E_{\mathrm{XUV}}(\Omega)M_{\mathbf{k}g}^{(\pm)}(\Omega)\,\mathrm{d}\Omega. \quad (3.6)$$

Here the IR photon energy is defined with respect to the final energy and the XUV photon energy in order to ensure conservation of energy. In order to calculate the energy resolved two-photon transition amplitude to the sidebands, one has to calculate this integral for every final energy

Let us now investigate the case where the intermediate and final continua are flat and the XUV and IR pulses are Gaussian and Fourier limited. In this situation, the two-photon transition amplitude has an analytic form [62]

$$\mathcal{A}_{\mathbf{k}g}^{(\pm)}(\tau) \propto \mathcal{F}(\tau)e^{\pm i\omega\tau}w\left[z(\Omega_{\mathbf{k}g},\tau)\right], \quad (3.7)$$

where $\mathcal{F}$ is a form factor, $z(\Omega_{\mathbf{k}g},\tau)$ is a complex parameter and $w(z) = e^{-z^2}\mathrm{erfc}(-iz)$ is the Faddeeva function with $\mathrm{erfc}(z)$ the complex error function. The exact form of the two-photon transition amplitude and the definition of the aforementioned quantities are given in Appendix I and the complete details on the derivation can be found in Ref. [62]. Unlike in Eq. 3.5, here the two-photon transition amplitude decays as a function of delay via $\mathcal{F}(\tau)w[z(\Omega_{\mathbf{k}g},\tau)]$, reflecting the fact that two-photon excitation is only possible when both XUV and IR pulses are temporally overlapped. This model can be extended to chirped pulses (or in general pulses with arbitrary amplitude and phase) by decomposing the pulses in a sum of Fourier limited Gaussian pulses with different carrier-to-envelope phases as we show in paper IV.

2 Photoelectron interferometry: RABBIT

So far we have considered a monochromatic or Gaussian XUV spectrum, however, HHG produces a harmonic comb. In that case, the PES will also have a comb structure. When

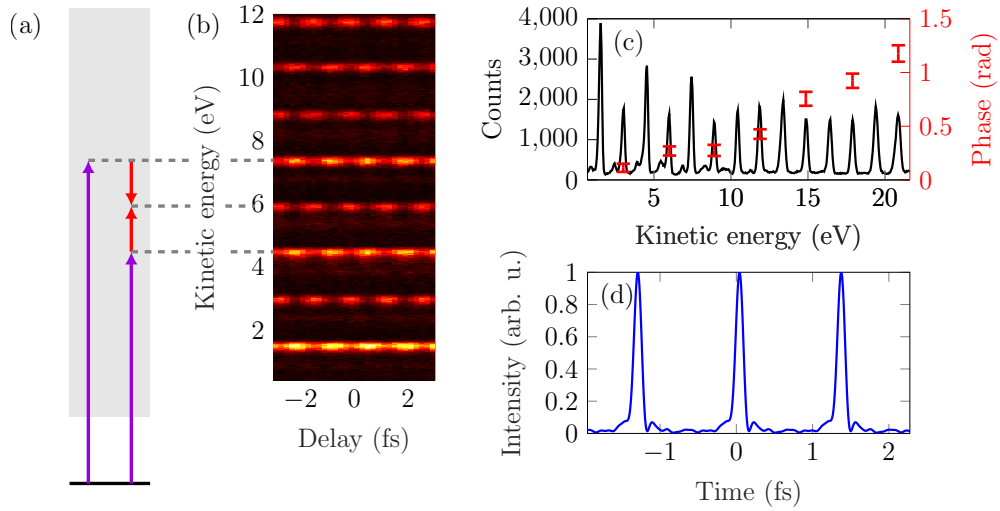

Figure 3.5: Characterization of an attosecond pulse train. (a) Schematic representation of the RABBIT technique. (b) Low energy part of a RABBIT scan in Ne from harmonics generated in Ne. (c) Delay integrated photoelectron spectrum and phase measured at the sidebands. (d) Reconstructed attosecond pulse train.

we add the IR field, we then get additional sidebands as discussed in the previous section. However, in this case, because the two consecutive harmonics are spaced by the equivalent of two IR photons, a given sideband can be reached via two quantum paths as shown in Fig. 3.5(a): absorption of one harmonic plus absorption of one IR photon or absorption of the following harmonic plus emission of one IR photon. As a result the signal of sideband q, which corresponds to the absorption of a photon with an effective energy $q\hbar\omega$, is given by

$$\begin{aligned} S_q &= \left|\mathcal{A}_{q-1}^{(+)} + \mathcal{A}_{q+1}^{(-)}\right|^2 \\ &= \left|\mathcal{A}_{q-1}^{(+)}\right|^2 + \left|\mathcal{A}_{q+1}^{(-)}\right|^2 + 2\left|\mathcal{A}_{q-1}^{(+)}\right|\left|\mathcal{A}_{q+1}^{(-)}\right|\cos\left(2\omega\tau - \Delta\varphi\right), \end{aligned} \tag{3.8}$$

where $\mathcal{A}_{q\mp1}^{(\pm)}$ is the two-photon transition amplitude corresponding to absorption of harmonic $q \mp 1$ and absorption $(+)$ or emission $(-)$ of an IR photon. As a result of the interference of the two quantum paths, the sideband intensity depends on the delay and oscillates at the frequency 2ω. The phase of these oscillations, $\Delta\varphi$, can be decomposed into two contributions, $\Delta\varphi = \Delta\varphi_{\mathrm{XUV}} + \Delta\varphi_{\mathrm{A}}$ which are defined as:

$$\begin{aligned} \Delta\varphi_{\mathrm{XUV}} &= \arg\left[E_{\mathrm{XUV}}(\Omega_{q+1})\right] - \arg\left[E_{\mathrm{XUV}}(\Omega_{q-1})\right] \approx 2\omega\tau_{\mathrm{XUV}}, \\ \Delta\varphi_{\mathrm{A}} &= \arg\left[M_{\mathbf{k}g}^{(-)}(\Omega_{q+1})\right] - \arg\left[M_{\mathbf{k}g}^{(+)}(\Omega_{q-1})\right], \end{aligned} \tag{3.9}$$

with $\Omega_{q\pm1} = (q \pm 1)\omega$. $\Delta\varphi_{\mathrm{XUV}}$ is the XUV group delay introduced in Eq. 2.6 and $\Delta\varphi_{\mathrm{A}}$ is the phase difference between the two-photon transition matrix elements, and is called atomic phase. By fitting the sideband oscillation with the equation above, we can extract the phase offset for the different sidebands as shown in Fig. 3.5(b). The phase difference formally depends on the emission angle $\hat{k}$ via the matrix elements in $\Delta\varphi_A$. This will be discussed in detail in chapter 6, however, in the following we restrict the discussion to angle-integrated measurements. In the case of ionization to a flat, featureless, continuum, the variation of the total phase, $\Delta\varphi$, with sideband order can be mostly attributed to the XUV group delay. For example, the close-to-linear phase variation shown in Fig. 3.5(b) is due to the attochirp. Having both amplitude and phase information it is then possible to reconstruct the attosecond pulse train as shown in Fig. 3.5(c). This interferometric method was first suggested by Véniard *et al.* [63], as a mean to measure the phase variation between consecutive harmonics and was then implemented experimentally by Paul and coworkers [6] to demonstrate that the radiation emitted by HHG corresponds to a train of attosecond pulses. The name RABBIT(T) was suggested by Muller in 2002 [64]. Over the last two decades, the main application of the RABBIT technique has shifted from measuring and characterizing the attosecond pulse trains to studying attosecond photoionization dynamics in matter.

2.1 Rainbow RABBIT

As discussed in section 1.2, the sidebands have a certain spectral width. In the original implementation of RABBIT, for each delay, the sideband signal was integrated over the width of the photoelectron peak in order to increase the signal-to-noise ratio. However, in principle, it is possible to measure the phase for every energy point in the sideband. Therefore, equations 3.8 and 3.9 become energy dependent. This energy-resolved version of RABBIT, dubbed Rainbow RABBIT, was developed recently by Gruson and coworkers [13][2].

The Rainbow RABBIT technique can be used to study fast phase variations across the sideband resulting from resonances or overlapping photoelectron peaks which originate from different ionization channels and was used in papers I,II,VII-X. However, this relies on the fact that the variation of the XUV spectral phase across the sideband width is negligible. For the Rainbow RABBIT technique, the difference in attochirp between the two adjacent harmonics results in a general phase offset and hence does not lead to a phase variation across the sideband. However, the XUV femtochirp, which varies quickly across one harmonic, may affect the energy-resolved phase measurments in the sideband. In paper IV, we study the effect of the femotchirp ϕ_q'' in detail. For low-order harmonics, the difference in femtochirp, $\Delta\phi_q''$, between consecutive harmonics is large enough so that a small quadratic variation of the sideband phase can be observed the in our simulations. However, as can be seen in Fig. 3.6(a),

[2] We note that a spectrally resolved analysis of the sidebands had already been used by Guénot *et al.* in 2012 [57].

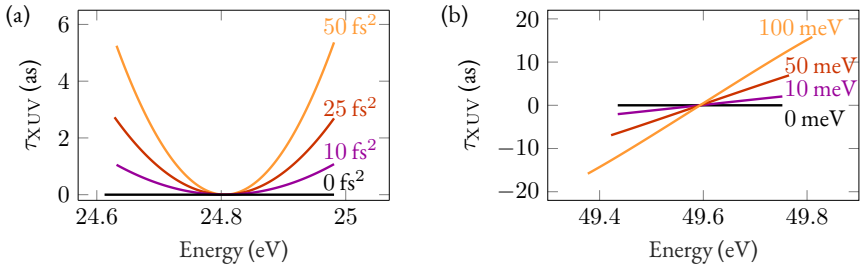

Figure 3.6: (a) Calculated delay variation for different values of $\Delta\phi_q''$. There is no blueshift. (b) Calculated delay variation for different blueshifts. The femtochirp of both harmonics is the same (-50 fs^2). Figure adapted from paper IV.

this is a small effect and can often be neglected. For higher-order sidebands, the femtochirp of consecutive harmonics is approximately the same. Therefore, in this case the phase difference measured in the sideband is constant. However, if during the generation, the fundamental IR field generating the harmonics is blueshifted by the plasma, the two-photon transitions amplitudes, $\mathcal{A}_{q-1}^{(+)}$ and $\mathcal{A}_{q+1}^{(-)}$, induced by the probe pulse, which is not blueshifted, may not perfectly overlap. This results in a linear phase variation across the sideband as shown in Fig. 3.6(b). This effect can be quite strong and must sometimes be accounted for in the data analysis.

2.2 Conditions and limitations of RABBIT

As we will show in chapters 4 and 5, the RABBIT and Rainbow RABBIT techniques are very powerful and versatile techniques to investigate photoionization dynamics. However, until recently there was no comprehensive study of the technique itself. In paper IV, we performed an in-depth study of the RABBIT technique, discussing how to optimize its performance and some of its limitations.

The first limitation, is related to the harmonic chirps and was discussed above. In addition, if the attosecond pulse train is generated by very short pulses, the chirp rate of different harmonics varies very strongly as a function of harmonic order [see Fig. 2.5(a)]. We show in paper IV that this leads to strong distortion of the sidebands as their central energy shifts as function of the delay. As a result, for very short driving pulses, generating only few attosecond pulses, the RABBIT technique does not work well [65].

The second limitation is linked to the fact that the PES results from the spatial integration over the interaction region. This means that the conditions should be kept as constant as possible across the interaction volume. As a result, it is important to match, to the extent possible, the XUV and IR wave fronts in the interaction region [66]. In addition, it has been

shown that HHG is subject to strong spatial-temporal couplings [36, 38] and great care has to be taken when focusing the XUV light [67–69]. As a general rule, it is strongly beneficial to minimize the interaction volume by confining the gas in a small region. However, further studies are needed to better understand the effects of spatial integration on RABBIT measurements and, in general, on photoelectron-based characterization techniques used in attosecond science.

The third limitation is linked to stability of the setup. Since XUV flux is not a very high, we only detect a few electrons per shot at 1 kHz. Therefore, in order to measure a PES with a decent signal to noise ratio, for each delay, we must acquire for some time ranging from tens of seconds to one hour. As a result, it is crucial that the intensity and pump-probe delay are stable during the acquisition of the RABBIT scan. In general, this poses the problem of the degree of coherence of the measured PES. RABBIT assumes full coherence and in some cases this can lead to inaccurate results as shown by Bourassin-Bouchet and coworkers [70]. As a response to this problem, a few different techniques have been developed in order to measure the degree of coherence of attosecond pulse trains [70, 71]. The role of decoherence in some of our measurements will be addressed in more detail in chapter 5.

3 Experimental methods

Experimentally, measuring a RABBIT trace requires a stable optical interferometer and an electron detector to record the PES. These are introduced in the following.

3.1 Attosecond optical interferometer

As shown in the previous section, in the RABBIT scheme, the intensity of the sidebands oscillates as a function of the delay with a frequency 2ω which, in our case, corresponds to a period of approximately 1.33 fs. As a result, it is important that the delay between the XUV APT and the IR pulse can controlled and stabilized with attosecond precision. This is achieved by using a Mach-Zender type interferometer that is schematically represented in Fig. 3.7. A beam-splitter reflects 70% of the incoming pulse which is used for generating the harmonics as described in chapter 2. In the other arm, 30% of the IR is transmitted through the beam-splitter and is delayed with respect to the "pump" pulse generating harmonics, first with a manual rough delay stage and then with a mirror on a piezo-electric mount that allows us to tune de delay with attosecond precision. The generated attosecond pulse train and the delayed IR pulse are then recombined using a drilled mirror in which the IR is reflected while the XUV goes through the central hole. Finally both pulses are focused in the interaction chamber using a gold-coated toroidal mirror in grazing incidence. In order for the XUV and

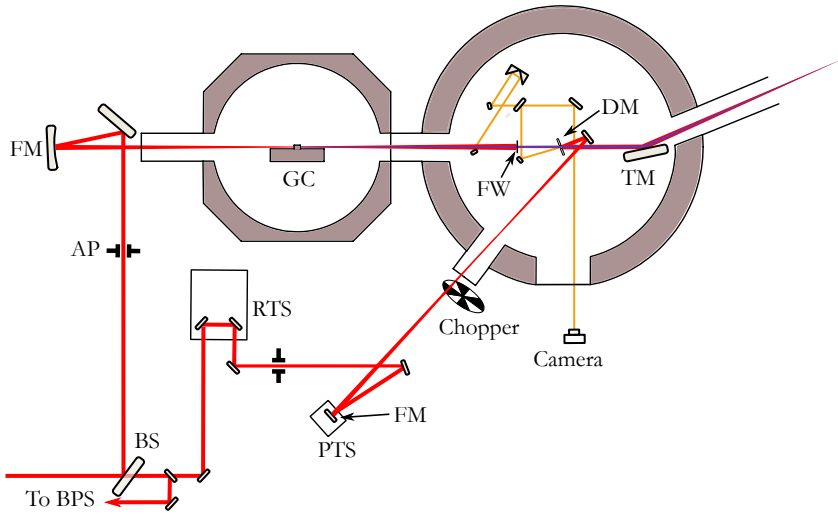

.

Figure 3.7: Figure of the optical setup. The following abbreviations are used in the figure: AP, aperture; BPS, beam-point stabilisation; BS, beam-splitter; DM, drilled mirror; FM, focusing mirror; FW, filter-wheel; GC, gas cell; PTS, piezoelectric translation stage; RTS, rough translation stage; TM, toroidal mirror. The path in yellow corresponds to the interferometer used to monitor the delay. Figure modified from [72]

the IR to be focused at the same position in the interaction chamber, the probe pulse is also focused in the vacuum chamber by a spherical mirror with 50 cm focal length. In both arms of the interferometer an iris is used to control the intensity. However, modifying the iris size in the probe arm is not the best way of changing the intensity since it also modifies the radius of the IR in the interaction region. For this reason, for papers II,VIII, which required very high spectral resolution, an additional $\lambda/4$ wave-plate and a polarizer were introduced in order to modify the intensity without affecting the size of the IR focus. In some cases, when several ionization channels are available, resulting in congested PES, it is convenient to periodically measure a PES with only the XUV. For this purpose, we use a chopper which can block every other IR probe pulse. This chopper was used in papers VII and IX.

In order to read and control the delay, a fraction of the IR from the pump and probe arms of the interferometer are recombined with a small angle on a CCD camera producing an interference fringe pattern whose phase is related to the delay between the two pulses. This second interferometer is represented by the yellow optical path in Fig. 3.7. While it is not possible to determine the zero delay accurately, it is however possible to monitor the variation of the relative delay. A feedback loop acting on the piezo-electric stage in the probe arm allows stabilizing the delay between the two arms. However, the interferometer stabilized in this process is not exactly the one used for the RABBIT measurements. The small optical path

difference between the two interferometers can lead to long-term drifts. Our beam-pointing stabilization system strongly helps reducing this effect. Nonetheless, when the laser is first sent in the interferometer, we observe drifts of about 3 fs between the two interferometers over the first 45 min due to the thermal expansion of the optical components in the beam path. The fact that most of our interferometer is in air has the advantage that the optical components reach thermal equilibrium relatively quickly, while it would take several hours if the interferometer was fully in vacuum. After this thermalization time, the delay in the RABBIT interferometer is measured to be stable to about 40 as root-mean-square error by an out-of-loop measurement over one hour. We note that this value corresponds to the phase measured at 100 Hz by the camera, and therefore each data point is averaged over 10 shots. At the time of writing this thesis, we plan on changing the interferometer design to further increase the stability. The new interferometer design will be strongly inspired from the one suggested by David Kroon in [72]. This design has the same parity of mirrors in both arms reducing the effect of spatial drifts. In addition, in Kroon's design, possible vibrations of the recombination mirror could be measured and compensated for. This design could also be adapted to include novel delay stabilization schemes such as the one implemented in Ref. [73] which uses a Michelson interferometer together with balanced homodyne detection with fast photodiodes to stabilize the interferometer at 300 Hz. Another possibility would be to use a line Camera which can operate in the kHz regime.

3.2 Electron detectors

There are different ways to detect photoelectrons, each technique having different advantages and drawbacks. In this thesis, photoelectrons were measured with two different spectrometers: a MBES and a VMIS. The first one benefits from a high spectral resolution while the second one offers angular resolution.

Magnetic bottle electron spectrometer

The magnetic bottle electron spectrometer (MBES) is a time-of-flight (TOF) spectrometer and was used in papers I,II,VII-X. Assuming that the electron detector, a MCP, is at a distance L from the focus of the XUV, the kinetic energy of a photoelectron can be deduced from the time t it takes to reach the detector:

$$E_k = \frac{mL^2}{2t^2}. \tag{3.10}$$

The signal from the MCP is then digitalized by an acquisition card and the data is compressed and saved on a computer. Since the acquisition card has a finite sampling frequency f, the resolution of the TOF spectrum is limited to $\delta t = 1/f$ and that of the kinetic energy spectrum is limited to $\delta E \propto L^2 t^{-3} \delta t$. As a result, in order to have the best spectral resolution

one needs an acquition card with a high sampling frequency and a long flight distance, L. In addition, the spectral resolution decreases as a function of the electron kinetic energy since the time the electrons take to reach the detector decreases. If we want to study high kinetic energy photoelectrons with high spectral resolution, it is possible to slow them down by applying a negative voltage at the entrance of the flight tube which then needs to be taken into account when converting from TOF to kinetic energy.

When an atom or a molecule is photoionized, photoelectrons can be emitted in almost all directions. If nothing is done to try to collect the photoelectrons, only very few will be effectively transmitted through the flight tube and hit the MCP, leading to a low detection efficiency. The principle of the MBES is to use magnetic fields to collect and guide the photoelectrons from the XUV focus to the MCP detector in order to increase the detection efficiency [74–76]. The MBES used in this thesis is based on the design of [76] which has a 2 m long flight tube and a 4π solid angle collection efficiency. Figure 3.8(a) shows the working principle of the MBES. A strong diverging magnetic field is generated by a permanent NdFeB magnet placed millimetres away from the interaction region, with a maximum field strength of $\sim 1\,\mathrm{T}$ at its surface. It yields field strengths between 100 mT to 1 T at the interaction region, depending on the exact distance. The strong diverging magnetic field acts as a magnetic mirror reflecting the electrons emitted in the direction opposite to the flight tube. In the flight tube, a weak linear magnetic field ($\sim 100\ \mu\mathrm{T}$) is created, using a solenoid, to guide the electrons to the MCP. The flight tube is inside a μ-metal tube to prevent the Earth's magnetic field to distort the magnetic field created by the solenoid. The resolution of the spectrometer is usually given by $E/\delta E$, which characterizes how fast the spectral resolution decreases with kinetic energy. In our case, we estimate it to be around $E/\delta E = 80$, based on the fact that we can observe the spin-orbit splitting in argon (180 meV) up to approximately 10 eV kinetic energy. Nonetheless, at very low kinetic energy, our spectral resolution is limited by the integration over the interaction volume. We estimate that the best spectral resolution that we can achieve at low energy is around 70 meV. The spectral resolution can be further improved by applying a deconvolution algorithm. For this reason, we have implemented a blind iterative deconvolution algorithm based on the Lucy-Richardson method [77, 78].

Velocity map imaging spectrometer

While the MBES offers high spectral resolution, the PES is integrated over all emission angles. In papers III and V, we use a velocity map imaging spectrometer (VMIS), designed by Rading and coworkers [79], in order to study photoionization dynamics as a function of the emission angle of the photoelectrons with respect to the laser polarization. The VMIS uses a set of electrodes (a repeller and an extractor) to direct the photoelectrons on an MCP behind which is placed a phosphor screen [80]. The voltages on the repeller and extractor are set such that

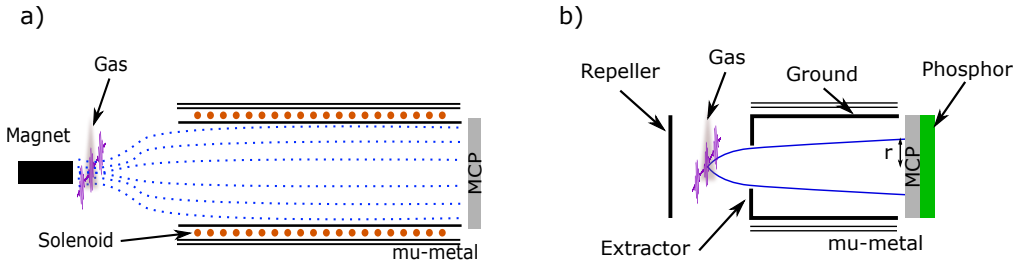

Figure 3.8: Photoelectron detectors. (a) Schematic representation of the MBES. The blue doted lines correspond to the magnetic field. (b) Schematic representation of the VMI. The blue lines represent two possible trajectories for an electron with a given kinetic energy E_k arriving at the MCP on a disk of radius r.

the 3-dimensional (3D) momentum distribution of the photoelectrons is projected on the 2-dimensional (2D) phosphor screen. As a result, photoelectrons with a kinetic energy E_k form a disk of radius

$$r = \sqrt{\frac{L^2 E_k}{eV}} \tag{3.11}$$

where L is the length of the flight tube which is here 350 mm and V is the voltage difference between the electrodes.

In general, photoionization is most probable along the polarization, giving rise to photoelectrons with an initial momentum parallel to the MCP. As a result, most of the electrons of a given kinetic energy arrive on a ring of radius r, rather than a homogeneous disk. Therefore, for a given radius, the angular dependence of the signal reflects the photoelectron angular distribution (PAD). Nonetheless, in order to recover the full 3D PAD, it is necessary to invert the projected distribution. If the polarization of the light fields is linear and parallel to the detection plane and if the PAD has a cylindrical symmetry around the polarization axis, it is possible to mathematically invert the 2D projection using the inverse Abel transform. There are multiple methods to perform this inversion: onion peeling [81], iterative algorithm [82], pBASEX [83]. For the results presented in this thesis pBASEX was used to perform the inversion. The pBASEX method relies on the fact that any angular distribution with cylindrical symmetry can be described as

$$\frac{d\sigma}{d\Omega} = \frac{\sigma_0}{4\pi}\left[1 + \sum_{n=1}^{\infty} \beta_i P_i(\cos\theta)\right], \tag{3.12}$$

where σ is the fully differential cross-section, σ_0 is the total cross-section, Ω is the solid angle, θ is the polar angle, P_n is the n^{th} Legendre polynomial and β_n are the asymmetry parameters. The algorithm generates a 3D distribution, projects it in a 2D plane and tries to fit the measured 2D projection by adjusting the asymmetry parameters β_n.

Chapter 4

Non-resonant photoionization

In this chapter we investigate the photoionization dynamics when an electron is sent to a flat continuum following the absorption of an XUV photon. It is important to clarify that, because time is not an observable in quantum mechanics, it is not possible to associate a time to the transition from the ground state to the continuum [84, 85]. Instead, once the electron is ionized, it propagates in the ionic potential as it moves away from the core. This leads to the electron being delayed by a few tens to hundreds of attoseconds compared to the same electron propagating freely in vacuum. This means that photoionization time delays probe the potential in which the electron propagates and thus are very sensitive to electron correlation effects [85–88]. These delays were measured for the first time for atomic targets in 2010 by Schultze and co-worker [22], shortly followed by Klünder *et al.* [9]. These measurements triggered a lot of theoretical and experimental attention since they opened the possibility to study photoionization in the time domain. In the following, we introduce photoionization time delays and discuss how they can be measured with the RABBIT technique before presenting our results in neon and argon.

1 Theory of photoionization time delays

The concept of time delay was first introduced from a purely theoretical perspective within the framework of scattering theory by Eisenbud and Wigner [89]. A wavepacket propagating in a short range potential $V(r)$ acquires a phase shift $\phi = 2\eta$ compared to a wavepacket propagating in free space. This phase shift originates from the fact that, as the electron propagates in the potential, its local momentum, and hence phase, varies spatially (see Eq. 3.3). As a consequence, due to scattering, the outgoing wavepacket acquires an effective

group delay τ_S defined similarly to that of an optical wavepacket

$$\tau_S = \hbar \frac{\partial \phi}{\partial E} = 2\hbar \frac{\partial \eta}{\partial E}. \tag{4.1}$$

In the case of photoionization, the situation is similar. When an electron is photoionized, it propagates away from the ion core, accumulating a phase. This can be viewed as a half-scattering process, since the EWP only propagates on half of the potential ($r > 0$). However, in this case, the range of the Coulomb interaction is infinite. Unlike short range potentials, it is not possible to determine a radius after which the phase shift has converged to a stationnary value. Nonetheless, for a given angular mometum L, it is possible to evaluate the asymptotic radial wavefunction R_L of the EWP which is given by [58, 90]

$$\lim_{r\to\infty} R_L(k,r) = \sqrt{\frac{2}{\pi k}} \frac{1}{r} \sin\left[kr + \frac{Z\ln(2kr)}{k} + \eta_L(k) - \pi L/2\right], \tag{4.2}$$

where Z is the charge of the ion. Here, η_L is the scattering phase, which can be decomposed into two contributions $\eta_L = \sigma_L + \delta_L$, where σ_L is the universal Coulomb phase shift and δ_L is an atom-specific phase shift originating from modifications of the short range potential due to electron correlations. In addition, the long-range Coulomb potential gives rise to an r-dependent phase, $Z\ln(2kr)/k$. As a result, the delay of the wavepacket relative to a free electron is given by[1]

$$\begin{aligned} \tau_{EWP} =& \hbar \frac{\partial}{\partial E}\left(\frac{Z\ln(2kr)}{k} + \eta_L(k) - \pi L/2\right) \\ =& \hbar \frac{\partial}{\partial E}\left(\frac{Z\ln(2kr)}{k}\right) + \hbar \frac{\partial \eta_L}{\partial E} \\ =& \Delta\tau_{Coul}(k,r) + \tau_W(k,L), \end{aligned} \tag{4.3}$$

where $\tau_W(k,L)$ is called the Wigner time delay and is a finite quantity which can be interpreted in the same way as the time delay introduced by Wigner for a short range potential (Eq. 4.1). The term $\Delta\tau_{Coul}(k,r)$ is a universal position-dependent delay which accounts for the outgoing electron progressively slowing down while moving away from the nucleus due to the attractive Coulomb potential [85]. Because the Coulomb potential reaches infinitely far, it is not meaningful to compare the delay of the outgoing EWP to a free EWP, since it is not possible to define a radius after which the phase shift is stationary. Nonetheless, one can compare the delay between two EWPs originating from two different photoionization processes such that we can eliminate $\Delta\tau_{Coul}(k,r)$ and study the difference between the Wigner time delays $\tau_W(k,L)$.

[1] Note that τ_S in Eq. 4.1 is the time delay for a complete scattering process while here τ_{EWP} is the time delay acquired by the EWP after photoionization. This also explains the that factor 2 in Eq.4.1 is not present here.

Finally, it is worth mentioning that, in the case of photoionization of negative ions, one would recover the simple situation discussed initially by Wigner. In this case, the atom would be left in its neutral form hence resulting only in a short range potential. This has been investigated theoretically in recent years [91, 92]. However, so far, there has been no experimental study due to the difficulty of combining a negative ion source with an attosecond photoelectron spectroscopy setup.

2 Measuring photoionization time delays with RABBIT

In chapter 3 we have shown that the RABBIT technique can be used to measure the phase of APTs, and in particular the attochirp, assuming that the atomic phase was negligible. Now we want to investigate whether it is also possible to measure photoionization time delays using the RABBIT technique. For this, we need to relate the phase of the two-photon transition matrix element to the phase shifts discussed in the previous section and understand the effect of the additional IR field on the phase acquired by the electron.

2.1 RABBIT measurements with a single channel

For a given channel, the asymptotic phase of the two-photon transition matrix element is given by [58]

$$\arg\left(M^{(\pm)}_{L\lambda m}\right) = \eta_\lambda(\kappa^{(\pm)}) + \phi_{cc}(\kappa^{(\pm)}, k) - \lambda\frac{\pi}{2}, \tag{4.4}$$

where $\kappa^{(\pm)}$ and k are the wave vectors of the electron in the intermediate and final states respectively, and $\phi_{cc}(\kappa^{(\pm)}, k)$ is the phase induced by the IR-driven continuum-continuum transition in the long Coulomb tail [58][2]. The asymptotic approximation works best at high kinetic energy but its validity extends down to kinetic energies of the order of ∼20 eV. At lower kinetic energy, the continuum-continuum phase depends on the intermediate and final angular momenta [58]. This has been recently measured by Fuchs et al. in helium [93]. Interestingly, τ_{cc} is largely independent of angular momentum as demonstrated in [58] because the angular momentum dependence of ϕ_{cc} cancels when taking the difference between absorption and emission.

Using the result in Eq. 4.4, and considering a single angular momentum channel, we get an expression for the atomic phase $\Delta\varphi_A$ (Eq. 3.9):

$$\Delta\varphi_A(\lambda) = \Delta\eta_\lambda + \Delta\phi_{cc}, \tag{4.5}$$

[2] Note that, since $\kappa^{(\pm)}$ is the momentum of the intermediate case and $(\pm)$ designates whether the IR photon is absorbed or emitted, $\kappa^{(+)} < \kappa^{(-)}$.

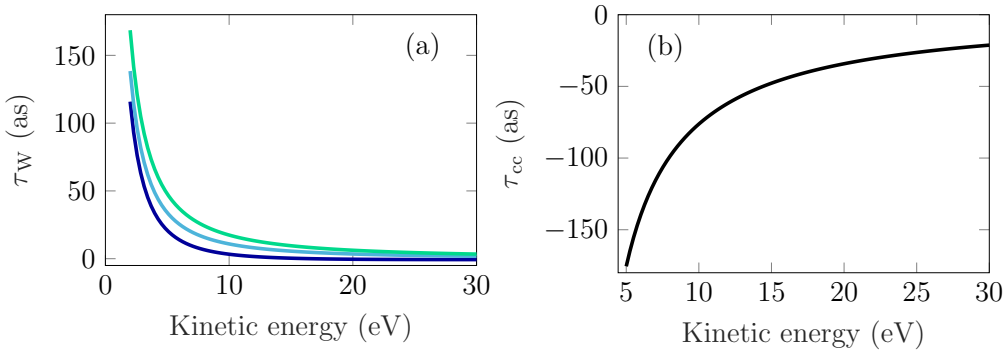

Figure 4.1: Photoionization time delays. (a) Finite difference approximation of the Wigner time delays for hydrogen for $L = 0$ (dark blue), $L = 1$ (light blue) and $L = 2$ (green). (b) Finite difference approximation of the continuum-continuum delay calculated using the analytical formula in [58].

which we can insert in the RABBIT equation, yielding

$$S_q \propto \cos\left(2\omega[\tau - \tau_{XUV} - \tau_{W_\lambda} - \tau_{cc}]\right), \tag{4.6}$$

where τ_{cc} and τ_{W_λ} are given by $\tau_{cc} \approx \Delta\phi_{cc}/(2\omega)$ and $\tau_{W_\lambda} \approx \Delta\eta_\lambda/(2\omega)$, which correspond to the finite difference approximation of the scattering time delays. The phase measured with the RABBIT technique is hence sensitive to the Wigner time delay, although it is also influenced by the attochirp and the measurement induced τ_{cc}.

Figure 4.1(a) shows the Wigner time delay for different angular momenta of the electron in hydrogen. In the case of hydrogen there is no short range correction to the Coulomb potential so that the Wigner time delay is given by the energy derivative of the Coulomb phase σ_L, which has an analytical expression [90]. Although here the Wigner delay is calculated for hydrogen, this contribution is present in all other atoms on top of which corrections due to electron correlations have to be taken into account. At low energy, as we get closer to the threshold, the Coulomb time delay increases very fast. For this reason, in paper X, where we are intrerested in measuring photoionization time delays induced by electron correlations close to the threshold, we subtract this contribution in order to make more visible the contribution of the short range potential to the total time delay. At higher kinetic energy, this delay quickly becomes negligible. In Fig. 4.1(b) we present the continuum-continuum delay τ_{cc} calculated using the analytical formula in [58]. Unlike the Wigner delay, this is a universal contribution which is the same for all atoms. This can be understood from the fact that for high enough electron momentum, where the asymptotic ϕ_{cc} approximation is valid, the continuum-continuum transition occurs at a large distance from the nucleus such that it is not sensitive to the atom-specific short range potential, including the centrifugal potential.

2.2 RABBIT measurements with multiple channels

So far, we have only considered a single angular momentum channel. If there is more than one channel, the situation becomes more complicated. For now we will restrict the discussion to angle-integrated measurements. The effect of multiple channels on angle-resolved measurements will be discussed in chapter 6.

For angle-integrated measurements, contributions from different final scattering states have to be summed incoherently. As a result, the total RABBIT scan corresponds to the incoherent sum of different RABBIT scans S_{Lm} for the different final scattering states:

$$S_q = \sum_{L,m} S_{Lm}, \tag{4.7}$$

with

$$S_{Lm} = \left| \sum_{\lambda} \left(\mathcal{A}^{(+)}_{L\lambda m} + \mathcal{A}^{(-)}_{L\lambda m} \right) \right|^2 . \tag{4.8}$$

where $\mathcal{A}^{(\pm)}_{L\lambda m}$ are the channel-resolved two-photon transition amplitudes defined as in Eq. 3.6 except that the transition matrix element $M^{(\pm)}_{\mathbf{k}g}$ is replaced by the channel specific transition matrix element $M^{(\pm)}_{L\lambda m}$.

As an example, we can compare helium and argon for which we have presented the different angular channels in Fig. 3.1. In helium, there are two final scattering states but only one intermediate one. Therefore, the RABBIT scans associated with the two final states will have the same atomic phase, $\Delta\varphi = \Delta\eta_1 + \Delta\phi_{cc}$, such that it is possible to accurately extract the one-photon Wigner time delay.

In the case of argon, the situation is different, as initially discussed by Guénot *et al.* [57, 94]. Indeed, for $m = 0$, the final p state can be reached via the intermediate s and d states with respective scattering phases η_0 and η_2. These two paths interfere, resulting in an effective phase which corresponds to neither of the two scattering phases. This means that the RABBIT signals associated to the two final states, S_{10} and S_{30}, do not oscillate with the same phase. This leads to a total sideband signal oscillating at the same frequency, 2ω, but with a different phase and a reduced contrast. For this reason, the phase of the total sideband signal cannot be related to the Wigner time delays of either of the intermediate states. Nonetheless, from Fano's propensity rule, we know that some transitions are more probable than others.

In Ne and Ar, the one-photon $p \to d$ channel tends to dominate over the $p \to s$ channel, particularly at low kinetic energy. In addition, the $p \to d$ channel is available for all magnetic quantum numbers of the electron in the ground state while the $p \to s$ channel is only possible for $m = 0$. As a result, it is often (but not always) possible to neglect the channel with

lowest angular momentum so that we can extract an approximate Wigner time delay of the intermediate state with highest angular momentum from the measurement.

3 Experimental measurements

Experimentally, it is impossible to directly access the Wigner time delay from a single measurement, even in the ideal case of a single channel. The first reason is that one would have to disentangle the contribution of τ_W from that of τ_{XUV} and τ_{cc}. While the continuum-continuum delay, τ_{cc}, can be calculated theoretically and subtracted from the data, the attochirp is very difficult to estimate theoretically since it is highly dependent on the generation conditions which, in general, cannot be estimated accurately enough. The second reason is that it would require knowing with a very high degree of accuracy the exact delay τ between the APT and the IR pulse, which is not possible experimentally.

In order to avoid this problem, one can measure two different photoionization processes in identical conditions such that the difference is independent of τ_{XUV} and τ. This can be done by ionizing different subshells of the atom or molecule (for example $3s$ and $3p$ shells of Ar) or by comparing different final states of the ion (for example $3p^5(^2P_{1/2})$ and $3p^5(^2P_{3/2})$ in Ar^+). Both methods result in photoelectrons with different kinetic energies which can be disentangled if the energy shift is large enough. This "double RABBIT" method was used in papers I, VII, VIII, X. It is also possible, if the experimental setup is very stable, to perform two consecutive RABBIT measurements on different gases and look at the difference between the two measured phases [94]. This was done in paper X.

3.1 Photoionization time delays in neon

Neon is the first atom from which photoionization time delays were measured by Schutlze and co-workers in 2010 [22]. Instead of using the RABBIT technique the authors used the attosecond steaking technique [95]. Like RABBIT, the streaking technique can be used to measure both amplitude and phase of the photoelectron wavepackets. There are however a number of differences as extensively discussed in Ref. [96]. First, while RABBIT uses a train of attosecond pulses, the streaking technique uses an isolated attosecond pulse to generate an EWP at a well defined moment in time. Contrary to the the spectrum of attosecond pulse trains, the spectrum of isolated attosecond pulses is continuous and a few eV broad. The second difference is that the streaking technique uses an intense close-to-single-cycle IR pulse while, in the RABBIT method, weaker and longer IR pulses are used. In streaking, the strong vector potential of the IR field streaks the electron wavepacket generated by the attosecond pulse, resulting in a delay-dependent energy shift of the EWP. By ionizing and streaking simultaneously electrons from the $2s$ and $2p$ shells of neon, Schultze *et al.* could

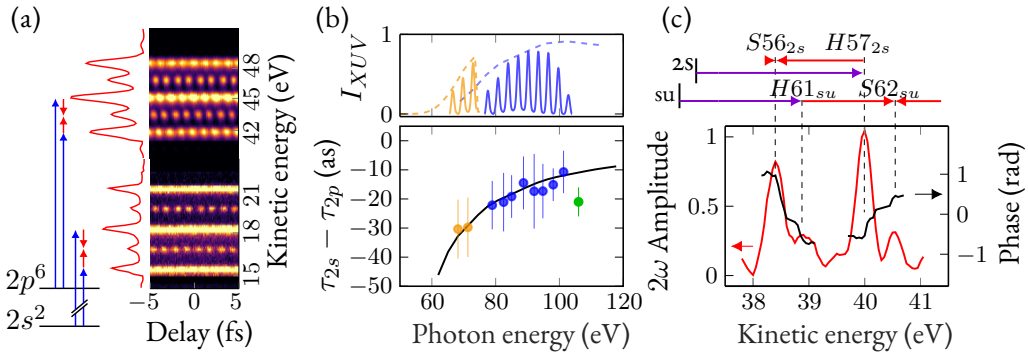

Figure 4.2: (a) Schematic representation of the double RABBIT measurement for photoelectrons from the $2s$ and $2p$ shells of neon. (b) Atomic time delay difference between $2s$ and $2p$ measured with different XUV spectra using AlZr (orange) or Zr (blue) filters. The green point is the measurement by Schultze *et al.* [22]. The solid black curve is the theoretical prediction. (c) Energy scheme and 2ω amplitude showing the partial overlap of shake-up harmonics with $3s$ sidebands. The black curve shows the phase measured with Rainbow RABBIT. Figure adapted from paper I.

retrieve a difference in atomic delay $\tau_{2s} - \tau_{2p} = -21 \pm 5$ as [22][3]. This delay was larger than that predicted by theory, thereby triggering an important theoretical activity in order to understand this measurement. Seven years later, there was still no explanation for this discrepancy.

In paper I, we investigate the difference in photoionization time delays in Ne between the $2s$ ($I_p = 48.5$ eV) and $2p$ ($I_p = 21.6$ eV) shells. A first set of experiments is performed using a combination of Al and Zr filters to select only three harmonics with photon energies between 65 and 70 eV. The photon energy is high enough to ionize electrons from both $2s$ and $2p$ sub-shells [Fig. 4.2(a)]. Comparing the phase of corresponding sideband orders, we extract a difference in atomic delay $\tau_{2s} - \tau_{2p} \approx -30$ as, which is in good agreement with the calculations based on many-body perturbation theory as can be seen in Fig. 4.2(b). Since these points are at lower photon energy than the measurements by Schultze *et al.*, we perform additional measurements at higher photon energy using a double zirconium filter [transmission curve in Fig. 4.2(b), blue curve]. At these photon energies, a large number of shake-up ionization channels open [97, 98]. Shake-up is a process in which after absorption of the XUV photon, the photoelectron transfers part of its energy to a second electron, promoting it to a higher bound state. As a result, the ion is left in an excited state and the photoelectron has a lower kinetic energy compared to direct photoionization. Most shake-up channels have a low cross section and hence can be neglected, however, the shake-up to the $2p^4(^1D)3p(^2P)$ state ($I_p = 55.8$ eV), has a cross section of the order of one sixth of the $2s$ photoionization

[3] In streaking, the IR also adds an additional delay, called Coulomb-laser coupling τ_{CLC}. It has been shown that although obtained differently, τ_{CLC} and τ_{cc} are identical.

cross section. Since the difference in ionization potential between the two processes is close, around $4.7\hbar\omega$, the one-photon ionization peaks (which we refer to as harmonic peaks) from the shake-up partially overlap with the sideband peaks from the $2s$ shell [Fig. 4.2(c)]. As can be seen in Fig. 4.2(c), the phase measured across the sideband varies strongly with energy. Using only the phase on the low energy part of the sidebands, where the amplitude of the shake-up harmonic peak falls to zero, we can reliably extract the phase of the $2s$ sideband and calculate the photoionization time delay between the $2s$ and $2p$ shells. Our measurements are in excellent agreement with the theoretical predictions. The result from Schultze *et al.* can probably be explained by the fact that the large bandwidth of the attosecond pulses prevented them from resolving the shake-up peaks which perturbed their measurement.

Our results show the potential of combining APTs with the RABBIT technique to measure photoionization time delays with a few tens of attosecond precision while maintaining sub-eV resolution. While, at first sight, this might seem to violate Heisenberg's uncertainty principle, it is not not case. Heisenberg's principle concerns the standard deviation of the probability distributions. The more precisely we determine the energy of the electron, the broader the probability distribution gets in the time domain. For example, as already discussed in chapter 2, the duration of a given harmonic is several femtoseconds long. The photoionization time delays that we measure correspond to group delay difference between two EWPs which can be arbitrarily long. In our measurements, the energy resolution is limited by the spectral resolution of the detector while the accuracy with which we can determine time delay differences mostly depends on the stability of the interferometer, not on the duration of the light pulses.

3.2 Photoionization time delays in argon

As mentioned earlier, photoionization time delays are a sensitive probe of electron correlations. Photoionization from the $3s$ ($I_p = 29.24$ eV) and $3p$ ($I_p = 15.76$ eV) shells of argon is known to exhibit signatures from intra-orbital [99] and inter-orbital correlations [86, 88]. One prominent example is the photoionization time delays associated to the $3s$ and $3p$ Cooper minima (CM). The $3p$ Cooper minimum results from the fact that the radial wave function changes sign, thereby crossing zero and leading to a cancellation of the photoionization cross section for the $p \rightarrow d$ channel [60], and to a large delay variation [86]. In this case, the $p \rightarrow s$ channel is dominant, resulting a break down of Fano's propensity rule for a bound to continuum transitions. Due to the competition between the two channels, in which only the $p \rightarrow d$ has a CM, in angle-integrated measurements, the delay variation in the vicinity of the $3p$ CM is rather small.

The $3s$ CM, originates from electronic correlations coupling the $3s$ and $3p$ shells. In this case, since there is only one channel ($s \rightarrow p$), the angle-integrated time delay is expected to strongly vary with energy although the sign, magnitude and position of the delay variation

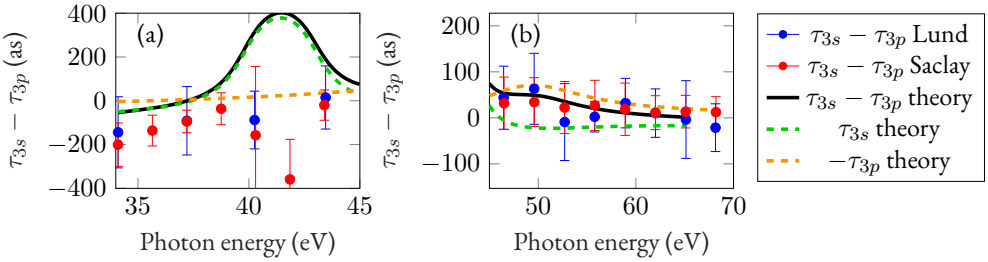

Figure 4.3: Atomic photoionization time delay difference between electrons from the $3s$ and $3p$ shells of argon in the region of the $3s$ Cooper minimum (a) and $3p$ Cooper minimum (b). Both Lund (blue) and Saclay (red) measurements are shown. Figure adapted from paper IX.

depends on the degree to which electron correlations are accounted for in the calculations [86].

Photoionization time delays in Ar have been investigated experimentally in several articles in the energy region between 30 and 40 eV [9, 57, 94], where different measurements and theories are in good agreement. These measurements end at the edge of the $3s$ CM. In paper VIII, we investigate the photoionization time delays in Ar over a broad energy range spanning from 35 to 70 eV and covering both $3s$ and $3p$ Cooper minima. As in the case of neon, several shake-up channels open at energies above 37 eV, in particular the $3s^2 3p^4(^1D)3d(^2S)$ ($I_p = 38.6$ eV) and the $3s^2 3p^4(^1D)4p(^2P)$ ($I_p = 37.1$ eV), refered to as $3p^{-2}3d$ and $3p^{-2}4p$ shake-ups respectively. Compared to the measurements in neon, there is a number of additional challenges. First, in the region of the CM, the photoionization cross section is very small. Second, because the $3s$ and $3p$ shells are closer in energy, the low energy part of the $3p$ PES and the high energy part of the $3s$ PES lie in the same energy region. The difference in ionization potential, $\Delta I_p = 9\hbar\omega - 0.47$ eV, is such that harmonics from $3p$ and the sidebands from $3s$ partially overlap. This makes it particularly difficult to measure the phase in the $3s$ sidebands in the region of the $3s$ CM where the sidebands are very weak and strongly contaminated by the large $3p$ harmonics. Finally, the photoelectrons originating from the two shake-ups also overlap with the $3s$ sidebands. While we could not directly observe these shake-up peaks, it is known from previous measurements and calculations that, in the energy region of the $3s$ CM, the cross section of $3p^{-2}3d$ and $3p^{-2}4p$ shake-up processes is higher than that of the $3s$ [100]. Figure 4.3 shows our measurements of the difference in atomic delay $\tau_{3s} - \tau_{3p}$ together with two-photon random phase approximation with exchange (RPAE) calculations in the region of the $3s$ CM [4.3(a)] and $3p$ CM [4.3(b)]. We observe good agreement between theory and experiment in the region of the $3p$ CM. These results also agree with results obtained in recombination spectroscopy [101]. However, in the region of the $3s$ CM, where theory predicts a large positive time delay, we measure a negative time delay of the order of -100 as. Our colleagues from the CEA Saclay in France,

independently performed the same measurements with a completely different setup. Interestingly, the results from the two experiments agree very well with each other. We attribute the deviation of the experimental data from theoretical calculations to the complex interplay between the $3s$ and the shake-up ionization channels which result in harmonics and sidebands from different ionization processes overlapping and oscillating with different phases. In particular, we show in paper VIII that taking into account the incoherent superposition of the $3s$ sidebands peaks with the $3p^{-2}4p$ harmonic peaks, we can reproduce the delays obtained experimentally at low energy ($E < 40$ eV). These measurements demonstrate the need for continuously improving the spectral resolution of the RABBIT technique in order to investigate photoionization dynamics in more complex systems, where multiple channels lead to complex PES.

Chapter 5

Resonant photoionization

In the previous chapter, we have discussed the case where the atom is ionized and the electron can imediately move away from the ion. This is not always the case. In some energy regions, the electron can be temporarily trapped, resulting in longer photoionization dynamics. We can distinguish two different cases: trapping of the electron in a quasi-bound state of the atom or trapping of the electron in the vicinity of the ion due to a potential barrier. In the former case, the electron is promoted to an unstable excited state of the atom, whose energy is above the ionization threshold. This state interacts with the continuum and relaxes by autoionization, i.e. by emitting an electron in the continuum. This is called a Fano resonance (or autoionizing resonance) [102], and is schematically represented in Fig. 5.1(a). The $sp2^+$ doubly excited state in helium is an example of Fano resonance. In the second case, the atom or molecule is immediately ionized but the electron is temporarily trapped by a potential barrier originating from the shape of the ionic potential. The electron eventually tunnels through the barrier and escapes the ion[1]. This is called a shape resonance and is schematically represented in Fig. 5.1(b). An example of a shape resonance is the giant dipole resonance in xenon [103, 104].

In this chapter, we investigate photoionization dynamics in the vicinity of Fano resonances and shape resonances. In the first case, it is not meaningful to talk about photoionization time delays because the fast spectral variation of the phase characteristic of Fano resonances induces a reshaping of the EWP during its propagation, hindering the possibility to define a one-photon Wigner delay [105, 106]. In papers II and IX, we focus instead on fully characterizing the autoionized EWP, similarly to what is done in ultrafast optics to characterize optical pulses. In the case of shape resonances, because these structures are usually broader than the width of a single harmonic, one can still define a Wigner time delay. In this case, due

[1] Note that the photoionization time delays which will be discussed are *not* tunneling time delays. The latter are not directly accessible from RABBIT measurements.

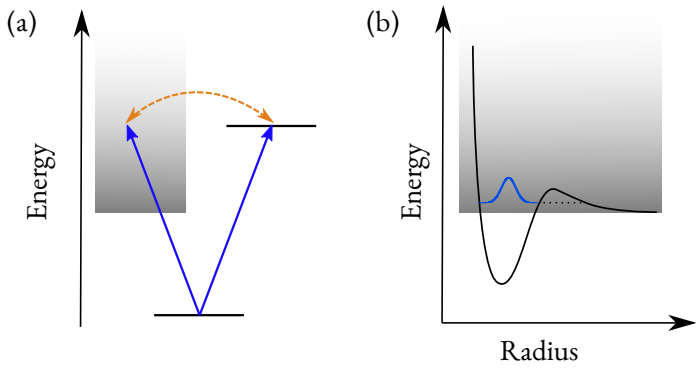

Figure 5.1: Resonances in the continuum. (a) Schematic representation of a Fano resonance, arising for the interaction of a bound state with the continuum. (b) Schematic representation of a shape resonance arising from the presence of the potential barrier through which the electron has to tunnel through to escape from the ion.

to the transient trapping of the electron close to the ion, interesting phenomena can occur. We study the photoionization via shape resonances in papers VII and X.

1 Fano resonances

Fano resonances are a general phenomenon in physics that occur whenever two oscillators, classical or quantum, are coupled via some interaction. In the context of photoionization, Fano resonances occur whenever a quasi-bound state is embedded in a continuum as shown in Fig. 5.1(a). These discrete states can be doubly excited states such as the $2snp$ states in helium, which are above the ionization potential ($I_p = 24.6$ eV), or inner-shell singly-excited states, such as the $3s^1 3p^6 np^1$ series in argon with an excitation energy higher than the ionization potential for the $3p$ shell ($I_p = 15.8$ eV). Electron correlations for these high-lying states are very important. As a result, the atomic state is not well described by independent configurations of electronic states. Instead, the different electron configurations, bound state or continuum state, mix so that the discrete state becomes unstable and quickly decays. The doubly excited states in He can be separated in two branches according to Cooper's classification [107]. The $|spn^+\rangle$ states can be easily accessed via optical transitions and mostly decay in the continuum, resulting in the autoionization of the atom. The $|spn^-\rangle$ cannot be accessed by optical transitions, which are quasi-forbidden, and decay via fluorescence [108]. The $3s^1 3p^6 np^1$ states in argon, or in short $3s^{-1} np$, also decay via autoionization. Table 5.1 summarizes the autoionizing resonances studied in this thesis and their characteristics.

Table 5.1: Energy E_α, Fano parameter q, spectral width Γ and lifetime τ of the autoionizing states studied in this thesis. Spectroscopic data from [109, 110].

Resonance	E_α (eV)	q	Γ (meV)	τ (fs)
He $sp2^+$	60.15	-2.77	36	17
He $sp3^+$	63.66	-2.58	8	82
Ar $3s^{-1}4p$	26.61	-0.25	76	9

1.1 Fano's formalism

The name Fano resonance comes from the Italian physicist, Ugo Fano, who developed the formalism explaining this phenomenon [102]. In this section, we introduce Fano's formalism. We consider a discrete state $|\alpha\rangle$ and a continuum of non degenerate states $|\beta_E\rangle$, E denoting their energy. Both discrete and continuum states are eigenstates of the unperturbed Hamiltonian $\hat{H}_0$. Due to configuration interaction, the state $|\alpha\rangle$ is coupled to the continuum via an interaction term $\hat{V}$. As a result, the total Hamiltonian $\hat{H} = \hat{H}_0 + \hat{V}$ is such that

$$\begin{aligned} \langle\alpha|\hat{H}|\alpha\rangle &= E_\alpha, \\ \langle\beta_E|\hat{H}|\alpha\rangle &= V_E, \\ \langle\beta_E|\hat{H}|\beta_{E'}\rangle &= E\delta(E-E'), \end{aligned} \tag{5.1}$$

with $\delta(E)$ the Dirac delta function. We then diagonalize the Hamiltonian in order to obtain its eigenstates. The eigenstates take the form of the superposition of bound and continuum states:

$$|\psi_E\rangle = a\,|\alpha\rangle + \int b'_E\,|\beta'_E\rangle\,\mathrm{d}E', \tag{5.2}$$

where the coefficients a and b'_E are given in Fano's article [102]. We can then calculate the one-photon transition matrix element from the ground state $|g\rangle$ to the final resonant continuum $|\psi_E\rangle$:

$$\langle\psi_E|\hat{z}|g\rangle = \langle\beta_E|\hat{z}|g\rangle\,\frac{q+\epsilon}{\epsilon+i}, \tag{5.3}$$

where $\epsilon = 2(E-E_\alpha)/\Gamma$ is the reduced energy, with $\Gamma = 2\pi|V_E|^2$ the width of the resonance. The q parameter is a real number measuring the relative strength between the transition from the ground state to the discrete state and the direct ionization to the continuum:

$$q = \frac{\langle\alpha|\hat{z}|g\rangle}{\pi V_E^*\,\langle\beta_E|\hat{z}|g\rangle}. \tag{5.4}$$

Equation 5.3, shows that the transition matrix element from the ground state $|g\rangle$ to the modified continuum $|\psi_E\rangle$ is the transition matrix element from the ground state to the unperturbed continuum $\langle\beta_E|\hat{z}|g\rangle$ multiplied a resonance factor

$$R(\epsilon) = \frac{q+\epsilon}{\epsilon+i}. \tag{5.5}$$

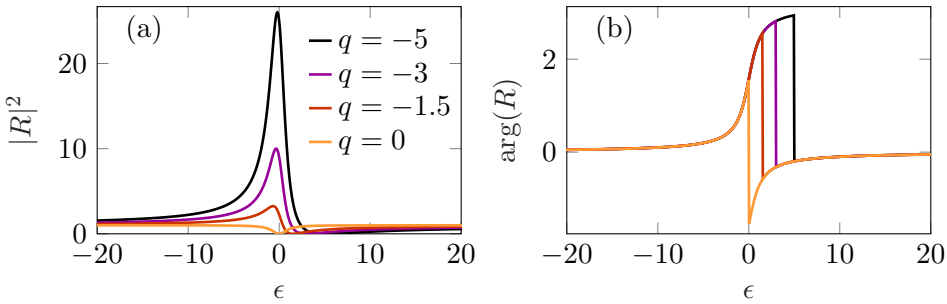

Figure 5.2: Square modulus (a) and phase (b) of the resonant factor R as a function of the reduced energy ϵ for different values of the q parameter. The legend in (a) is common to (a) and (b).

The modulus square of Eq. 5.3 gives the famous Fano profile

$$\sigma(E) = \sigma_0 \frac{(q+\epsilon)^2}{\epsilon^2+1}, \tag{5.6}$$

where σ_0 is the off-resonance photoionization cross-section.

Figure 5.2(a), shows the Fano profile for different values of q. The resonance profile is in general asymmetric, characterized by an enhancement of the photoionization cross-section followed by a minimum. This can be explained from the fact that two ionization paths lead to the continuum and interfere: direct ionization and photoexcitation of the quasi-bound state followed by autoionization to the continuum (see Fig. 5.1). This results in constructive and destructive interference yielding an asymmetric line-shape. The exact shape of the resonance profile depends on the q parameter. In the limit $q \to \pm\infty$, corresponding to the transition to the bound state being infinitely larger than the transition to the continuum, we recover a symmetric Lorentzian profile, typical of transitions between bound states. In the limit $q \to 0$, corresponding to the case where the transition to the continuum is infinitely stronger than that to the bound state, we obtain a window resonance. The destructive interference leads to a decrease of the photoionization cross section at resonance.

Traditional photoionization experiments only provide information on the cross section. However, in order to fully characterize these resonances, it is also necessary to measure their phase. The phase of the resonant factor is given by

$$\arg[R(\epsilon)] = \arctan\epsilon - \pi\Theta(\epsilon+q) + \frac{\pi}{2}, \tag{5.7}$$

where $\Theta(\epsilon)$ is the Heaviside function. The phase variation as function of the reduced energy is shown in Fig. 5.2(b). The phase increases smoothly from 0 and jumps by $-\pi$ at $\epsilon = -q$ before increasing again smoothly towards 0. The phase jump originates from the fact that the complex amplitude in Eq. 5.3 crosses zero.

In his original derivation, Fano also considers the case where a discrete state can interact with multiple continua. This is the case for the Fano resonances in argon, where the $3s^{-1}np$ discrete states decay in the s and d continua. In general, for any two non-degenerate continua $|\beta_{\xi E}\rangle$ and $|\beta_{\xi' E}\rangle$, the total Hamiltonian in Eq. 5.1 is modified such that

$$\begin{aligned}
\langle\alpha|\hat{H}|\alpha\rangle &= E_\alpha, \\
\langle\beta_{\xi E}|\hat{H}|\alpha\rangle &= V_{\xi E}, \\
\langle\beta_{\xi' E}|\hat{H}|\alpha\rangle &= V_{\xi' E}, \\
\langle\beta_{\xi E}|\hat{H}|\beta_{\xi E'}\rangle &= E\delta(E-E'), \\
\langle\beta_{\xi E}|\hat{H}|\beta_{\xi' E'}\rangle &= 0.
\end{aligned} \tag{5.8}$$

In this case, it is more convenient to transform the two interacting continua into an interacting continuum $|\beta_E^{(1)}\rangle$ and a non-interacting continuum $|\beta_E^{(2)}\rangle$ defined as [11, 102]

$$|\beta_E^{(1)}\rangle = \frac{V_{\xi E}}{V_E}|\beta_{\xi E}\rangle + \frac{V_{\xi' E}}{V_E}|\beta_{\xi' E}\rangle\,, \tag{5.9}$$

$$|\beta_E^{(2)}\rangle = \frac{V^*_{\xi' E}}{V_E}|\beta_{\xi E}\rangle - \frac{V^*_{\xi E}}{V_E}|\beta_{\xi' E}\rangle\,, \tag{5.10}$$

with $|V_E|^2 = |V_{\xi' E}|^2 + |V_{\xi E}|^2$. Both states can be radiatively coupled to the ground state but only $|\beta_E^{(1)}\rangle$ interacts with the bound state $|\alpha\rangle$. In analogy to the single continuum case (Eq. 5.3), the transition matrix elements to the final interacting $|\psi_E^{(1)}\rangle$ and non-interacting $|\psi_E^{(2)}\rangle$ continua are given by:

$$\langle\psi_E^{(1)}|\hat{z}|g\rangle = \langle\beta_E^{(1)}|\hat{z}|g\rangle\,\frac{q+\epsilon}{\epsilon+i};\ \langle\psi_E^{(2)}|\hat{z}|g\rangle = \langle\beta_E^{(2)}|\hat{z}|g\rangle\,. \tag{5.11}$$

The total photoionization cross section is given by the incoherent sum of the two channels:

$$\sigma(E) = \sigma^{(1)}\frac{(q+\epsilon)^2}{\epsilon^2+1} + \sigma^{(2)}. \tag{5.12}$$

It is not possible to give an expression for the total phase since the two channels add incoherently. However, the phase of the interacting channel takes the same form as Eq. 5.7, while that of the non interacting channel is flat on the energy scale of the resonance.

1.2 Two-photon finite pulse model for resonant photoionization

So far, we have limited our discussion to the case where a single XUV photon excites a resonances. Here, we extend the two-photon non-resonant finite pulse model for laser assisted-photoionization presented in chapter 3 to the case where the XUV pulse is resonant with an

autoionizing state. This is based on the work by Jiménez-Galán and co-workers [61, 62]. We further restrict the discussion to the case where there is only a single continuum and a single resonance in the intermediate state.

Let us first consider the two-photon transition matrix element. Jiménez-Galán and co-workers show that, for a given ionization channel going from the ground state $|g\rangle$ to a final non-resonant continuum $|\beta_E\rangle$, through an intermediate resonant continuum $|\psi_\varepsilon\rangle$ the two-photon transition matrix element takes a form similar to that of one-photon case (Eq. 5.3):

$$M^{(\pm)}_{\beta_E g} \propto \frac{\epsilon_{\varepsilon\alpha} + q^{(\pm)}_{eff}}{\epsilon_{\varepsilon\alpha} + i}, \tag{5.13}$$

where $q^{(\pm)}_{eff}$ is defined as:

$$q^{(\pm)}_{eff} = q \mp 2(q - i)\kappa\omega/\Gamma. \tag{5.14}$$

Since now two continuum energies, corresponding to the intermediate and final states, have to be considered, $\epsilon_{\varepsilon\alpha}$ indicates that this is the reduced energy difference between the bound state at energy E_α and the intermediate energy $\varepsilon = \hbar\Omega$. The parameter κ describes the strength of the coupling between the intermediate bound state and the final continuum. If $\kappa = 0$, $q_{eff} = q$ and we recover the same resonance factor as in equation 5.3. However, if $\kappa \neq 0$, q_{eff} becomes complex and depends on whether the IR photon is absorbed or emitted $(\pm)$. As a result, the phase variation is no longer given by Eq. 5.7. If $\kappa < 0$, in the case of emission, the phase variation becomes smoother than in the one-photon case and the amplitude of the phase jump is reduced. On the contrary, in the case of absorption, the total phase variation of the transition matrix element is 2π [11].

Figure 5.3 shows the modulus square and phase of the absorption and emission two-photon transition matrix elements for different values of the coupling parameter κ. For very small values of κ, $|M^{(\pm)}_{\beta_E g}|^2$ is almost identical for absorption and emission while the phases are very different. This is the case for example in helium where, for the $sp2^+$ doubly excited state $\kappa = -0.0003$ [62], as in the figure. For larger values of κ, we can observe a difference in both the amplitude and phase of the matrix element.

Let us now consider the time-dependent two-photon transition amplitudes given by equation 3.6. As a reminder, this assumes that both XUV and IR pulses are Fourier limited. Considering that the IR photon energy is much larger than the resonance width, the transition amplitude can be written as:

$$\mathcal{A}^{(\pm)}_{\beta_E g}(\tau) \approx \mathcal{F}(\tau) e^{\pm i\omega\tau} \left\{ w[z(E,\tau)] + (\kappa - \epsilon^{-1}_{E\alpha})(q - i) w[z(E_\alpha,\tau)] \right\}, \tag{5.15}$$

where, as in Eq. 3.6, $\mathcal{F}(\tau)$ and $z(E,\tau)$ are respectively, a form factor and a complex parameter defined in appendix 1 and $w(z)$ is the Faddeeva function. Note the different notation

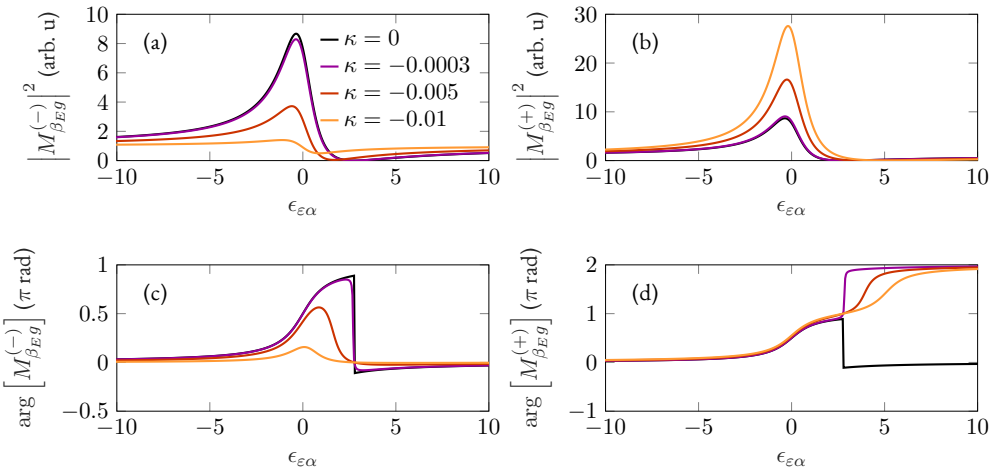

Figure 5.3: Resonant two-photon transition matrix elements in the case of emission (a,c) and absorption (b,d) of an IR photon. (a) and (b) show the modulus square of the matrix element for different values of the κ parameter. (c) and (d) show the phase of the matrix element. The legend in (a) is common for all the figures. The resonance parameters used are those for the $sp2^+$ state (see table 5.1).

for the reduced energy between Eqs. 5.13 and 5.13. Here $\epsilon_{E\alpha}$ is the reduced energy difference between the bound state $|\alpha\rangle$ and the *final* continuum $|\beta_E\rangle$ with energy $E = \hbar\Omega \pm \hbar\omega$, while in Eq. 5.13 $\epsilon_{\varepsilon\alpha}$ is the reduced energy difference between the bound state $|\alpha\rangle$ and the *intermediate* continuum with energy ε. Figure 5.4(a) shows the modulus square of the two-photon transition amplitude associated to the emission of an IR photon. The energy axis corresponds to the effective photon energy needed to reach the final state $|\beta_E\rangle$ in He. The spectrum shows a clear modulation as a function of the effective photon energy due to the Fano resonance in the intermediate state. Because in this case the IR is emitted, the signature of the Fano resonance is observed around the energy $E_\alpha - \hbar\omega \approx 58.6$ eV. The difference with Fig. 5.3(a), is that the transition amplitude depends both on the two-photon transition matrix elements and the spectral bandwidth of the XUV and IR fields. For this reason, far from $\hbar\Omega - \hbar\omega$, the spectral intensity falls to zero. The resonance is much narrower than the XUV bandwidth (180 meV), such that it modifies the intermediate continuum on an energy range smaller than the XUV bandwidth. This explains the presence of two peaks in the spectrum. The first large peak at low energy and the minimum at $E_f \approx 58.65$ eV, originate from the constructive and destructive interference characteristic of the Fano profile. The second, peak around 58.8 eV, originates from the excitation of a smooth continuum far enough from the resonance. Figure 5.4(a) shows that the exact shape of the spectrum depends on the bandwidth of the IR pulse. For narrow pulses ($\sigma_{IR} = 10$ nm), the constructive interference is very strong, resulting in a large narrow maximum, and the destructive interference leads to a complete cancellation of the photoionization probability. As the bandwidth of the IR in-

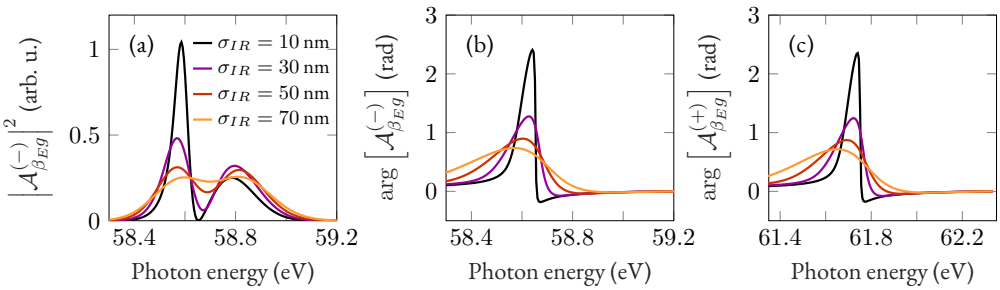

Figure 5.4: Resonant two-photon transition amplitudes for different pulse durations (FWHM). (a) Modulus square of the two-photon transition amplitudes corresponding to emission of an IR photon. (b,c) Phase of the two-photon transition amplitudes for emission (b) and absorption (c) of an IR photon. The legend in (a) is common for all the figures. The resonance parameters used are those for the $sp2^+$ state in He(see table 5.1) and $\kappa = -0.0003$. The pulse parameters used are $\hbar\omega = 1.55$ eV, $\hbar\Omega = E_\alpha + 0.14$, $\sigma_{XUV} = 180$ meV. The delay between XUV and IR is set to 0.

creases, the minimum becomes shallower and the low energy peak gets smaller and broader. This can be understood as a the result of frequency mixing due to the finite pulse effects (see section 1.2), which have an effect analogue to a convolution.

In Fig. 5.4(b) we show the corresponding phase of the two-photon transition amplitude $\mathcal{A}^{(-)}_{\beta_{Eg}}$. Compared to the phase shown in Fig.5.3(c), here the amplitude of the phase jump is smaller. As the spectral bandwidth of the IR pulse increases, the phase variation gets smoother and the total phase excursion decreases. In Fig. 5.4(c), we show the phase of $\mathcal{A}^{(+)}_{\beta_{Eg}}$. Interestingly, while Fig. 5.3(d) shows that the phase of the two-photon matrix element exhibits a 2π phase variation, here there is almost no difference between the phase of the absorption and emission transition amplitudes. Calculations show that the broadening and smoothing resulting from the finite pulse effects tend to hide the effect observed in Fig. 5.3(d). Because κ is very small for the $sp2^+$ resonance, to see a difference between absorption and emission would require using close to monochromatic IR pulses. In this case, the frequency mixing induced by an IR pulse with a 10 nm bandwidth is already large enough to wash out this effect. However, for resonances with a larger coupling parameter, such as the $3s^{-1}4p$ resonance in Ar ($\kappa = 0.05$), our calculations show that we should be able to measure a 2π phase variation in the emission sideband using an IR pulse with 10 nm bandwidth. For larger IR bandwidths, the transition amplitude recovers the typical smoothed Fano phase variation although we can still observe clear differences between absorption and emission transition amplitudes as we demonstrate experimentally in paper VIII.

1.3 Characterization of autoionized electron wavepackets

Experimentally, Fano resonances have been investigated for several decades. Since the first observations of Fano profiles in the photoionization cross section of rare gases by Madden and Codling [111], several high-resolution studies of the photoionization cross sections in the vicinity of autoionizing states have been performed using synchrotron radiation [109, 110, 112–116]. More recently, with the advent of attosecond science and technology, it has been possible to follow in time the exponential decay of autoionizing states [117, 118], to control the Fano profile [119], or to investigate the time evolution of two autoionizing states coherently excited [120].

Fano resonances in helium

One of the aims of this thesis is to fully characterize the electron wavepackets emitted via autoionizing states in both spectral and temporal domains. In paper II, we use the Rainbow RABBIT technique to measure the amplitude and phase of photoelectrons emitted via the $sp2^+$ and $sp3^+$ Fano resonances in He. This study follows the work of Gruson *et al.* who used the Rainbow RABBIT technique to measure the amplitude and phase of the $sp2^+$ Fano resonance and reconstruct the build up of the electron wavepacket in the continuum [13]. Our experiments aim at pushing forward the analysis of autoionization dynamics performed by Gruson and coworkers in order to obtain a complete picture of the ionization dynamics in the time-frequency domain. Importantly, the experimental conditions for the two experiments are very different, as summarized in table 5.2. In addition, to further increase the spectral resolution, we use a blind deconvolution algorithm based on the Lucy-Richardson method [77, 78].

Table 5.2: Comparison of the experimental parameters between this work and [13]: central wavelength, bandwidth and pulse duration of the IR, bandwidth of the harmonics, and spectrometer resolution (from left to right).

	λ_{IR}(nm)	σ_{IR}(meV)	Δt_{IR} (fs)	σ_{XUV}(meV)	σ_{MBES}(meV)
This work	800	125	30	180	89
[13]	1295	26	70	400	190

Figure 5.5 shows the principle of the experiment. By tuning the central frequency of the generating IR field, we can selectively excite the $sp2^+$ resonance with harmonic H39 or the $sp3^+$ resonance with harmonic H41. Neglecting for now the femtochirp of the harmonics, the phase of the non-resonant transition amplitude can be assumed to be flat, thereby providing a reference for the phase measurement of the resonant two-photon transition amplitude. We remind that the phase measured in the sidebands is defined as the phase difference between the emission and the absorption paths, $\Delta\varphi = \arg[\mathcal{A}^{(-)}] - \arg[\mathcal{A}^{(+)}]$. The sidebands

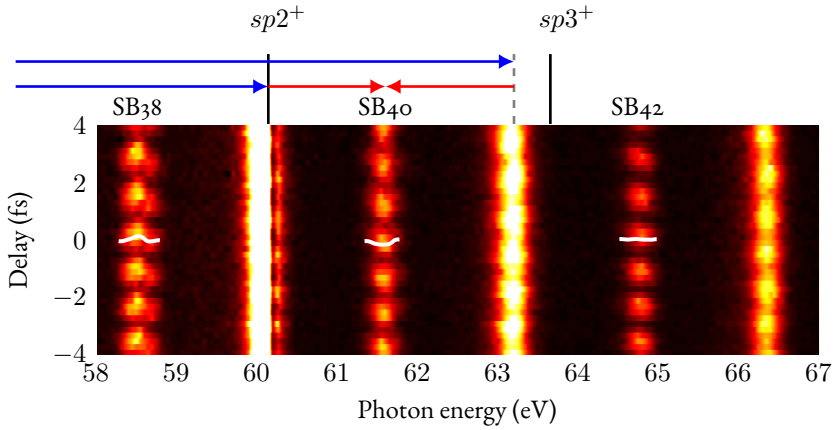

Figure 5.5: RABBIT scan when harmonic 39 is resonant with the $sp2^+$ state. The arrows on top indicate the XUV and IR transitions and the position of the two resonance is indicated with a black solid line. The phase of the Fano resonance is imprinted on the neighbouring sidebands as shown by the white lines. Figure adapted from paper II.

adjacent to the resonant harmonic, refered to as resonant sidebands, exhibit a phase variation characteristic of the Fano resonance (see white lines in Fig. 5.5). In the lower resonant sideband, the resonant transition amplitude corresponds to the emission path, while for the upper resonant sideband, the resonant transition amplitude corresponds to the absorption path. As a consequence, the sign of the phase measured in these two sidebands is opposite, the lower sideband providing the phase of the resonant transition amplitude with the right sign. If we now take into account the femtochirp, the phase of the non-resonant transition amplitude cannot be assumed to be flat. However, for high enough harmonic orders, the femtochirp of consecutive harmonics can be considered to be the same, thereby cancelling in the sideband[2].

Figure 5.6 shows the phases measured in sidebands SB38, SB40 and SB42 when H39 is resonant with the $sp2^+$ resonance (top row) and when H41 is resonant with the $sp3^+$ resonance (bottom row). For the $sp2^+$ resonance, we observe a total phase variation of about 1 rad in SB38 and SB40. The phase of SB42 is flat since both paths leading to this sideband are non-resonant. Despite very different experimental conditions, our results are very similar to those reported by Gruson and co-workers. In their work, the amplitude of the phase jump was limited by the spectral resolution of the MBES while in our work it is reduced due to the large bandwidth of the probe pulse (see table 5.2). The $sp3^+$ resonance is not accessible using standard Ti:Sapphire systems at 800 nm as shown in Fig. 5.6. However, thanks to the

[2]In reality, in the data analysis we do take into account that the combined effect of the femtochirp and a blueshift of the harmonics can result in a linear phase variation across the sideband as discussed in chapter 3 and in papers II and IV.

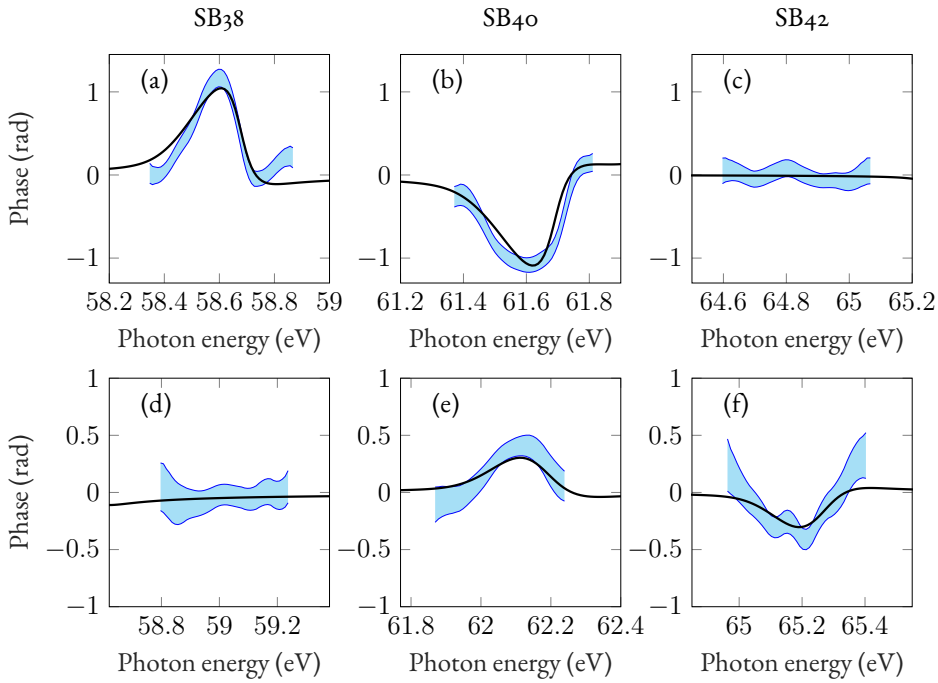

Figure 5.6: Phases measured (blue) in SB38, SB40 and SB42 in the cases where H39 is resonant with the sp2+ state (first row) and where H41 is resonant with the sp3+ state (second row). The shaded areas correspond to standard deviation around the measured value. The black solid line shows the result of the theoretical calculations using the finite pulse model. Figure from paper II.

tunability of our laser we are able to tune harmonic 41 on resonance in order to measure the phase variation induced by the $sp3^+$ resonance on the two neighbouring sidebands (SB40 and SB42). In this case, SB38 has a flat phase since we are detuned from the $sp2^+$ resonance. Because the $sp3^+$ resonance is much narrower than the $sp2^+$ one, the amplitude of the phase jump is greatly reduced due to the finite pulse effects.

In order to characterize the EWPs, we also need to measure their amplitude. For this, we need to extract the resonant 2-photon amplitude from the total sideband intensity. Assuming that the non resonant two-photon transitions are the same for all sidebands, we can extract the amplitude of the EWP emitted via the resonance, $|\mathcal{A}_R^{(\pm)}|$, as follows [13]

$$\left|\mathcal{A}_R^{(\pm)}\right| = \frac{\tilde{I}_R^{(\pm)}(2\omega)}{\sqrt{2\tilde{I}_{NR}(2\omega)}} \tag{5.16}$$

where $\tilde{I}_R^{(\pm)}(2\omega)$ is the amplitude of the 2ω peak in the Fourier transform of the resonant side-

band (for example SB38 or SB40 for the $sp2^+$ case) and $\tilde{I}_{NR}(2\omega)$ is that of a non-resonant sideband (SB42 for the $sp2^+$ case).

Figure 5.7(a) shows the measured amplitude and phase of $\mathcal{A}_R^{(-)}$ for the $sp2^+$ resonance. Similarly to what we do in chapter 2 to characterize the attosecond pulse trains in the time-frequency domain, in paper II, we use different time-frequency representations of the EWP in order to fully characterize the ionization dynamics. In Fig. 5.7(c), we show the Wigner distribution of the EWP. In order to interpret the result, we calculate analytically the Wigner distribution associated to the resonance factor $R(E)$. In the time domain, the resonance factor $\tilde{R}(t)$ can be written as the sum of a direct excitation to the continuum (direct photoionization) and an exponential decay to the continuum (autoionization) [121]:

$$\tilde{R}(t) = \delta(t) - i\frac{\Gamma}{2\hbar}(q-i)\exp\left[\left(-i\frac{E_\alpha}{\hbar}+\frac{\Gamma}{2\hbar}\right)t\right]. \tag{5.17}$$

The Wigner distribution of the coherent sum of these two terms results in three terms, $W(E,t) = W_D(E,t) + W_A(E,t) + 2\mathrm{Re}[W_{AD}(E,t)]$, each of them having a distinct time-frequency representation. The first term corresponds to the time-frequency representation of the direct ionization path, the second term corresponds to the time-frequency representation of the autoionization path and finally the last term corresponds to the time-frequency representation of the interference of these two paths. The exact analytical expression of these three terms and their derivation are given in appendix 2.

The spectrally broad and temporally short feature centred at $t = 0$ in figure 5.7(c) can be understood as the Wigner distribution of the direct ionization. Its Gaussian shape reflects that of the harmonic. The spectrally narrow feature centred at $E_\alpha - \hbar\omega = 58.6$ eV, which is almost 10 fs long, corresponds to the decay of the autoionizing state. Finally the negative feature in the center and the positive lobe around 58.9 eV correspond to the interference term. The Wigner distribution hence allows us to disentangle the ionization dynamics of the two ionization paths involved in a Fano resonance. However, we can notice that the decay of the autoionizing state is much shorter than that predicted based on the resonance width (17 fs). In addition as is clear in Fig. 5.7(a), the lack of spectral resolution of the measurements leads to incomplete destructive interference in the Fano profile and a rather small phase variation.

Rainbow RABBIT measurements can be improved by reducing the bandwidth of the probe pulse. In order to obtain measurements with a better spectral resolution, we perform new experiments (unpublished) using a 10 nm bandpass filter in the probe arm of the interferometer, reducing the finite pulse effects. In Fig. 5.7(b) we show the measured amplitude and phase of the EWP measured in sideband 38 after deconvolution of the spectra[3]. Compared to the result from Gruson *et al.* and the results reported in paper II, these measurements

[3] The effect of the deconvolution algorithm in the case of large IR bandwidth is very small. For narrow bandwidths, the spectrometer resolution is the main limiting factor such that the deconvolution improves a lot the amplitude of the phase jump and the minimum of the destructive interference.

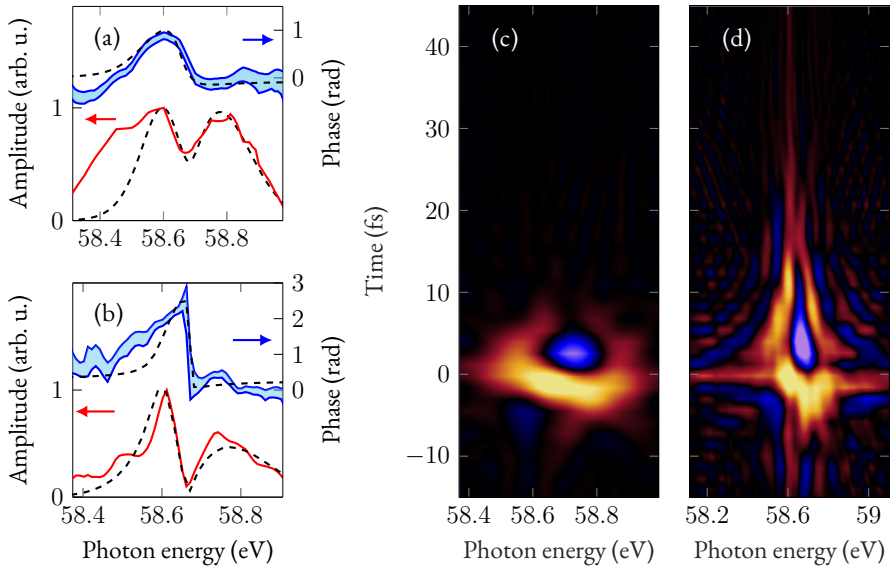

Figure 5.7: Characterization of autoionized wavepackets. (a) Amplitude (red) and phase (blue) of the 2-photon EWP measured with an IR bandwidth of 65 nm. (b) Same as (a) measured with an IR bandwidth of 10 nm. In both cases the dashed black curves show the theoretical calculations. (c) Wigner distribution of the EWP presented in (a). (d) Wigner distribution of the EWP presented in (b). Blue features correspond to a negative value, red/yellow features correspond to positive value and black corresponds to zero.

show almost complete destructive interference in the spectral amplitude and a phase jump close to π rad, demonstrating a large increase in spectral resolution. In Fig. 5.7(d) we show the Wigner distribution corresponding to this wavepacket. As previously, we can recognize the time-frequency distribution of the direct and autoionization paths. In this case, thanks to the much longer duration of the IR probe pulse, we can follow the decay up to approximately 40 fs. However, the largest difference between the two series of experiments is in the interference term of the Wigner distribution. First, it shows an extremely negative peak around $t = 5$ fs and $E = 58.7$ eV, second we can see hyperbolic interference fringes between the direct and autoionization paths. These fringes, which we had predicted theoretically in paper II, cannot be seen in Fig. 5.7(c) since they are very sensitive to the spectral resolution. This demonstrates the significant improvement in spectral resolution of our experiment and sets a new standard in terms of spectral and temporal resolution achievable in attosecond interferometry experiments.

The reconstruction of the Wigner distribution is based on the assumption that the EWPs are fully coherent. If they are not, the wavepackets cannot be described by a wavefunction and instead require a description in terms of a density matrix ρ. It has been shown that the lack of spectral resolution can result in a large decrease of the degree of coherence of the EWP [122].

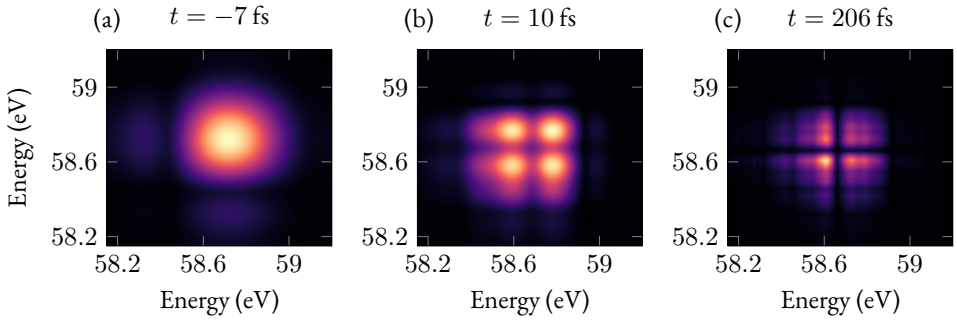

Figure 5.8: Snapshots of evolution the density matrix reconstructed from the experiment at $t = -7$ fs (a), $t = -10$ fs (b), $t = 206$ fs (c).

Here, the good agreement between our model, which assumes full coherence, and our experimental results justifies our method. In a system with time-reversal symmetry, the q parameter of a Fano resonance is real. However, if time-reversal symmetry is broken, for example due to decoherence, the q parameter becomes complex [123]. To quantify the degree of coherence, we modify our model to allow for a complex q parameter and a broader effective resonance width due to decoherence via a pure dephasing mechanism [123]. Based on this model, preliminary results show that the strength of the dephasing channel, i.e. the strength of the interaction with the environment, with respect to the electronic coupling between the bound and continuum states is around 1%. This indicates that to a good degree of approximation, we can consider that the helium atoms are a closed system and, most importantly, that we do not introduce an experimental source of decoherence. In the following, we assume that our state is fully coherent and additionally calculate the density matrix of the pure state EWP and its temporal evolution. For this, we need the time-dependent wavefunction

$$|\Psi\rangle\,(t) = \int_0^\infty c_E(t)\,|\psi_E\rangle\,\mathrm{d}E. \tag{5.18}$$

The complex amplitude that we measure experimentally $\mathcal{A}(E)$ simply corresponds to the asymptotic value of the coefficients $c_E(t)$ [124]: $\mathcal{A}(E) \propto \lim_{t\to\infty} c_E(t)$. It was rigorously demonstrated by Desrier and coworkers that, as long as the interaction between the bound state and the continuum, V_E, is independent of energy, the time-dependent coefficients can be accessed using the cumulative Fourier transform introduced in chapter 2 [124]:

$$c_E(t) = \frac{1}{2\pi}\int_{-\infty}^{\infty} \tilde{\mathcal{A}}(\tau)\Theta(t-\tau)\mathrm{d}\tau, \tag{5.19}$$

where $\tilde{\mathcal{A}}(\tau)$ is the Fourier transform of the measured complex amplitude. We can then construct the time-dependent density matrix, $\rho(t) = |\Psi(t)\rangle\,\langle\Psi(t)|$, based on our experimental results.

Figure 5.8 shows the result of the reconstruction of the density matrix based on our experimental results. The signal on the diagonal (from bottom left to top right) corresponds to the populations in the continuum, i.e. the probability to find an electron in a continuum state with given energy. The off-diagonal signal corresponds to the coherences, i.e. the degree of coherence between different states in the continuum. At early times, for which ionization is dominated by the direct path, the density matrix has a Gaussian shape reflecting the Gaussian spectrum of the XUV and IR pulses [Fig. 5.8(a)]. At later times, as the quasi-bound state decays in the continuum, the two paths interfere resulting in a decrease of the population around 58.7 eV. Fig. 5.8(b) shows that, at $t = 10$ fs, the populations in the resonant and non-resonant parts of the continuum have similar populations and have equally strong coherences. This strongly resembles to a Schrödinger cat's state $|\Psi\rangle = (|\varphi_1\rangle + |\varphi_2\rangle)/\sqrt{2}$, where the total wavefunction corresponds to the superposition of the two states with the same probability. At very long times, the populations converge towards the spectrum measured experimentally and the main features of the density matrix become sharper. The coherences between the resonant and non resonant parts of the EWP are at the origin of the interference pattern observed in the reconstructed Wigner distribution.

Finally we note that, while in this case the assumption of a pure state is justified, it might not always be the case. It is therefore of general interest to develop techniques that allow for a complete characterization of the density matrix of the EWP. Such techniques have already been proposed and demonstrated experimentally [70, 71], but so far, they have not been applied to gain new insight on photoionization dynamics.

Fano resonance in argon

In paper VIII, we study the photoionization via the $3s^{-1}4p$ resonance in Ar. In this case, the situation is much more complicated than for helium. Unlike the $sp2^+$ state, which can only decay in a p continuum, the $3s^{-1}4p$ state can decay in both s and d continua. In addition, in argon, the ion $(3p^5)$ is left with angular momentum $\ell_i = 1$ which couples to the final electron angular momentum $L = 1; 3$, leading to a total angular momentum given by $\Lambda = \ell_i + L = 0; 2$. As a result, three incoherent ionization channels are available: $(\Lambda = 0, L = 1)$, $(\Lambda = 2, L = 1)$ and $(\Lambda = 2, L = 3)$. Nonetheless, as discussed in paper VIII, calculations show that the two dominating channels, $(\Lambda = 0, L = 1)$ and $(\Lambda = 2, L = 3)$, have very similar Fano profiles and phases such that, in the following, we can, to a good degree of approximation, that there is only one effect channel with a well defined amplitude and phase.

A second complication arises from the fact that in argon, the spin angular momentum s of the Ar^+ ion and its orbital angular momentum ℓ_i couple to each other giving rise to two ionic states with total angular momentum $J = \ell_i + s = 1/2; 3/2$. The ionization energy needed to reach the $^2P_{3/2}$ state, $I_p(^2P_{3/2}) = 15.76$ eV, is lower than the energy needed to reach the

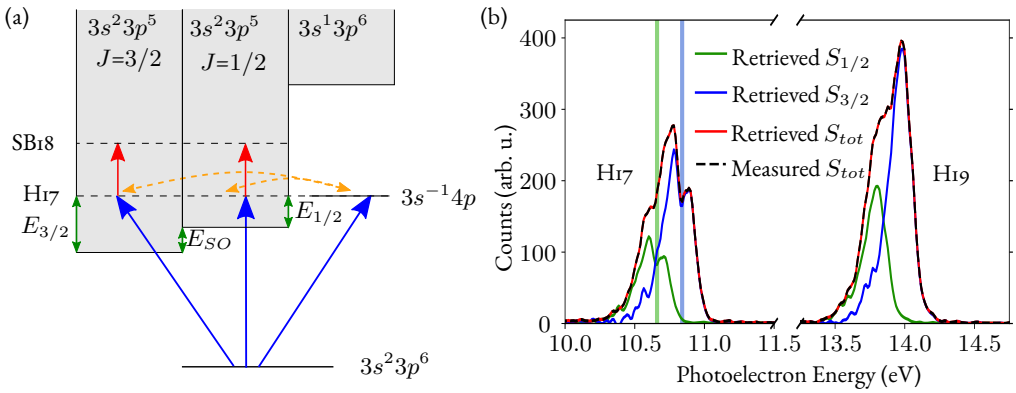

Figure 5.9: (a) Schematic representation of the energy levels and transitions involved in this work. The blue (red) arrows represent absorption of an XUV (IR) photon. The orange dashed arrows represent the configuration interaction between the quasi-bound state $3s^{-1}4p$ and the continua. (b) Retrieved (red line) and measured (black dashed line) XUV-only photoelectron spectra. The two S-O components $J = 1/2$ and $J = 3/2$ are shown in green and blue respectively. The blue and green lines show the position of the minimum in the PES due to the Fano resonance. Figure adapted from paper VIII.

$^2P_{1/2}$ state, $I_p(^2P_{1/2}) = 15.93$ eV. The difference in energy between the opening of these channels corresponds to the spin-orbit (S-O) splitting energy $E_{SO} = 180$ meV. The relevant energy levels and transitions considered in the following are presented in Fig.5.9(a). As a result of the S-O splitting, the total photoelectron spectrum can be written as the incoherent sum of two spectra corresponding to the two final states of the ion, $S_{1/2}$ and $S_{3/2}$:

$$S_{tot}(E) = S_{1/2}(E) + S_{3/2}(E). \tag{5.20}$$

Figure 5.9(b) shows the XUV-only PES in argon where harmonic 17 is resonant with the $3s^{-1}4p$ state while harmonic 19 is not resonant. The PES of H19 presents a double structure due to the overlap of Gaussian spectra spaced by the S-O splitting. The small value of E_{SO} in argon combined with the relatively broad bandwidth of the harmonics prevents us from fully resolving the two peaks. The triple structure observed on the PES of H17 can be attributed to the overlap of two complex spectra modified by the Fano resonance. When the IR is overlapped with the XUV, the total sideband signal also results from the overlap of sidebands associated to the $^2P_{3/2}$ and $^2P_{1/2}$ states of the ion. In order to measure the spectral amplitude and phase of the emitted EWPs it is necessary to disentangle to contribution from the two S-O split states.

In paper VIII we show that this can be done assuming that the PES associated to the two ionic states are identical, only shifted in energy by E_{SO} and scaled by a degeneracy factor. We can

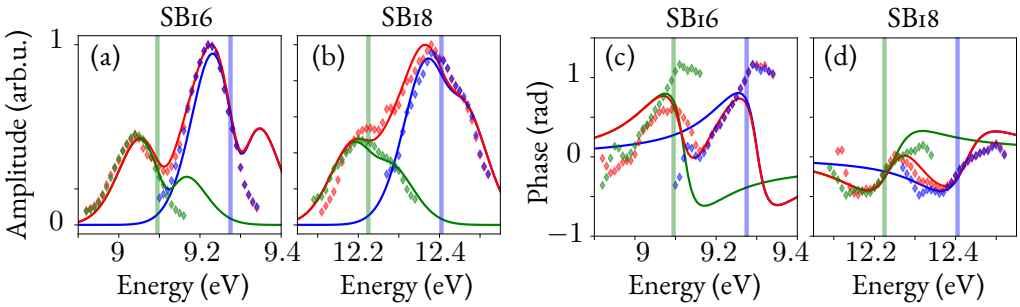

Figure 5.10: Separation of the amplitude (a),(b) and phase(c),(d) of the EWPs coming from the two ionic states. The total measured (diamonds) and simulated (solid curve) amplitude and phase is shown in red and the S-O separated ones are shown in green for $^2P_{1/2}$ and blue for $^2P_{3/2}$. The green and blue lines indicate the position of the resonance plus or minus one photon in photoelectron kinetic energy for the two S-O split states. Figure adapted from paper VIII.

then write the total spectrum in terms of a single function $S(E)$:

$$S_{tot}(E) = S(E) + 2S(E - E_{SO}), \tag{5.21}$$

where the factor 2 in the second term originates from the degeneracy ratio between the $^2P_{3/2}$ and $^2P_{1/2}$ states. Given this approximation, it is possible to numerically disentangle the contributions of the two ionic states by Fourier transform [125] as shown in Fig. 5.9(b). Performing this at every delay of the RABBIT scan, we obtain two RABBIT scans, one for each ionic state. Figure. 5.10 shows the amplitude and phase measured from the total RABBIT scan and those measured individually from the two S-O separated scans. This method therefore allows us to isolate the complex spectral amplitude of the 2-photon EWPs emitted via the $3s^{-1}4p$ resonance for a given S-O channel. These measurements are in good agreement with simple theoretical calculations in particular for SB18. The agreement is worse for SB16, possibly due to the presence of the broad $3s^{-1}4s$ resonance ($\Gamma = 170$ meV) in the vicinity of SB16 which is not included in the calculations and can be reached via two-photon transitions. Nonetheless, both experiment and theory show that, unlike helium, the amplitude and phase measured in the two sidebands are different. As discussed previously in section 1.2, this results from the coupling of the bound state with the final continuum, which is an order of magnitude stronger than for He.

2 Shape resonances

As mentioned at the beginning of the chapter, shape resonances in photoionization arise from the transient trapping of an outgoing electron due to the shape of the ionic potential. This means that, in contrast to Fano resonances, the ionic state does not change when

the electron is released in the continuum after tunneling through the barrier. In addition, in principle, shape resonances can arise even in the absence of electron correlations. However, because the position and width of the barrier strongly depend on the exact shape of the potential, an accurate description of these resonances requires accounting for correlation effects.

In this thesis, we study the photoionization via shape resonances in two systems. In paper VII, we investigate the photoionization via the $3\sigma_g^{-1}$ shape resonance in the N_2 molecule. In paper X, we measure photoionization time delays from the $4d$ shell in xenon in the vicinity of the giant dipole resonance.

2.1 Molecular shape resonance in nitrogen

Most of this thesis focuses on the study of photoionization dynamics in atoms, however, in paper VII we use the RABBIT technique to investigate the photoionization of N_2. Unlike atoms, molecules have more degrees of freedom which can play a role in photoionization. In particular, molecules can rotate and vibrate. Compared to the time scale of electronic dynamics, rotation of molecules is extremely slow and hence we can consider that the molecule does not rotate during photoionization. Molecular vibration is faster, in the picosecond to femotsecond time scale. However, it is still slow enough compared to electronic motion so that we can often consider that during an electronic transition, the nuclei stand still. In other words, we can consider that the transition dipole operator is independent of the internuclear distance. This approximation is known as the Franck-Condon approximation[4].

In paper VII, high-order harmonics are generated in argon to photoionize N_2 in the region of the $3\sigma_g$ shape resonance between 20 and 40 eV photon energy. With these photon energies, we ionize N_2 from both the $3\sigma_g$ and $1\pi_u$ subshells, leading to N_2^+ ions in the $X\ ^2\Sigma_g^+$ and $A\ ^2\Pi_u^+$ electronic states, referred to as X and A states respectively. Their potential energy curves are shown in Fig. 5.11(a). Each of these electronic states support several vibrational levels which can be excited during photoionization. Fig. 5.11(c) shows a photoelectron spectrum for XUV only in which we can distinguish photoelectron peaks with distinct shapes when the ion is left in the X or A state. For each of these broad peaks we can observe additional sub-peaks which originate from different vibrational states of the ion. Because the difference in energy between the X and A states is close to that of an IR photon, when the IR field is overlapped with the XUV, the sidebands from one electronic state overlap with the harmonics from the other state, similarly to the situations encountered in the non-resonant photoionization of Ne and Ar (see chapter 4). As a result, it is very difficult to identify the sidebands, as shown by the small difference between XUV-only and XUV+IR spectra in

[4]It should not be confused with the Born-Oppenheimer approximation which considers that, because the time scale for the evolution of the electronic and nuclear wavefunctions are very different, it is possible to decouple them.

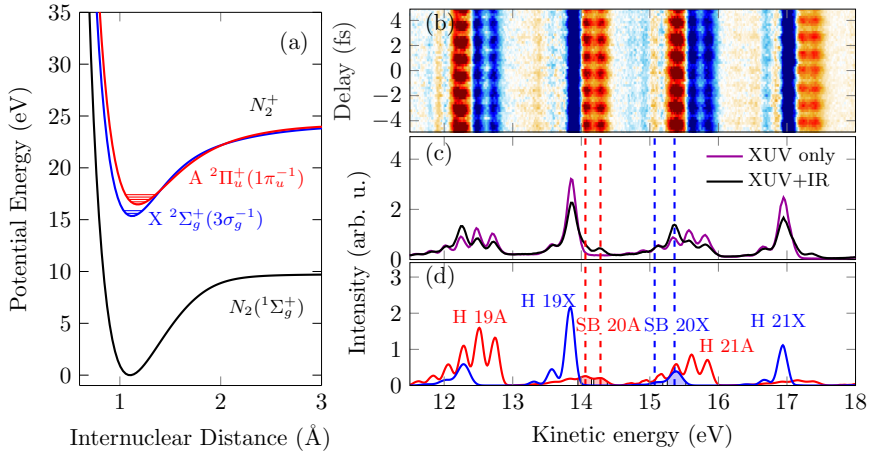

Figure 5.11: (a) Potential energy surfaces of the ground state of N_2 and of the two lowest states of the ion. (b) Difference between XUV+IR and XUV-only PES as a function of delay. (c) Delay averaged XUV-only and XUV+IR PES. Theoretical XUV+IR PES associated to the A state (red) and X state (blue). The dashed lines indicate the position of the sideband $v' = 0$ and $v' = 1$ for the X and A states. Figure adapted from paper VII.

Fig. 5.11(c). For this reason, we use a chopper in the probe arm which allows us to record every other shot an XUV only spectrum. Subtracting the XUV only PES from the XUV+IR PES, we obtain the RABBIT scan shown in Fig. 5.11(b), where a positive (red) signal indicates the presence of a sideband, while a negative (blue) signal is due to depletion of the harmonics. Theoretical calculations shown in Fig. 5.11(d), show that we can indeed attribute the positive peaks to the sidebands.

Figures 5.12(a)-(c) show the main experimental results where we present the measured time delay difference between the two electronic states and between different vibrational levels within the same electronic state. These results are compared to theoretical calculations which are in good agreement with the measurements, besides a constant energy shift[5]. The shape resonance is only observed in the X channel. Therefore, comparing the time delay between the X and A states, provides a measure of the molecular time delay associated to the shape resonance. Figure 5.12(a) shows that electrons from the X state are delayed up to 60 as compared to those from the A state as a result of the resonance. In Figs. 5.12(b) and (c), we show the time delay difference between vibrational levels $v' = 1$ and $v' = 0$ for the X and A states respectively. While for the X state we observe a large variation of the molecular time delay difference, for the A state the difference is constant and close to zero. These observations are an indication that, in the vicinity of the shape resonance, the Franck-Condon principle breaks down, as initially suggested by Dehmer *et al.* [126]. Indeed, theoretical calculations

[5]This energy shift originates from an incomplete description of electron correlations.

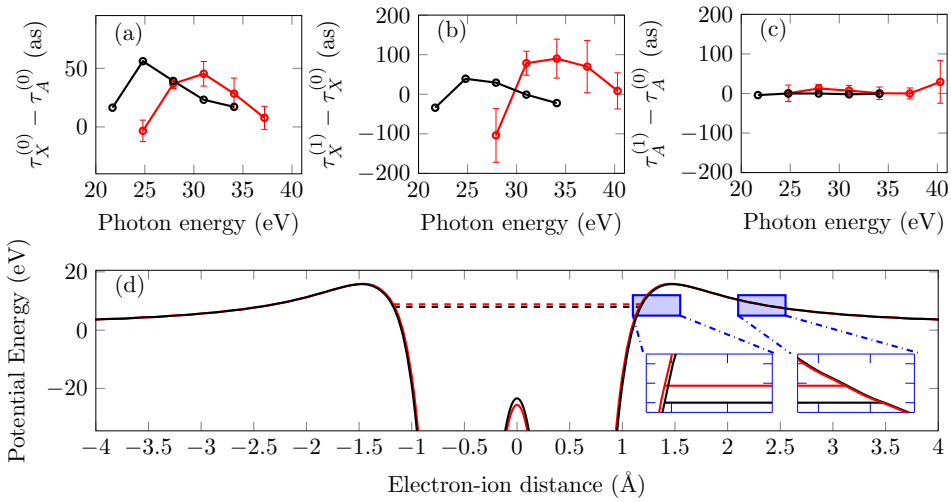

Figure 5.12: Time delay difference between the X and A states for $v' = 0$ (a), and between the $v' = 1$ and $v' = 0$ levels for the X (b) and A (c) states. The red curves are the experimental results and the black curves are theoretical calculations. (d) Potential felt by an electron escaping from the N_2^+ ion with internuclear distance $R(v' = 1) = 10.92$ pm (red) and $R(v' = 0) = 11.16$ pm (black). Figure adapted from paper VII.

show that the dipole transition matrix element for the X state depends on the internuclear distance, in contradiction with Franck-Condon's principle. As a result, the distributions of internuclear distances are slightly different for the two vibrational states. This difference, of only 2 pm between the maxima of the distributions, changes the width of the potential well, leading to a small shift of the resonance energy. As a result, the potential barrier seen by the electron is wider for $v' = 0$ than $v' = 1$, leading to a measurable time delay between the two electrons as seen in Fig. 5.12(b). These measurements constitute the first observation, in the time domain, of the effect of nuclear motion on the potential seen by the photoelectron.

2.2 Photoionization in the vicinity of the giant dipole resonance in xenon

In paper X, we study the photoionization of the $4d$ inner-shell of xenon with photon energies spanning 70-100 eV. This energy region is particularly interesting as photoionization is strongly affected by electron correlations in the vicinity of the giant dipole resonance, whose maximum is at 100 eV and spans several tens of eV [127]. This giant dipole resonance is characterized by a collective oscillation of all electrons from the $4d$ shell, leading to a large enhancement of the photoionization cross section. This collective effect originates from the presence of a shape resonance in the $4d \rightarrow \epsilon f$ channel [128]. In addition, xenon being a heavy atom, it is subject to strong relativistic effects, in particular close to the ionization threshold,

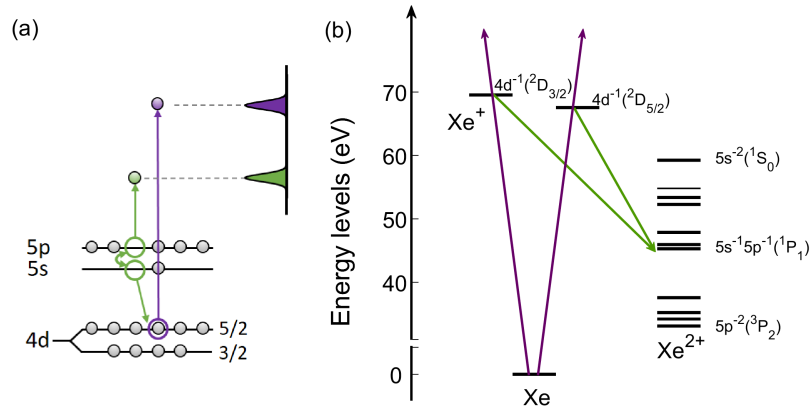

Figure 5.13: (a) Schematic representation of Auger decay. Absorption of an XUV photon leads to the emission of a photoelectron from the $4d$ shell (purple). The $4d^{-1}$ hole can then be filled by a valence shell electron, leading to the emission of a second electron (green). (b) Energy levels of the neutral, singly ionized and doubly ionized xenon atoms. Figure from paper x.

where the branching ratio between the two spin-orbit split ionic states ($^2D_{5/2}$ and $^2D_{3/2}$) varies as a function of kinetic energy [129]. Finally, following the photoionization from the $4d$ shell, electrons from the $5s$ and $5p$ shells can recombine with the $4d^{-1}$ hole and transfer the energy difference to another electron from one of these shells which is then ionized. This process is known as Auger decay and is schematically represented in Fig 5.13(a).

The combination of the spin-orbit splitting of the hole ($E_{SO} = 2$ eV) and the presence of various Auger decay channels [Fig. 5.13(b)], gives rise to a very complex photoelectron spectrum that makes the RABBIT analysis very difficult. In paper x, we use coincidence spectroscopy in order to reduce the spectral congestion. The principle of this technique is to detect both the photoelectron and the Auger electron, and associate them as coming from the same ionization event. This means that we need to keep track of all the electrons emitted at each laser shot. In standard conditions, the XUV flux and gas pressure are such that each APT leads to the ionization of several atoms. In these conditions, if two electrons are detected, it is impossible to know if they originate from the double ionization of a single atom or from the single ionization of two different atoms. Coincidence spectroscopy requires that the number of ionization events per shot is much smaller than one. For most of the laser shots we detect no electrons. When we detect two electrons they most probably come from the same event. In the following, the two electrons, which in general have different kinetic energies, are referred to as the fast electron, which we detect first, and the slow electron, which is detected later.

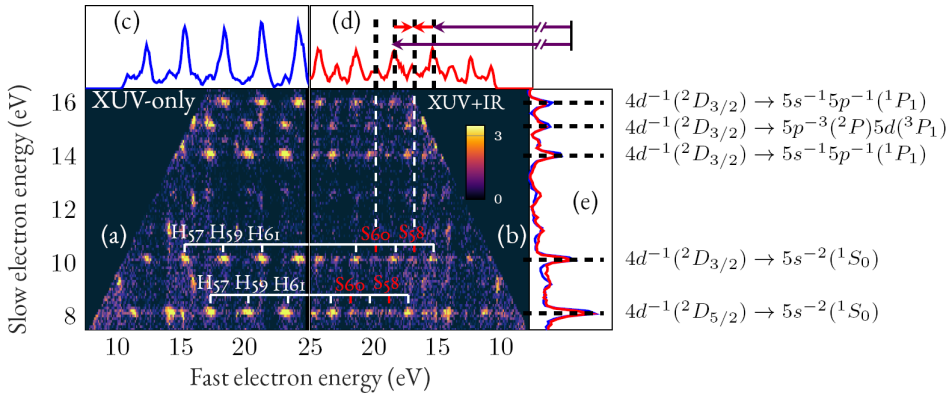

Figure 5.14: Coincidence map for XUV-only (a) and XUV+IR (b). The projections of the coincidence maps on the fast electron energy axis are show in (c) for XUV-only and (d) for XUV+IR. The projection on the slow energy axis shows the Auger peaks corresponding to different decay channels of the $4d^{-1}$ hole, with (red) and without (blue) IR field. Figure adapted from paper x.

Figure 5.14(a) shows an XUV-only coincidence map as a function of the kinetic energy of the slow and fast electrons. Because this map is symmetric with respect to the axis defined by $E_{fast} = E_{slow}$, the map is folded along this axis. The energy of electrons from Auger transitions is fixed by the energy difference between the respective energy levels of the electron and hole, and is therefore independent of the absorbed photon energy. On the contrary, the energy of the photoelectron depends on the energy of the XUV photon absorbed and the state of the intermediate Xe^+ ion. In addition, in the region of interest, the Auger electrons tend to be slower than the photoelectrons. As a result, the horizontal lines for a fixed slow electron energy that we see in Fig. 5.14(a), correspond to the energy of the photoelectron measured in coincidence with an electron coming a specific Auger transition. The projection of the map on the fast electron energy axis hence gives the spectrum of the photoelectrons as shown in Fig. 5.14(c). For example, the peaks labelled H57 correspond to the measurement in coincidence of the a photoelectron generated by absorption of harmonic 57 followed by the Auger decay $4d^{-1}(^2D_{3/2}) \rightarrow 5s^{-2}(^1S_0)$ or $4d^{-1}(^2D_{5/2}) \rightarrow 5s^{-2}(^1S_0)$. This technique allows us to disentangle contributions from the $^2D_{5/2}$ and $^2D_{3/2}$ spin-orbit split states of the Xe^+, since the Auger lines appear at different energies depending on the state of the $4d^{-1}$ hole[see Fig. 5.14(e)]. When the probe pulse is sent in the interaction volume and overlapped with the XUV, we observe sidebands between the XUV-only photoelectron peaks as shown in Figs. 5.14(b,d).

In figures 5.15 (a) and (b) we show the photoionization time delays associated to the $4d_{3/2}^{-1}$ and $4d_{5/2}^{-1}$ holes, using Ne $2p$ as a reference[6]. At energies above 80 eV, both figures show a

[6] As we show in paper 1, neon is a good reference since $2p$ shell has a time delay close to zero in this energy

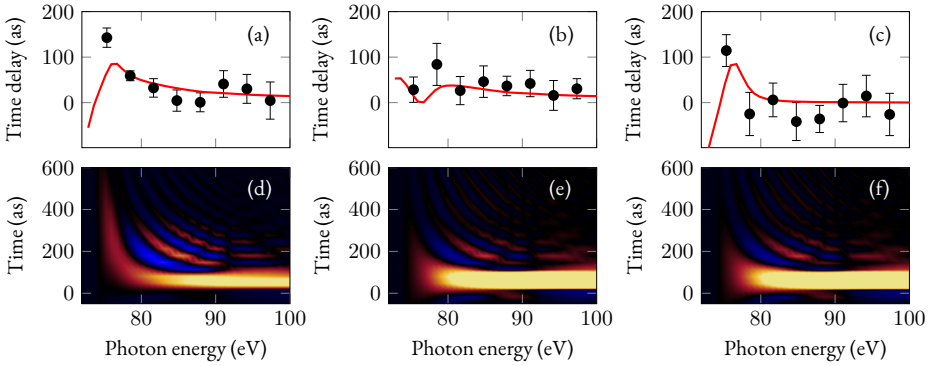

Figure 5.15: (a)–(c) Photoionization time delay differences $\tau_A[\mathrm{Xe}(4d_{3/2})] - \tau_A[\mathrm{Ne}(2p)]$ (a), $\tau_A[\mathrm{Xe}(4d_{5/2})] - \tau_A[\mathrm{Ne}(2p)]$ (b) and $\tau_A[\mathrm{Xe}(4d_{3/2})] - \tau_A[\mathrm{Xe}(4d_{5/2})]$ (c). Experimental points are in black and theory is in red. (d)–(f) Wigner distribution of the $4d_{5/2} \rightarrow \epsilon f_{5/2}$ (d), $4d_{5/2} \rightarrow \epsilon f_{7/2}$ (e) and $4d_{3/2} \rightarrow \epsilon f_{5/2}$ (f) channels. Figure adapted from paper x.

similar time delay decreasing from 40 as to 20 as for increasing photon energy. At low energy, $E < 80$ eV, the measured time delays depend on the state of Xe^+. In figure 5.15 (c), we show the time delay difference between the photoelectrons associated to the two spin-orbit split states of the $4d^{-1}$ hole. The difference is close to zero for almost all photon energies except at the lowest energy where we measure a delay difference of about 100 as. Our measurements are in very good agreement with theoretical calculations at high photon energy based on the relativistic random phase approximation (RRPA). At lower energy, the agreement between experiment and theory is only qualitative. It is very interesting to note that, around the giant dipole resonance, we do not measure a large delay variation. This can be explained from the fact that the resonance is very broad and the phase variation very slow. The variation of the time delay at low energy points towards interesting relativistic effects at threshold.

Photoionization from the $4d$ shell in the energy range studied here is dominated by $4d \rightarrow \epsilon f$ which is composed of three channels: $4d_{3/2} \rightarrow \epsilon f_{5/2}$, $4d_{5/2} \rightarrow \epsilon f_{7/2}$ and $4d_{5/2} \rightarrow \epsilon f_{5/2}$. The latter one, which involves a spin flip, is negligible at high photon energy, in the region of the giant dipole resonance, but contributes significantly close to threshold. In paper x, we show using RRPA calculations that the time delays associated to the three channels coincide above 80 eV, with a time delay around 40 as. This is in good agreement with the time delays measured experimentally at high energy. At low energy, the calculations show important channel-dependent oscillations of the time delays, indicating the presence of quantum interference between the different channels due to the spin-orbit interaction. This results in the large time delay measured experimentally at low energy.

region and can be accurately predicted by theory.

As in the case of Fano resonances, we use the Wigner representation to reveal the dynamics at the origin of this interference effect. Figures 5.15 (d)−(f) present the Wigner distribution of the one-photon transition matrix elements of the three ionization channels. This representation shows that there are at least two resonances in this energy region, a very broad and short lived one which corresponds to the giant dipole resonance and a narrow and long lived one around 75 eV. In the $4d_{3/2} \rightarrow \epsilon f_{5/2}$ and $4d_{5/2} \rightarrow \epsilon f_{7/2}$, the broad high energy resonance is dominant. However, for the $4d_{5/2} \rightarrow \epsilon f_{5/2}$ channel, both resonances have similar contributions, resulting in strong oscillations of the cross-term in the Wigner distribution. The observation of these two resonances is supported by calculations based on RRPA and analysed using multichannel quantum defect theory by Cheng and Johnson [129]. This analysis allows retrieving the eigenchannels, which are completely decoupled from each other, and which they label using the closest LS-coupled channels $(d^9 f)$ ^1P, ^3P and ^3D. The ^1P gives rise to the giant dipole resonance while the ^3P and ^3D result in two narrow resonances close to threshold. The latter resonances exist due to singlet to triplet mixing enabled by the spin-orbit interaction and are at the origin of the low energy long-lived feature observed in the Wigner representation.

The theoretical analysis allows us to conclude that the large time delay measured at low energy is a signature of the quantum interference between the dipole allowed $^1S \rightarrow ^1P$ transition and the spin-orbit induced $^1S \rightarrow ^3P, ^3D$ transitions, which have similar amplitudes in that energy region.

Chapter 6

Angle-resolved photoionization

Most studies of attosecond photoionization dynamics performed until now, including the results presented in chapters 4 and 5, have dealt with angle-integrated measurements. However, as discussed in chapter 4 angular integration results in the incoherent addition of contributions from ionization channels leading to different final angular momenta. As a result, in the analysis and interpretation of the results is it often necessary to neglect some of the channels. While in some cases these approximations are justified, in general, it is important to account for the different angular channels. This is one of the main limitations of angle-integrated measurements which only provide partial information on the ionization dynamics. Disentangling the contributions of the different angular channels requires a new method.

Angle-resolved RABBIT, first introduced in 2003 to characterize APTs [130], can, in principle, provide much more information on the interplay between different angular momentum channels in photoionization. In 2016, Heuser and coworkers used this technique to investigate angle-resolved photoionization time delays in He [12] and showed that despite the ground state of He being spherically symmetric, the photoionization time delays strongly vary as a function of the emission angle. Since then, the number of theoretical [131–133] and experimental [17, 19, 93, 134] angle-resolved studies has strongly increased.

In this chapter we present studies of angle-resolved photoionization dynamics performed during this thesis. We first introduce the angle-resolved RABBIT technique before presenting the results obtained in paper III, where two-photon angle-resolved photoionization time delays are measured in the vicinity of the $3s^{-1}4p$ resonance in Ar [1]. Finally, we discuss the results of paper V in which, by studying theoretically angle-resolved photoionzation, we set a work-frame to analyse and interpret angle-resolved RABBIT measurements, providing an

[1] While it is not possible to define a Wigner time delays for Fano resonances, it is possible to define a two-photon time delay in the vicinity of such resonances [106].

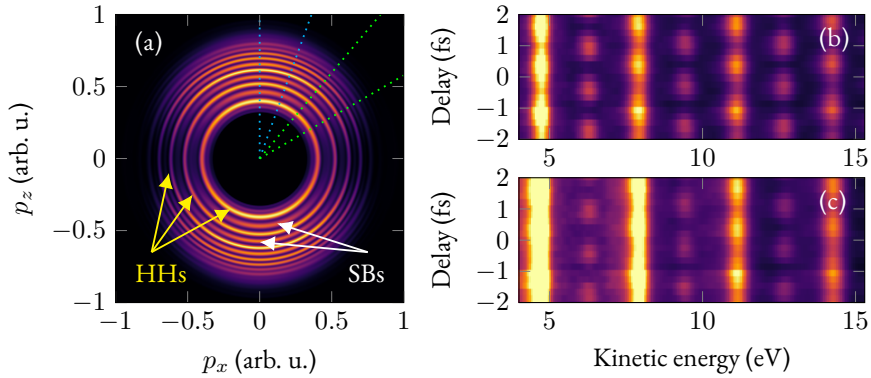

Figure 6.1: (a) Inverted VMI image for XUV+IR at a given delay. Harmonics (HHs) and sidebands (SBs) are indicated by yellow and white arrows respectively. Integrating the signal between 0 and 20 degrees (area defined by the blue dotted lines) and between 40 and 60 degrees (area defined by the green dotted lines,) with respect to the polarization axis $\hat{z}$, we obtain RABBIT scans presented in (b) and (c) respectively.

explanation to some experimental observations reported in paper III.

1 Angle-resolved RABBIT

In angle-resolved RABBIT, instead of measuring the total electron yield as a function of delay, we measure the photoelectron angular distribution (PAD) as a function delay. In figure 6.1(a) we present a typical momentum map at a given delay. As can be seen from the figure, harmonics and sidebands have different angular distributions. This can be understood from the fact that the angular distribution is determined by the spherical harmonics associated to the different final states. Since the angular momenta accessible by one- and two-photon transitions are different, the PADs of harmonics and sidebands are different.

In this thesis, the XUV and IR pulses used are linearly polarized, with parallel polarization axis. As a consequence, the PAD always has an azimuthal symmetry. In these conditions, as discussed in chapter 3, it is possible to parametrize the PAD according to equation

$$S(\theta) = \frac{\sigma_0}{4\pi}\left[1 + \sum_n^{\infty} \beta_n P_n(\cos\theta)\right] \tag{6.1}$$

where β_n are asymmetry parameters, P_n are Legendre polynomials, θ the angle with respect to the polarization axis $\hat{z}$ and σ_0 the angle-integrated photoionization cross-section. In the case where the parity of the final states is the same, the PAD is up-down symmetric such that odd asymmetry parameters are equal to zero in equation 6.1. Finally, it can be shown that for

an unpolarized target, regardless of the initial angular momentum of the electron, the highest order of the Legendre polynomials in the expansion 6.1, is given by $n_{max} = 2N$, where N is the number of photons exchanged [135]. As a result, the angular distributions for XUV-only and XUV±IR are respectively given by

$$\begin{aligned} S^{(1)}(\theta) &= \frac{\sigma_0^{(1)}}{4\pi}\left[1 + \beta_2^{(1)} P_2(\cos\theta)\right], \\ S^{(2)}(\theta) &= \frac{\sigma_0^{(2)}}{4\pi}\left[1 + \beta_2^{(2)} P_2(\cos\theta) + \beta_4^{(2)} P_4(\cos\theta)\right], \end{aligned} \tag{6.2}$$

where $S^{(1)}$ and $S^{(2)}$ are the PADs for the XUV-only and XUV±IR cases respectively, and $\sigma_0^{(1)}$, $\sigma_0^{(2)}$ their cross-sections. It is hence possible to fully describe the PADs of harmonics and sidebands with the β_2 and β_4 parameters.

When the delay between the XUV and IR is varied, the intensity of the sidebands oscillates. Looking at the harmonic and sideband signal as a function of delay at a given emission angle, we can reconstruct the RABBIT scan for electrons emitted in that direction. In practice, in order to have a reasonable signal to noise ratio, we need to integrate the signal over some angular interval. In Figs. 6.1(b) and (c) we present the RABBIT scans obtained after integration of the signal from 0 to 20 degrees (b) and from 40 to 60 degrees (c). It is then possible to extract the angle-dependent amplitude and phase of the emitted EWP.

The RABBIT equation for angle-resolved measurements can be written as:

$$S(\theta, \tau) = A(\theta) + B(\theta)\cos\left[2\omega\tau - \Delta\varphi_{XUV} - \Delta\varphi_A(\theta)\right], \tag{6.3}$$

where $A(\theta)$ and $B(\theta)$ are two coefficients whose exact form will be discussed in section 3. It is interesting to note that the XUV group delay is independent of the emission angle so that, for a given sideband order, the angle-dependence of the sideband phase corresponds directly to the angle-dependence of the atomic phase difference $\Delta\varphi_A(\theta)$. As discussed in chapter 3, the signal measured in a specific direction $\hat{k}$ corresponds to the interference of several partial waves. For this reason, it is not meaningful to write the atomic phase as the sum of a scattering phase and a continuum-continuum phase since these quantities are channel specific.

2 Angle-resolved study of a Fano resonance

In paper III, we use the angle-resolved RABBIT technique to investigate the photoionization via the $3s^{-1}4p$ resonance in Ar. This work is made in collaboration with the group of Ursula Keller at ETH, Zürich. Since the Lund and ETH results were obtained independently, in the following only the results from Lund are presented. Upon absorption of an XUV

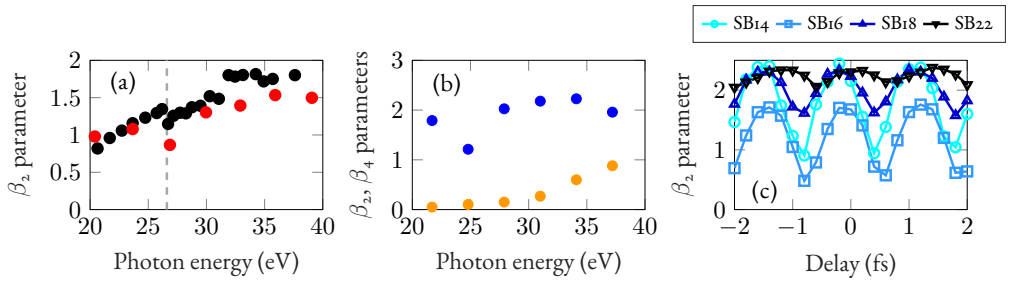

Figure 6.2: Asymmetry parameters. (a) XUV-only asymmetry parameters measured for harmonics 13 to 25 (red dots). Harmonic 17 is resonant with the $3s^{-1}4p$ resonance indicated by the gray dashed line. The measurements are compared to synchrotron radiation measurements from [136] (black dots). (b) Delay-integrated asymmetry parameters β_2 (blue) and β_4 (orange) for sidebands 14 to 24. (c) Asymmetry parameter β_2 as a function of the delay between the XUV and IR pulses. Figure adapted from paper III.

photon, an electron from the $3p$ shell of argon can be excited either to the ϵs or ϵd continua. Following Fano's propensity rule for one photon ionization, the channel $3p \rightarrow \epsilon d$ is usually stronger than that leading to ϵs. However, in the vicinity of a Fano resonance the transition amplitudes to the different final states change strongly, resulting in a modification of the PAD [115, 136]. Figure 6.2(a) shows the β_2 parameters measured for the different harmonics when harmonic 17 is resonant with the $3s^{-1}4p$ resonance ($E_\alpha = 26.61$ eV). The effect of the resonance is visible on H17 as a decrease of the β_2 parameters, reflecting the fact that, on resonance, ionization via the ϵs is dominant [137]. This is in qualitative agreement with experimental data from synchrotron measurements [115, 136]. Figure 6.2(b) shows the β_2 and β_4 parameters of the sidebands when the XUV and IR fields are overlapped. The effect of the resonance is very visible on sideband 16 (≈ 25 eV) as a large drop of the β_2 parameter. However, we do not see a clear signature of the resonance on β_4. The value the β_2 parameter in SB16 may also be affected by the presence of the $3s^{-1}4s$ resonance in its vicinity. When we change the delay between the XUV and IR pulses, we observe that the PADs of the harmonics and sidebands change periodically, resulting in an oscillation of the asymmetry parameters [see Fig. 6.2(c)]. The oscillations are not sinusoidal and their amplitude decreases with increasing sideband order. The fact that sidebands 16 and 18 have resonant contributions does not seem to affect these oscillations besides the fact that the values of the β_2 parameter for SB16 are in general lower than those of the other sidebands, in agreement with the observation from Fig. 6.2(b). As pointed out in paper III, such a delay dependence of the PAD must originate from an asymmetry between absorption and emission processes although, in paper III, no clear explanation for this effect is given.

In figure 6.3(a), we present the atomic delay for sideband 14, which has no resonant contribution. The measured delay has a strong dependence on the emission angle, dropping to almost -300 attoseconds at 75°. This result is similar to that observed in helium by Heuser

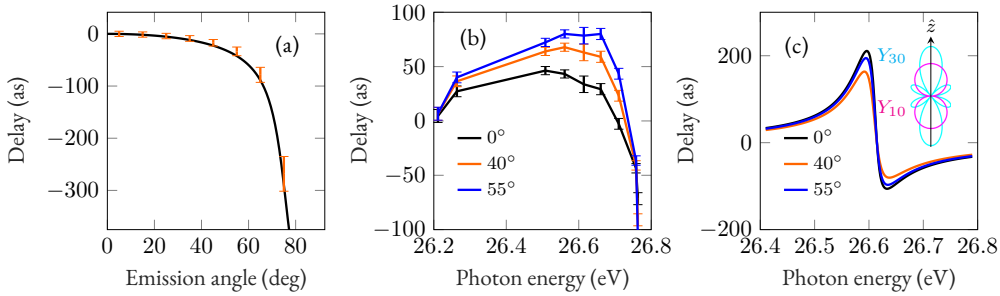

Figure 6.3: Angle-resolved atomic delays. (a) measured (orange) and theoretical atomic delays of SB14 as a function of the emission angle. (b) Measured phase of sideband 16 as function of the H17 central photon energy for three different emission angles. (c) Simulated delay variation across the the Fano resonance as a function of the XUV photon energy and for three different angles. The inset shows the spherical harmonics of the two final states considered in this simple model. Figure adapted from paper III.

and co-workers [12]. The main difference between He and Ar is that in argon the delay seems to decrease faster as a function of emission angle for similar electron kinetic energies. This result is in excellent agreement with theoretical calculations based on many-body perturbation theory.

In this study, we do not use the Rainbow RABBIT technique since it would require a very high number of counts in order to reliably extract the oscillation phase of sidebands at every energy and angle. Even integrating over 20 degrees, the signal is approximately 18 times lower than that of an angle-integrated measurement. In addition, the spectral resolution of the order of 200 meV in the energy range of the resonant sidebands limits the interest of this technique. To study the phase variation accross the resonance, we instead take advantage of the tunability of the laser to scan the central energy of the resonant harmonic across the resonance. For each wavelength, a RABBIT scan is acquired and the sideband phase is extracted, similarly to the work of Kotur and co-workers [11].

Figure 6.3(b) shows the time delays extracted from sideband 16 as a function of the central photon energy of H17 for three different emission angles. Each energy point corresponds to the phase extracted from one RABBIT scan. At the lowest energy point, where H17 is not resonant, we measure a delay variation similar to that measured in SB14. In the figure, this delay variation is removed by setting to zero the delay of the first energy point at each emission angle, in order to outline the delay anisotropy induced by the resonance. We can see a clear dependence of the delay on both emission angle and photon energy in the vicinity of the resonance. In the non-resonant case, we show in paper III that the angular dependence of the delay is independent of the photon energy (over the small energy region investigated). It is also interesting to note that around $E = 27.78$ eV, the curves for the different angles cross.

In order to qualitatively understand the origin of the complex angle and energy dependence of the delay, we use an extremely simple model. The model only aims at providing an intuitive picture of what is happening. First, we only consider $m = 0$ such that we only have two final states with angular dependence given by the spherical harmonics $Y_{30}(\theta)$ and $Y_{10}(\theta)$[2], which are represented as an inset in Fig. 6.3(c). Denoting the complex amplitude of the one-photon resonant channels as A_s and A_d, in paper III we approximate the angle dependent emission $(-)$ amplitude to sideband 16 as [3]

$$\mathcal{A}^{(-)}(\theta) = A_d Y_{30}(\theta) + (A_s + A_d) Y_{10}(\theta), \tag{6.4}$$

The final two-photon ϵp state has contributions from both intermediate resonant continua, while the ϵf continuum can only be accessed via εd. If taken individually, the final states have a well defined phase which is angle independent. In our measurements, the two final states mix with an angle dependent weight given by their respective spherical harmonics Y_{10} and Y_{30}. However, if we find an angle at which one channel cancels, it is possible to extract the delay of only one of the final states, which is impossible in angle-integrated measurements. For example, at $\theta = 55°$, Y_{30} has a node so that we can access the delay of the ϵp continuum. Unfortunately, the ϵp finals state can be accessed via both the εs and εd intermediate resonant continua. Consequently, it is not possible to separate the time delays associated to the two resonant channels. The delay variation calculated using the model in Eq. 6.4 is shown in Fig. 6.3(c) for three different emission angles. The simulations show that, like in our measurements, time delays depend both on the energy and emission angle. Furthermore, the angular dependence of the delays disappears at one photon energy, here equal to 26.6 eV. This can be understood by the fact that, at this energy, $A_d \approx 0$ [137], so that the same phase is measured regardless of the emission angle. We observe this point experimentally close to 26.8 eV. We emphasize that the simulations presented here and in paper III are the result of an extremely simple toy model which aims at discussing qualitatively the physics behind the energy and angle dependence of the measured time delays.

Finally, it is worth mentioning that, while we are able to qualitatively understand the measured delays, additional experiments and theoretical calculations should be carried out to get a better understanding of angle-resolved autoionization dynamics. Experimentally, although very challenging, it should be possible to perform angle-resolved Rainbow RABBIT measurements. In fact, we have performed promising experiments recently which we will mention in chapter 7. Theoretically, it requires a more complete model and a better understanding of angle-resolved RABBIT measurement in general. We discuss this in the following section.

[2] Here and in the following, $Y_{Lm}(\theta)$ denotes the θ-dependent part of the spherical harmonics $Y_{Lm}(\theta, \phi)$. These two quantities differ by the factor $e^{im\phi}$, which is integrated away in VMI measurements.

[3] This expression is slightly different from that in paper III due to a different definition of the channel resolved matrix elements in the partial wave expansion. In this thesis the phase $i^L e^{-i\eta_L}$ is included in our definition of channel-resolved matrix elements (Eq. 3.2). In paper III, this phase is not included in matrix elements and hence must be written explicitly. Both expressions are correct.

3 Theory of non-resonant angle-resolved RABBIT

Following the results obtained in paper III, we investigate more thoroughly the theory behind angle-resolved RABBIT measurements in the case of non-resonant photoionization. In particular we use the channel-resolved two-photon transition matrix elements discussed in the section on Fano's propensity rule in chapter 3.

For each accessible final state, in the monochromatic limit, the transition amplitude is given by

$$\mathcal{A}^{(\pm)}_{Lm}(\theta,\phi,\tau) = -\frac{ie^2}{\hbar} E_{XUV}(\Omega) E_{IR}(\omega) e^{\pm i\omega\tau} \sum_{\lambda} M^{(\pm)}_{\lambda Lm} Y_{Lm}(\theta,\phi), \tag{6.5}$$

where we add coherently the transition amplitudes of different angular channels leading to the same final state, such as $p \to s \to p$ and $p \to d \to p$ in the case of argon or neon for $m = 0$. As mentioned previously, each of these transition amplitudes has a well defined phase which is independent on the emission angle θ. Ideally, one would like to be able to access these quantities experimentally. In angle-integrated RABBIT, since the spherical harmonics form an orthogonal basis, the transition amplitudes to different final angular momenta add incoherently, giving rise to equation 4.7 in chapter 4. In angle-resolved RABBIT, for a given state of the ion, *i.e.* for a given magnetic quantum number m, all the accessible final states add coherently, while states with different m add incoherently. As a result, the angle- and delay-dependent sideband signal is given by

$$S(\theta,\tau) = \int_0^{2\pi} \mathrm{d}\phi \sum_m \left| \sum_L \mathcal{A}^{(+)}_{Lm}(\theta,\phi,\tau) + \mathcal{A}^{(-)}_{Lm}(\theta,\phi,\tau) \right|^2 . \tag{6.6}$$

This equation is completely general. We first restrict the discussion to the case of helium where $\lambda = 1$ and $m = 0$. In this case, the angle-resolved RABBIT signal takes the form

$$\begin{aligned} S(\theta,\tau) \propto \Big| & \overbrace{\left[M^{(+)}_{100} Y_{00}(\theta) + M^{(+)}_{120} Y_{20}(\theta) \right]}^{D^{(+)}_0(\theta)} e^{i\omega\tau} \\ & + \underbrace{\left[M^{(-)}_{100} Y_{00}(\theta) + M^{(-)}_{120} Y_{20}(\theta) \right]}_{D^{(-)}_0(\theta)} e^{-i\omega\tau} \Big|^2 , \end{aligned} \tag{6.7}$$

where the term in the first row, $D^{(+)}_0(\theta)$, corresponds to the angle-resolved transition amplitude of the absorption path and the term in the second row, $D^{(-)}_0(\theta)$ corresponds to the emission path. The subscript of $D^{(\pm)}_0(\theta)$ indicates the magnetic quantum number $m = 0$. Equation 6.7 shows that, in general, it is not possible write $S(\theta,\tau)$ as the product of a temporal and an angular factor. This implies that the PAD is delay-dependent and that the delay

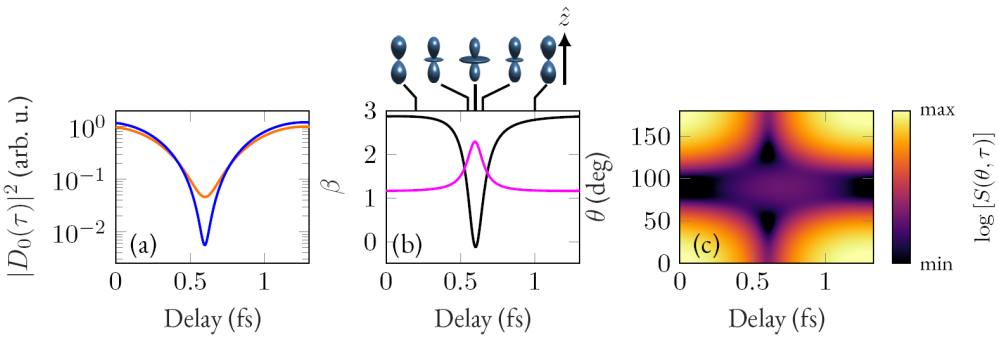

Figure 6.4: Populations $|P_L(\tau)|^2$of the s (blue) and d (orange) states. (b) Asymmetry parameters β_2 (black) and β_4 (magenta) as a function of delay. The insets on top show the 3D PAD at different delays. (c) Sideband intensity as a function of delay and angle. A logarithmic color map is used. Figure adapted from paper v.

is angle-dependent, as observed experimentally in paper iii. Equation 6.7 can be rewritten as follows

$$S(\theta,\tau) \propto \Big| \overbrace{\left[M_{100}^{(+)} e^{i\omega\tau} + M_{100}^{(-)} e^{-i\omega\tau}\right]}^{P_{00}(\tau)} Y_{00}(\theta) + \underbrace{\left[M_{120}^{(+)} e^{i\omega\tau} + M_{120}^{(-)} e^{-i\omega\tau}\right]}_{P_{20}(\tau)} Y_{20}(\theta)\Big|^2, \tag{6.8}$$

where here the term in the first row, $P_{00}(\tau)$ corresponds to the "RABBIT amplitude" associated to the s final state while the term in the second row, $P_{20}(\tau)$ corresponds to the "RABBIT amplitude" associated to the d final state. The second subscript corresponds to m. Equations 6.7 and 6.8 are identical but 6.7 outlines the effect of angular interference in $D_0^{(\pm)}(\theta)$ while 6.8 shows the effect of temporal interference in the "RABBIT amplitudes" $P_{L0}(\tau)$ of the final angular momentum states.

Let us first investigate the evolution of the populations of the s and d states, $|P_{00}|^2$ and $|P_{20}|^2$ respectively, as a function of delay. Figure 6.4(a) shows the sinusoidal oscillation of the populations over one sideband period in a logarithmic scale. Interestingly, we see that around the maximum of the oscillations both populations are similar, while at the minimum the population of the s state drops significantly compared to that of the d state. In other words, the contrast of the oscillations for the s state is higher than for the d state. As we show in paper v, this can be understood based on Fano's propensity rule. Indeed, the absorption and emission paths to a given final angular momentum do not have the same strength. In this case, the CC transition $\varepsilon p \rightarrow \epsilon d$ is stronger for absorption than emission while it is the opposite of the transition $\varepsilon p \rightarrow \epsilon s$. This implies that the contrast of the RABBIT oscillations is smaller

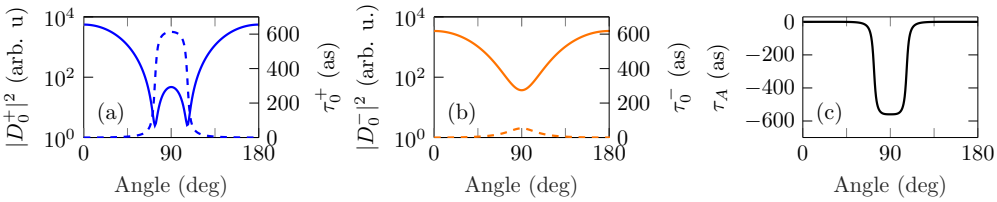

Figure 6.5: (a) Square modulus (solid line) and "time delay" (dashed line) of $D_0^{(+)}(\theta)$. (b) Square modulus (solid line) and "time delay" (dashed line) of $D_0^{(+)}(\theta)$. (c) Angle-resolved atomic time delay difference between emission and absorption.

than one. In addition, Fano's propensity rule tells us that the asymmetry between absorption and emission increases with the final angular momentum (see Fig. 3.2). As a result, the contrast of the oscillations for the s state is larger than for the d state.

The difference in oscillation contrast for the population of the s and d states implies that the contribution of the s and d waves to the total PAD varies as a function of time. In figure 6.4(b) we show the oscillations of the β parameters associated to the PAD together with the 3-dimensional representation of the angular distributions at some specific delays. In Fig. 6.4(c) we present the angle- and delay-resolved sideband intensity in a logarithmic scale. Both figures show a large modification of the angular distribution around the minimum of the sideband oscillation, where the ratio of the populations of the s and d states changes dramatically. The asymmetry between absorption and emission predicted by Fano's propensity rule explains the modifications of the PAD as a function of delay observed in paper III[4].

We now investigate the angular dependence of the absorption and emission transition amplitudes $D_0^{(\pm)}(\theta)$ (Eq. 6.7). Using the asymptotic phase of the matrix elements given in equation 4.4, and neglecting the angular momentum dependence of ϕ_{cc}, $D_0^{(\pm)}(\theta)$ can be approximated here as[5]

$$D_0^{(\pm)}(\theta) \approx e^{i(\eta_1^{(\pm)}+\phi_{cc}^{(\pm)})}\left[|M_{100}^{(\pm)}|Y_{00}(\theta) + |M_{120}^{(\pm)}|Y_{20}(\theta)\right], \tag{6.9}$$

The phase of the first term is simply $\eta_1^{(\pm)} + \phi_{cc}^{(\pm)}$. Since the factor on the right is real, its phase is either equal to 0 or π, depending on its sign. Y_{00} is constant and does not depend on the emission angle, while Y_{20} takes both positive and negative values depending on the emission angle. As a result, depending on the weight $|M_{1L0}^{(\pm)}|$ of the two scattering waves, destructive interference may be observed at specific angles. Figures 6.5(a) and (b) show the

[4]The modification of the PAD with delay always originates from an asymmetry between absorption and emission. However, in resonant photoionization, the relative strength of the different paths is not well described by Fano's propensity rule.

[5]The minus sign in paper V is a typo.

square modulus of $D_0^{(+)}$ and $D_0^{(-)}$. We note that, in the simulations, we use the exact expression of $D_0^{(\pm)}$ given in Eq. 6.7, in which $\phi_{cc}^{(\pm)}$ depends slightly on the angular momentum. In the absorption path we observe very strong destructive interference while in the emission path $|D_0^{(-)}|^2$ varies smoothly as function of the angle. This can be understood from the fact that, in the absorption path, the d wave dominates and Y_{20} changes sign between $0°$ and $90°$. As a result, around $75°$, $|M_{100}^{(+)}|Y_{00}(\theta) + |M_{120}^{(+)}|Y_{20}(\theta)$ crosses zero, leading to destructive interference. In the emission path, it is the s wave that dominates. Here the second term of Eq. 6.9 never changes sign, leading to a smooth variation of $|D_0^{(-)}|^2$.

We also show in Figs. 6.5(a,b) the "time delay" of the absorption/emission paths defined as $\tau_0^{(\pm)} = \arg[D_0^{(\pm)}]/2\omega$. The "time delay" in the absorption path jumps by almost 600 as (π rad is equivalent to 667 as at 800 nm) around the angle at which we observe the destructive interference due to the change of sign. On the contrary, for the emission path, the "time delay" is almost angle independent. As a result, the angle-dependent atomic delay $\tau_A = \tau_0^{(-)} - \tau_0^{(+)}$, exhibits a large delay variation as a function of the angle due to the destructive interference in the absorption path as shown in Fig. 6.5(c). We can conclude that the angle-dependence of the atomic time delays is a second consequence of Fano's propensity rule.

Here we have discussed the case of helium because, the fact that it only has one intermediate state and one magnetic quantum number, significantly simplifies the discussion. However a similar analysis can be done with more complex atoms. In that case, as we show in paper VI, it is important to consider channels with different m individually. Indeed, in the total PAD, the incoherent sum of the angular distributions associated to different ionic states can sometimes hide the asymmetry between absorption and emission, in particular in the case of neon (see paper VI). It can also lead to a complex delay-dependence of the asymmetry parameters and angle-dependence of the time delays. To illustrate the complexity of the problem we consider the non-resonant photoionization of argon.

Figure 6.6 presents an analysis, similar to that performed in helium, of the m-resolved channels in argon. The top row corresponds to $m = 0$ and the bottom row to $m = \pm 1$. As already discussed several times, for $m = 0$, two paths lead to the final p continuum state. As a result, we can see in Fig. 6.6(a) that, unlike in He, the oscillations of the populations for the p and f states are not perfectly in phase. We do, however, still observe that the contrast of the oscillations is higher for the p state than for the f state as expected from the propensity rule. The small phase shift explains, for example, the asymmetric shape of the β_2 oscillations predicted by our calculations in paper V.

In figure 6.6(b), we show the angular distribution for the absorption and emission paths. In the absorption path (blue), we observe two local minima at around $50°$ and $130°$. However, in argon, we aslo see some features in the angular distribution associated to the emission path (orange) around $70°$ and $110°$. The large minimum at $90°$ observed in both absorption and

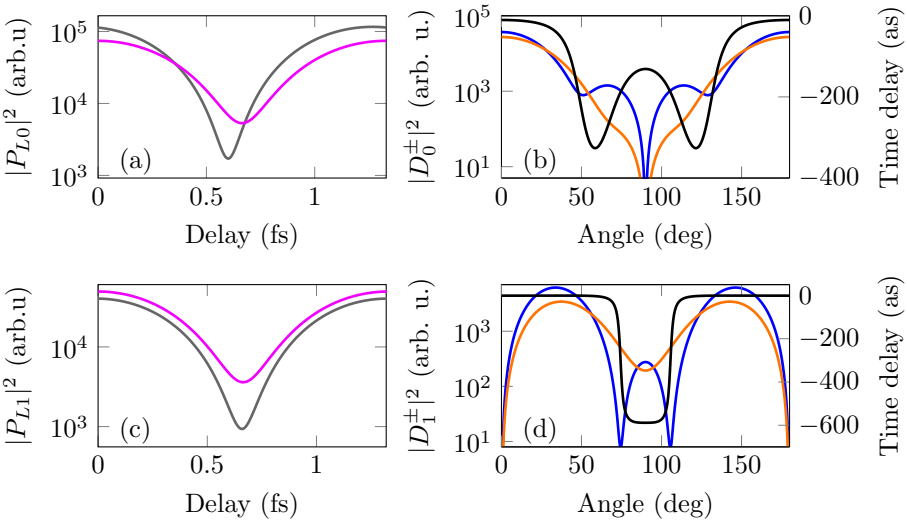

Figure 6.6: Channel-resolved analysis of angle-resolved RABBIT in argon for $m = 0$ (a) and (b) and $m = \pm 1$ (c) and (d). (a) and (c) show the populations of the p (gray) and f (magenta) states. (b) and (d) show the absorption (blue) and emission (orange) angular distributions $|D^{\pm}|^2$ and the corresponding atomic time delay τ_A (black).

emission does not correspond to destructive interference but simply to a common node of the spherical harmonics Y_{10} and Y_{30}. As a result of the interference features observed in both absorption and emission paths, the atomic delay has a more complex angle-dependence. A similar time delay variation had already been predicted by Ivanov and Kheifets for $m = 0$ in neon [131].

In figure 6.6(c), we show the population of the p and f states for $m = \pm 1$. In this case, because there is only one intermediate channel, both oscillations are in phase. Again, as predicted by Fano's propensity rule, at the minimum, the highest angular momentum dominates strongly. Finally, Fig. 6.6(d) shows the angular distribution of the absorption and emission paths and the atomic delay for $m = \pm 1$. In this case, the situation is very similar to that in helium, with strong destructive interference only in the absorption path and a large delay jump as we cross the these interference regions.

In order to reproduce the PADs and angle-resolved time delays measured experimentally in Ar in paper III and V, we have to add incoherently the $m = 0$ and $m = \pm 1$ channels which makes it much more complicated to fully interpret the experimental results without a theoretical back-up. As an example, using the results in figure 6.6, we can understand the shape of the β_2 oscillations reported in paper V as mentioned earlier. In addition the fact that the angle-resolved time delays in Ar, shown in Fig. 6.3(a) start decreasing already at relatively low angles is due to the contribution of the $m = 0$ channel, while the sharp drop of the time

delay at around 75° is due to the $m = \pm 1$ channels. Our theoretical results and methods therefore provide a general framework to analyse and interpret angle-resolved RABBIT measurements.

Finally, as the asymmetry between absorption and emission decreases with electron kinetic energy, both the delay-dependence of the PAD and the angle-dependence of the time delays are reduced. For sufficiently high kinetic energy, where approximations such as the soft-photon approximation [138] or the strong-field approximation [29] are valid, these effects disappear.

Chapter 7

Summary and outlook

1 Summary

In this thesis we have investigated photoionization from a large variety of systems (He, Ne, Ar, Xe and N_2) and via different ionization mechanisms represented schematically in Fig. 7.1. While traditional photoelectron spectroscopy only provides information on the amplitude of the emitted EWPs, our studies, performed with the interferometric technique RABBIT, allow us to measure both the spectral amplitude and phase of the EWPs, which we then use to characterize the EWP in the time-frequency domain and gain detailed information on the attosecond to femtosecond ionization dynamics.

In general, several ionization channels are available. When the channels lead to the same ionic state, they interfere, resulting in fast variations of the spectral amplitude and phase of the EWPs. This is the case for Fano resonances, where direct photoionization and autoionization interfere (papers II, III, VIII), or in the case of angle-resolved measurements, where the coherent superposition of final states with different angular momenta gives rise to interference between the different partial waves (papers III, V, VI). When the channels lead to different ionic states, for example due competing shake-up processes (papers I and IX), spin-orbit splitting of the ion (papers VIII, X) or different Auger decay channels (paper X), the contribution of the different channels add incoherently. In both cases, in order to understand the results, it is necessary to disentangle and analyse the contribution of the different channels. In this work, we have developed and implemented different tools to investigate photoionization dynamics when multiple competing ionization channels are available.

During this thesis, we have continuously worked to increase the spectral resolution of our measurements, showing that it is possible to do attosecond physics while maintaining high spectral resolution. Using attosecond pulse trains in combination with a high-resolution

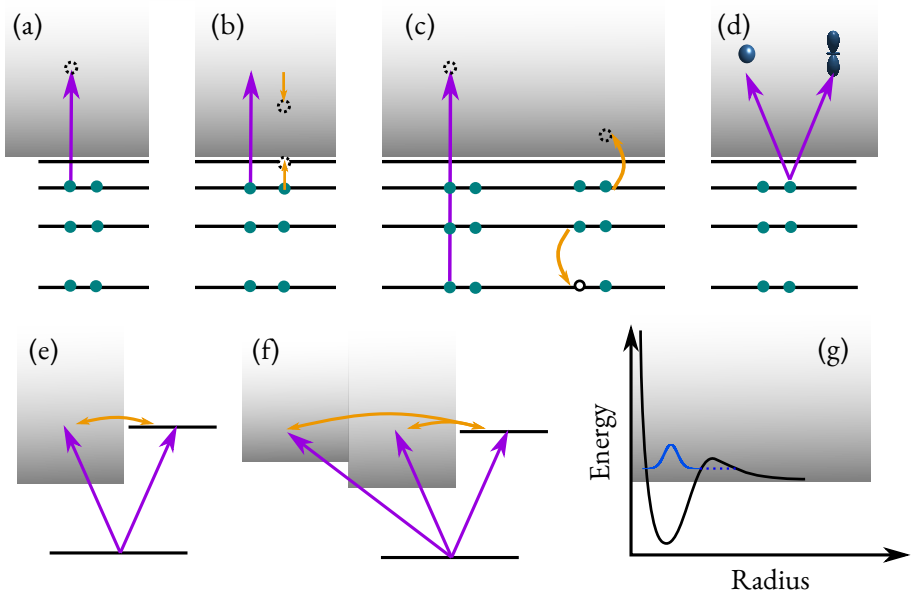

Figure 7.1: Schematic representation of different ionization mechanisms studied in the thesis. (a) Photoionization from a valence shell. (b) Photoionization with shake-up. (c) Photoionization from an inner shell (left) and subsequent Auger decay (right). (d) Angular momentum resolved photoionization to two different partial waves. (e) Photoionization via an autoionizing state interacting with a single continuum. (f) Photoionization via an autoionizing state interacting with several continua. (g) EWP in a shape resonance.

electron spectrometer, long IR probe pulses, the Rainbow RABBIT technique and a deconvolution algorithm can provide a spectral resolution of the order of tens of meV, allowing for an accurate characterization of the emitted EWPs. Advanced detection schemes such as electron-electron coincidence used in paper X are also very powerful tools to separate competing processes, though at the expense of long acquisition times and a higher complexity for the data analysis. The possibility to study photoionization dynamics with high spectral resolution will be increasingly important as the size of the systems under study increases, resulting in more complex photoelectron spectra as was the case in Xe (paper X) and N_2 (paper VII). Finally, angle-resolved measurements can provide complementary information in particular regarding the interplay of different angular channels, which can not be spectrally separated. Angular resolution is a requirement if we want to be able to completely characterize the electron dynamics, not only in the time-frequency domain but also in the position-momentum phase space.

2 Towards attosecond quantum state tomography of photoelectron wavepackets

In chapter 5, we reconstruct the Wigner distribution and density matrix of the EWPs assuming that they are fully coherent. While in this case it is a fair approximation, in general, decoherence can occur, either due to fluctuating experimental conditions [70, 122], or due to relaxation dynamics of the system via channels that are not measured. Both situations result in a loss of information which gives rise to decoherence. To fully understand the ionization dynamics it is hence important to characterize the quantum state of the system without assuming that it is a pure state. This characterization is called quantum state tomography (QST). QST protocols for discrete variables have already been proposed and demonstrated in the field of attosecond science [70, 71, 122]. However, in order to characterize the EWPs we need a QST protocol for continuous variables, which, to our knowledge, does not exist yet for photoelectrons. Towards the end of this thesis, we have explored theoretically two different continuous variable QST protocols which could be implemented experimentally.

The first idea investigated is inspired from the methods used in quantum optics [139, 140]. It relies on mixing an unknown quantum object, here the EWP, with a known classical field, referred as local oscillator in quantum optics which in our case corresponds to the IR probe pulse. Our approach consists in taking advantage of the frequency mixing induced by the finite pulse effects. As shown in figure 3.4, the IR-induced CC transitions makes interfere different parts of the one-photon wavepacket. This results in a modification of the amplitude and phase of the EWP, which depends on the degree of coherence between the different parts of the EWP. In other words, it gives access to the coherences of the density matrix. By recording the spectrum for a large number of delays, we obtain a large enough set of measurements to reconstruct the quantum state of the EWP. It should then be possible to reconstruct the Wigner distribution of the EWP from the measured RABBIT spectrogram using a mixed-state generalized projection algorithm [70]. In collaboration with Charles Bourassin-Bouchet from the Université Paris-Sud and with Pascal Salières' group from the CEA Saclay, the first numerical tests seem to indicate that it is indeed possible to tomographically reconstruct the quantum state of the EWP with this method.

The second idea investigated is inspired from two-dimensional spectroscopy in which three pulses are used to trigger and probe the dynamics [141]. In the traditional RABBIT scheme, the beating between two consecutive harmonics, spaced by $2\hbar\omega$, gives rise to fast oscillations at angular frequency 2ω. If now we use two probe pulses at slightly different frequencies ω and $\omega\delta\omega$, we generate two 2-photon EWPs which are slightly offset in energy with respect to each other. Delaying one probe pulse with respect to the other, results in a beating of the coherent superposition of the two EWPs at angular frequency $\delta\omega$. One can easily show that the amplitude of the $\delta\omega$ oscillations corresponds to $\langle\epsilon|\rho|\epsilon + \hbar\delta\omega\rangle$. Therefore, for a given detuning $\delta\omega$, the variation of the spectral amplitude and phase of the $\delta\omega$ oscillations with

the energy of the sideband, ϵ, gives us a diagonal of the density matrix. Varying $\delta\omega$, we can then map the entire density matrix. Using this method on numerical simulations, we have been able to reconstruct the density matrix of a partially coherent EWP and to measure its purity with good accuracy. In an ongoing collaboration with Daniel Finkelstein Shapiro and Tönu Pullerits from Lund University, we are investigating the possibility to generalize this scheme by implemented the phase cycling method, which used in two-dimensional spectroscopy [142].

The main advantage of this protocol is that it does not rely on a retrieval algorithm to extract the density matrix. However, it would require measuring multiple RABBIT scans, one for each $\delta\omega$. We are now investigating the experimental feasibility of this technique.

Both methods seem very promising and should be investigated in more detail. The goal being, of course, to test them experimentally first on simple systems and then on more complex systems where we can expect decoherence.

3 Towards a complete characterization of EWPs in phase space

One of the goals of attosecond physics is to make a "movie" of electronic motion in various processes. The concept of making a movie, tracking the position of an electron as a function of time is a classical concept. The equivalent of such movie in a quantum mechanical world would be to visualize to the evolution of the Wigner quasi-probability distribution in the position-momentum phase space on the attosecond time scale. This would requires knowing the temporal evolution of the complex amplitude in momentum space $\mathcal{A}(\mathbf{k}, t)$. In chapter 5, we have characterized autoionized EWPs in the time-frequency domain using the Rainbow RABBIT technique. In particular, we have discussed the possibility of reconstructing the temporal evolution the spectral amplitude $\mathcal{A}(E, t)$ from that measured experimentally at $t \to \infty$. In chapter 6, we have investigated photoionization dynamics as a function of the electron kinetic energy and emission direction, *i.e.* as a function momentum. In principle, if we can use the Rainbow RABBIT technique with the angular resolution, we should be able to make a complete measurement of the EWP and recontruct the movie of the electron leaving the atom in phase-space.

Recently, we performed experiments in which we study resonant two-photon ionization in helium. In our experiment, we excite the $3p$ Rydberg state with harmonic 15. The Rydberg state is then ionized upon absorption of an IR photon, resulting in photoelectrons corresponding to SB16 at very low kinetic energy. The aim is to completely characterize the emitted EWP using angle-resolved Rainbow RABBIT measurements with the VMI. In order to benefit from the best resolution we generate harmonics in Xe so that we have only two harmonics above threshold. This allows us to magnify the image on phosphor screen, hence

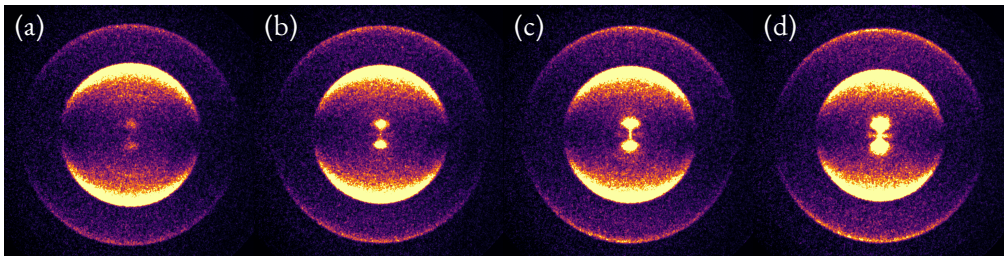

Figure 7.2: Raw VMI images of the electron distribution as the harmonic 15 is tuned towards the $3p$ state. The feature observed at the center of each VMI image corresponds to SB16.

increasing the spectral resolution of the measurements. In addition, the strong ionization enhancement by the intermediate of the $3p$ state together with the high XUV flux obtained when generating in Xe provides us with a very strong signal. The combination of strong electron signal and high spectral resolution allows us to use the angle-resolved Rainbow RABBIT technique. We note that this method has already been demonstrated for molecules [17].

In figure 7.2, we show the images obtained on the phosphor screen as we scan the energy of H15 from off-resonance [Fig. 7.2(a)] to on-resonance [Fig. 7.2(d)]. The electrons emitted via the $3p$ state and corresponding to SB16 give rise to the signal observed at the center of the image. It is interesting to observe how the angular distribution of SB16 changes as we scan the central wavelength. Off-resonance the distribution looks like p orbital while on resonance the distribution looks more like a d orbital. While data is still under analysis, we hope that these measurements will allow us to fully characterize the EWPs in phase-space.

4 Upgrade of the experimental setup

As we move towards increasingly complex experiments requiring numerous RABBIT scans, coincidence measurements and/or angular resolution, the time needed to perform these experiments becomes increasingly large. This sets constraints on the long term stability of the interferometer. For this reason the experimental setup is undergoing a major upgrade. We very recently upgraded the repetition rate of the laser from 1 to 3 kHz, which will decrease the acquisition time for RABBIT scans by a factor 3. In addition, we are planning on rebuilding the attosecond interferometer in order to increase its long and short term stability and replace some of the equipment which has served its time since the first attosecond experiments performed in Lund in 2003. The upgrade of the laser and setup should allow us to perform complex experiments which were out of reach until now and to push further our understanding of attosecond electron dynamics.

Appendix

1 Two-photon finite pulse model

In chapters 3 and 5 we have introduced the two-photon transition amplitudes for both resonant and non resonant transitions without fully introducing all the relevant parameters. Here we provide the complete description of all parameters and functions used to calculate the two-photon transition amplitudes. This is entirely based on reference [62]. The aim of this appendix is to provide all the necessary information in order to be able to reproduce some of the main theoretical results obtained in this thesis.

Let us consider a Gaussian, linearly polarized, pulse with a vector potential given by

$$\tilde{A}(t) = A_0 \exp\left[\frac{\sigma^2}{2}(t-t_0)^2\right] \cos\left[\omega_0(t-t_0)+\varphi\right], \tag{1}$$

where A_0 is the amplitude, ω_0 is the central frequency, t_0 is the central time, σ is the spectral width and φ is the carrier-to-envelope phase of the pulse. The Fourier transform of this pulse has components with positive and negative frequencies, $A(\omega) = A^+(\omega) + A^-(\omega)$, which correspond respectively to the absorption and emission components and are defined as

$$A^{\pm}(\omega) = \frac{A_0}{2\sigma} \exp[i(\omega t_0 \mp \varphi)] \exp\left[-\frac{(\omega \mp \omega_0)^2}{2\sigma^2}\right]. \tag{2}$$

As explained in chapter 3, the two-photon transition amplitude is given by

$$\mathcal{A}_{fg}^{(\pm)}(\Omega_{fg},\tau) = \int_0^\infty E_{\mathrm{IR}}(\Omega_{fg}-\Omega) e^{\pm i(\Omega_{fg}-\Omega)\tau} E_{\mathrm{XUV}}(\Omega) M_{fg}^{(\pm)}(\Omega)\, \mathrm{d}\Omega. \tag{3}$$

In the non-resonant case, Eq. 3 yields [62]

$$\mathcal{A}_{fg}^{(\pm)}(\Omega_{fg},\tau) = i\mathcal{F}(\tau) e^{i\omega\tau} w[z(\Omega_{fg},\tau)], \tag{4}$$

with $\mathcal{F}(\tau)$ a form factor defined as

$$\mathcal{F}(\tau) = -\pi \frac{A_{XUV} A_{IR}}{4\sigma_{XUV}\sigma_{IR}} e^{-i(\varphi_{XUV}+\varphi_{IR})} \exp\left[-\frac{1}{2}\left(\frac{\delta^2}{\sigma^2} + \frac{\tau^2}{\sigma_t^2} + 2i\frac{\sigma_{IR}}{\sigma_{XUV}}\frac{\delta}{\sigma}\frac{\tau}{\sigma_t}\right)\right], \tag{5}$$

where $\sigma = \sqrt{\sigma_{XUV}^2 + \sigma_{IR}^2}$, $\sigma_t = \sqrt{\sigma_{XUV}^{-2} + \sigma_{IR}^{-2}}$ and $\delta = \Omega + \omega - \Omega_{fg}$. The function $w(z)$ is the Faddeeva function defined as

$$w(z) = \frac{i}{\pi}\int_{-\infty}^{+\infty} \frac{e^{-t^2}}{z-t} dt, \quad \mathrm{Im}[z] > 0, \tag{6}$$

and the complex parameter $z(\Omega_{fg}, \tau)$ is given by

$$z(\Omega_{fg}, \tau) = \frac{\sigma_t}{\sqrt{2}}\left[\left(\omega - \frac{\sigma_{IR}^2}{\sigma^2}\delta - i\frac{\tau}{\sigma_t^2}\right) - \Omega_{fg}\right]. \tag{7}$$

For the resonant case the two-photon transition amplitude is given by

$$\mathcal{A}_{fg}(\tau) \approx \mathcal{F}(\tau) e^{\pm i\omega\tau}\left\{w[z(E_f,\tau)] + (\kappa - \epsilon_{E_{f\alpha}}^{-1})(q-i)w[z(E_\alpha,\tau)]\right\}, \tag{8}$$

where $\mathcal{F}(\tau)$, $w(z)$ and $z(E,\tau)$ are defined in the same way as for the non resonant case.

2 Wigner distribution for a Fano resonance

In this appendix we calculate analytically the Wigner distribution of the one-photon Fano resonance profile, which is given by

$$R(\epsilon) = \frac{q+\epsilon}{\epsilon+i} \tag{9}$$

where ϵ is the reduced energy defined as $\epsilon = 2(E - E_\alpha)/\Gamma$, with E_α the resonance energy and Γ the resonance width. The transition amplitude can be Fourier transformed and expressed in the time domain as [121]

$$\tilde{R}(t) = \delta(t) - i\frac{\Gamma}{2\hbar}(q-i)e^{-(i\frac{E_\alpha}{\hbar}+\frac{\Gamma}{2\hbar})t}\Theta(t) \tag{10}$$

The Wigner distribution can be defined in both the spectral and temporal domain:

$$\begin{aligned} W(E,t) &= \int_{-\infty}^{+\infty} \mathrm{d}\tau\, \tilde{R}\left(t+\frac{\tau}{2}\right)\tilde{R}^*\left(t-\frac{\tau}{2}\right)e^{iE\tau/\hbar} \\ &= \frac{1}{2\pi}\int_{-\infty}^{+\infty} \mathrm{d}\varepsilon\, R\left(E+\frac{\varepsilon}{2}\right)R^*\left(E-\frac{\varepsilon}{2}\right)e^{-i\varepsilon t/\hbar} \end{aligned} \tag{11}$$

Starting from the expression of the transition amplitude in the time domain (eq. 10), we can write the Wigner distribution as the sum of four terms:

$$W(E,t) = W_D + W_I + W_{ID} + W_{DI} \tag{12}$$

where W_D, W_I, W_{DI} and W_{ID} are defined as:

$$W_D(E,t) = \int \delta(t+\frac{\tau}{2})\delta(t-\frac{\tau}{2})\,\mathrm{e}^{iE\tau/\hbar}\,\mathrm{d}\tau \tag{13}$$

$$\begin{aligned} W_I(E,t) =& \frac{\Gamma^2}{4\hbar^2}\int (q-i)\mathrm{e}^{-(iE_\alpha/\hbar+\Gamma/2\hbar)\left(t+\frac{\tau}{2}\right)}\Theta\left(t+\frac{\tau}{2}\right) \\ &\times (q+i)\mathrm{e}^{(iE_\alpha/\hbar-\Gamma/2\hbar)\left(t-\frac{\tau}{2}\right)}\Theta\left(t-\frac{\tau}{2}\right)\mathrm{e}^{iE\tau/\hbar}\,\mathrm{d}\tau \end{aligned} \tag{14}$$

$$\begin{aligned} W_{ID}(E,t) =& -i\int \mathrm{d}\tau\,\delta(t-\frac{\tau}{2})\frac{\Gamma}{2\hbar}(q-i) \\ &\times \exp\left[\left(-\frac{iE_\alpha}{\hbar}-\frac{\Gamma}{2\hbar}\right)\left(t+\frac{\tau}{2}\right)\right]\Theta\left(t+\frac{\tau}{2}\right)\mathrm{e}^{iE\tau/\hbar} \end{aligned} \tag{15}$$

$$\begin{aligned} W_{DI}(E,t) =& i\int \mathrm{d}\tau\,\delta(t+\frac{\tau}{2})\frac{\Gamma}{2\hbar}(q+i) \\ &\times \exp\left[\left(\frac{iE_\alpha}{\hbar}-\frac{\Gamma}{2\hbar}\right)\left(t-\frac{\tau}{2}\right)\right]\Theta\left(t-\frac{\tau}{2}\right)\mathrm{e}^{iE\tau/\hbar} \end{aligned} \tag{16}$$

The result for W_D is straightforward: $W_D(E,t) = \delta(t)$.

Let us now calculate W_I:

$$\begin{aligned} W_I(E,t) =& \frac{\Gamma^2}{4\hbar^2}(q^2+1)e^{-\frac{\Gamma t}{\hbar}} \int \mathrm{d}\tau \exp\left[-(i\frac{E_\alpha}{\hbar} + \frac{\Gamma}{2\hbar})\frac{\tau}{2}\right] \\ & \times \exp\left[(-i\frac{E_\alpha}{\hbar} + \frac{\Gamma}{2\hbar})\frac{\tau}{2}\right] e^{i\frac{E\tau}{\hbar}} \Theta(t+\frac{\tau}{2})\Theta(t-\frac{\tau}{2}). \end{aligned} \tag{17}$$

The integral is non zero only if the product $\Theta(t+\frac{\tau}{2})\Theta(t-\frac{\tau}{2})$ is non zero. This condition is fulfilled when $\tau \in [-2t; 2t]$ with $t \geq 0$. Hence we get:

$$W_I(E,t) = \frac{\Gamma^2}{4\hbar^2}(q^2+1)e^{-\frac{\Gamma t}{\hbar}}\Theta(t) \int_{-2t}^{2t} \mathrm{d}\tau \exp\left(i\frac{E-E_\alpha}{\hbar}\tau\right) \tag{18}$$

$$W_I(E,t) = \frac{\Gamma^2}{2\hbar}(q^2+1)e^{-\frac{\Gamma t}{\hbar}}\Theta(t)\frac{\sin\left(2\frac{E-E_\alpha}{\hbar}t\right)}{E-E_\alpha} \tag{19}$$

Now we calculate W_{ID}.

$$\begin{aligned} W_{ID} =& -i\frac{\Gamma}{2\hbar}(q-i)\exp\left[-\left(i\frac{E_\alpha}{\hbar} + \frac{\Gamma}{2\hbar}\right)t\right] \\ & \times \int \mathrm{d}\tau \exp\left(-i\frac{E_\alpha\tau}{2\hbar} - \frac{\Gamma\tau}{4\hbar} + i\frac{E\tau}{\hbar}\right)\Theta\left(t+\frac{\tau}{2}\right)\delta\left(t-\frac{\tau}{2}\right)\mathrm{e}^{iE\tau/\hbar} \end{aligned} \tag{20}$$

$\delta\left(t-\frac{\tau}{2}\right)$ is non zero only when $\tau = 2t$ and $\Theta\left(t+\frac{\tau}{2}\right)$ is non zero for $\tau \geq -2t$. We then get:

$$W_{ID}(E,t) = -i\frac{\Gamma}{2\hbar}(q-i)e^{2i\frac{E-E_\alpha}{\hbar}t}e^{-\frac{\Gamma}{\hbar}t}\Theta(t) \tag{21}$$

Similarly we get for W_{DI}:

$$W_{DI}(E,t) = i\frac{\Gamma}{2\hbar}(q+i)e^{-2i\frac{E-E_\alpha}{\hbar}t}e^{-\frac{\Gamma}{\hbar}t}\Theta(t) \tag{22}$$

We can then write the sum of W_{ID} and W_{DI} as:

$$W_{ID} + W_{DI} = -\frac{\Gamma}{\hbar}e^{-\frac{\Gamma}{\hbar}t}\left[-q\sin\left(2\frac{E-E_\alpha}{\hbar}t\right) + \cos\left(2\frac{E-E_\alpha}{\hbar}t\right)\right]\Theta(t) \tag{23}$$

Note that $W_{ID} + W_{DI} = 2\mathrm{Re}(W_{ID})$, as written in chapter 5 and in paper II.

Author contributions

Paper I: Photoionization in the time and frequency domain

In this paper, we measure the difference in photoionization time delays from the $2s$ and $2p$ shells of neon in the $70 - 100$ eV range. The combination of high spectral and temporal resolution allows us to disentangle direct photoionization from photoionization with shake-up, thereby obtaining excellent agreement with theoretical calculations.

I took part in the experiments and discussions of the results. I participated to the manuscript with comments and feedback.

Paper II: Time-frequency representation of autoionization dynamics in helium

In this paper, we measure the amplitude and phase of EWPs emitted via the $sp2^+$ and $sp3^+$ resonances in helium. For the EWP emitted via the $sp2^+$ resonance, we characterize it in the time-frequency domain allowing us to disentangle the ionization dynamics of the direct and autoionization paths.

I took part in the experiments, did most of the analysis and interpretation of the results. I wrote the code for the finite pulse calculations and performed most of the simulations. I wrote most of the article with input from all the other authors.

Paper III: Anisotropic photoemission time delays close to a Fano resonance

In this paper, we investigate the photoionization time delays in the vicinity of the $3s^{-1}4p$ resonance in argon with angular resolution. We show that the presence of the resonance leads to a complex energy and angle dependence of the photoionzation time delays.

I had a leading role in the operation of the HHG source and attosecond interferometer and

in the analysis and interpretation of the results obtained in Lund. I also made the calculations using the simplified model. I contributed to the manuscript with some of the figures together with comments and feedback.

Paper IV: Accuracy and precision of the RABBIT technique

In this paper, we investigate in detail the performance of the RABBIT technique with simulations. We analyse the effects of the temporal and spatial properties of the light fields and of the experimental procedure.

I extended the finite pulse model to non Fourier-limited calculations. I did all the simulations regarding the effect of the spatial and temporal properties of the light-fields, except for the calculations based on the strong field approximation. I wrote parts of the manuscript in particular regarding my simulations.

Paper V: Fano's propensity rule in angle-resolved attosecond pump-probe photoionization

In this paper, we extend the validity of Fano's propensity rule to laser assisted photoionization. We show that the asymmetry between absorption and emission of an IR photon in the continuum explains the delay-dependence of the PADs and angle-dependence of the photoionization time delays reported in the literature and in particular in paper III. We verify the theoretical results with experimental measurements in argon.

Theoretically, I analysed the theoretical data (matrix elements) calculated by Jimmy Vinbladh from Stockholm University, interpreted the results and made the angle-resolved RABBIT simulations. Experimentally, I had a leading role in the operation of the HHG source and attosecond interferometer and in the data analysis. I wrote the manuscript with input from all the other authors.

Paper VI: Propensity rules and interference effects in laser-assisted photoionization of helium and neon

In this paper, we investigate the photoelectron angular distributions from laser-assisted photoionization of helium and neon. We study the cases where the IR induces one or two transitions between continuum states. We investigate the validity of Fano's propensity rule in the case of multiple continuum-continuum transitions and discuss the effect of interference between multiple paths to the final states.

I participated to the analysis and interpretation of the results. I contributed to the manuscript with comments and feedback.

Paper VII: Attosecond timing of electron emission from a molecular shape resonance

In this paper, we investigate photoionization time delays in the vicinity of the $3\sigma_g^{-1}$ shape resonance in N_2. We measure a delay difference between two vibrational states due to a modification of the internuclear distance of approximately 2 pm during photoionization. This observation indicates a break-down of the Franck-Condon principle.

I participated to the experiments and discussions of the results. I contributed to the manuscript with comments and feedback.

Paper VIII: Spin-orbit resolved spectral phase measurements around a Fano resonance

In this paper, we measure the amplitude and phase of EWPs emitted via $3s^{-1}4p$ resonance in argon. In particular we separate the spectral components associated to the two spin-orbit split states of the ion and reconstruct the ionization dynamics of the spin-orbit separated EWPs.

I participated to the experiments, the data analysis and interpretation of the results. I contributed to the manuscript with comments and feedback.

Paper IX: Attosecond photoionization dynamics in the vicinity of the Cooper minima in argon

In this paper, we measure photoionization time delays in argon in the vicinity of the $3s$ and $3p$ Cooper minima. We obtain good agreement with theory for the $3p$ Cooper minimum but not for the $3s$ Cooper minimum. We explain this disagreement by the presence of multiple of shake-up channels which dominate at the $3s$ Cooper minimum.

I had a leading role in conducting the experiments in Lund, and in the data analysis and the interpretation of the results. I contributed to the manuscript with comments and feedback.

Paper x: Attosecond electron–spin dynamics in Xe 4d photoionization

In this paper, we measure photoionization time delays from the $4d$ shell in xenon close to threshold and in the vicinity of the giant dipole resonance. We show that the dynamics is affected by the interplay of the giant dipole resonance with narrow shape resonances at threshold due to the spin-orbit interaction.

I participated to the experiments and the interpretation of the results. I did the calculations of the Wigner distributions and contributed to the manuscript with comments and feedback.

Acknowledgements

Four years in a foreign country with a culture and language different from yours, where the winters are long, dark and rainy… that could have been very long. Yet, as I write these acknowledgements, I realize how fast these four years as PhD student passed by. For this, I am very grateful to a lot of people who provided help, support and fun, without whom this work would not have been possible.

First, I want to thank my main supervisor Anne L'Huillier for accepting me as a PhD student. Thank you for all the help, encouragements, guidance and freedom you gave me during these years. After your successful career, I truly admire your humility and your passion for science.

I am also very grateful to my co-supervisors Mathieu Gisselbrecht and Marcus Dahlström. Mathieu, thank you the long discussions we've had about physics, academia and life. When I was stuck, you always had a fresh idea to look at the problem differently. Marcus, thank you for all the help and support regarding the theory part of my PhD. I really appreciate that I could come to your office whenever I had a question or a doubt.

A big thank you to the Attolab crew, in particular the people I worked with on the "old setup". From the "old crew", thank you to Marcus Isinger for all the work you did on the data acquisition and data analysis softwares, to Anne Hart for all the questions and interesting discussions, to Miguel Miranda for your magic fixing of the laser and to Saikat Nandi for teaching me how to work with vacuum. Shiyang Zhong, we started at the same time and we'll finish more or less at the same time. Thank you for your patience, and for the expertise and experimental support you provided throughout these four years. A big thank you to the "new crew", who has heard me complain more and more often about the setup and together with whom we went through the crazy month-long campaign last September. Thank you Lana Neoričić for bringing your southern European character and honesty and for the laughter we've had in the lab. Thank you Hugo Laurell for your enthusiasm and constant optimism (because who knows, the problem might fix itself ;)) and for the many discussions and brainstorming sessions we've had the last two years. Finally, thank you Robin Weissenbilder for sharing my opinions on teaching and for acknowledging that the remote control for the gas cell works like a charm since I "fixed it".

Because there is no experiment without a working laser, there would be no results without Cord Arnold. Thank you for all the help with the laser, with plumbing and for sharing your knowledge in optics.

During this PhD I've had the opportunity to collaborate with many other groups which I want to thank. Most of the results obtained during this thesis would not have been possible without the the MBES. Thank you Richard Squibb and Raimund Feifel for lending us the MBES and helping us getting the best out it during the experimental campaigns. I also want to thank Pascal Salières, Lou Barreau, Margherita Turconi, Christina Alexandridi and Dominique Platzer for a very nice and productive collaboration since I started my Master thesis.

As an experimental group, we have collaborated with many theory groups both in Sweden and abroad who provided the theoretical support needed to understand in detail the physics behind our experimental observations. For this, I want to thank Eva Lindroth, Jimmy Vinbladh, Mattias Bertolino, Felipe Zapata Abelan, Göran Wendin, Fernando Martín, Alicia Palacios, Etienne Plésiat, Leon Petersson, Álvaro Jiménez Gálan, Richard Taïeb and Jeremy Caillat. A special thank you to Luca Argenti who helped me get my "finite pulse" code working at the begging of my PhD after quite some struggles. I am also very grateful to Daniel Finkelstein Shapiro for the help and discussion regarding decoherence and Fano resonances. This really help us move forward after more than a year being stuck with our results.

I want to thank everyone in the atto group for being such a nice, helpful and friendly bunch of people. Thank you Neven "Locokovic" for all the nonsense conversations during the coffee breaks and for keeping track of the lunch points. Thank you for never agreeing with me. We tried agreeing sometimes but it wasn't as fun. Thank you Jasper and Hampus for the physics and non-physics discussions we've had around a coffee or a beer and for all the fun we've had at summer schools and conferences. Thank you Emma for being my official gesture-to-English translator, for teaching me that English is basically mispronounced French and for sharing the struggles of learning Swedish. Thank you Sylvain for all the help with VMI experiments, for the French jokes and for being even more critical than I am with Swedish food. Thank you Samuel for being such a genuinely nice person and for the game nights at your place. Thank you Jan L for all the bad puns. Thank you Chen, Anne-Lise and Yu-Chen for the lunches and coffee breaks that we shared. Tack så mycket Anna for the chats we've had in Swedish after a few beers, I learned as much as in the Swedish class. Thank you Sara for the nice discussions we've had when travelling to different conferences and schools and on other occasions.

спасибо to the Russian crew, Ivan and Alexander for all the after works, for teaching me some of the most important Russian words and the art drinking vodka with закуска. Thanks to the two of you and to Fabian L for the nice winter trip(s) to Kiruna and Abisko.

Many more current or past members of the atto group have contributed to the nice and relaxed working atmosphere. Thank you Jan V, Maria, Albin, Stefanos, Lisa, Esben, Hélène,

Hugo D, Piotr, Per, Johan, Filippo, Fabian B, Maïté, Marius, the three Balázs, Linnea, Alexandre, Ingrid, Maria, Shekhar, Simon, Timothé and the people I might have forgotten here.

If we can focus most of our time on research, it is because there are always people in the background making sure that the activities at the Atomic physics division run smoothly. For all their essential work, I am very grateful to the head of the division Claes-Göran Wahlström and to the administrative and technical staff Anne Petersson Jungbeck, Jakob Testad and Åke Johansson.

While I have mostly interacted with people from the atto group, people from all the other groups in the division have contributed to making the Atomic physics division a great work place with a friendly and relaxed atmosphere. Thank you for all the Monday cakes, Christmas dinners, division outings and corridor chats.

Merci aux marseillais J-B, Nico, Amélie, Fiona, Joffrey, Benoit, Laura, Mathieu, Marie, Damien, Audrey, peu importe le temps et la distance, quand on se retrouve j'ai l'impression de n'être jamais parti. Merci pour cette amitié unique qui dure depuis plus de dix ans.

Para terminar, quiero agradecer a mi familia por haberme apoyado todos estos años y por entender lo que es trabajar en el mundo académico que tan poca gente conoce. ¡Y, lo más importante, gracias por haberme traído lomo y chorizo para que no me muera de hambre!

References

[1] A. Shayeghi, P. Rieser, G. Richter, U. Sezer, J. H. Rodewald, P. Geyer, T. J. Martinez, and M. Arndt. Matter-wave interference of a native polypeptide. *Nat. Communi.*, 11(1):1–8, 2020.

[2] H. Hertz. Ueber einen Einfluss des ultravioletten Lichtes auf die electrische Entladung. *Ann. Physik*, 267:983, 1887.

[3] A. Einstein. Über einen die erzeugung und verwandlung des lichtes betreffenden heuristischen gesichtspunkt. *Ann. Physik*, 322(6):132–148, 1905.

[4] A. McPherson, G. Gibson, H. Jara, U. Johann, T. S. Luk, I. A. McIntyre, K. Boyer, and C. K. Rhodes. Studies of multiphoton production of vacuum-ultraviolet radiation in the rare gases. *J. Opt. Soc. Am. B*, **4**:595, 1987.

[5] M. Ferray, A. L'Huillier, X. Li, L. Lompre, G. Mainfray, and C. Manus. Multiple-harmonic conversion of 1064 nm radiation in rare gases. *J. Phys. B*, **21**:L31, 1988.

[6] P. Paul, E. Toma, P. Breger, G. Mullot, F. Augé, P. Balcou, H. Muller, and P. Agostini. Observation of a train of attosecond pulses from high harmonic generation. *Science*, 292:1689, 2001.

[7] F. Krausz and M. Ivanov. Attosecond physics. *Reviews of Modern Physics*, 81(1):163, 2009.

[8] F. Calegari, G. Sansone, S. Stagira, C. Vozzi, and M. Nisoli. Advances in attosecond science. *J. Phys. B: At. Mol Opt. Phy.*, 49(6):062001, 2016.

[9] K. Klünder, J. M. Dahlström, M. Gisselbrecht, T. Fordell, M. Swoboda, D. Guénot, P. Johnsson, J. Caillat, J. Mauritsson, A. Maquet, R. Taïeb, and A. L'Huillier. Probing single-photon ionization on the attosecond time scale. *Phys. Rev. Lett.*, 106:143002, 2011.

[10] E. P. Månsson, D. Guénot, C. L. Arnold, D. Kroon, S. Kasper, J. M. Dahlström, E. Lindroth, A. S. Kheifets, A. L'Huillier, S. L. Sorensen, et al. Double ionization probed on the attosecond timescale. *Nat. Phys.*, 10:207–211, 2014.

[11] M. Kotur, D. Guénot, A. Jiménez-Galán, D. Kroon, E. W. Larsen, M. Louisy, S. Bengtsson, M. Miranda, J. Mauritsson, C. L. Arnold, S. E. Canton, M. Gisselbrecht, T. Carette, J. M. Dahlström, E. Lindroth, A. Maquet, L. Argenti, F. Martín, and A. L'Huillier. Spectral phase measurement of a Fano resonance using tunable attosecond pulses. *Nat. Comm.*, 7:10566–, 2016.

[12] S. Heuser, Á. J. Galán, C. Cirelli, C. Marante, M. Sabbar, R. Boge, M. Lucchini, L. Gallmann, I. Ivanov, A. S. Kheifets, et al. Angular dependence of photoemission time delay in helium. *Physical Review A*, 94(6):063409, 2016.

[13] V. Gruson, L. Barreau, Á. Jiménez-Galan, F. Risoud, J. Caillat, A. Maquet, B. Carré, F. Lepetit, J.-F. Hergott, T. Ruchon, L. Argenti, R. Taïeb, F. Martín, and P. Salières. Attosecond dynamics through a fano resonance: Monitoring the birth of a photoelectron. *Science*, 354(6313):734–738, 2016.

[14] I. Jordan, M. Huppert, S. Pabst, A. S. Kheifets, D. Baykusheva, and H. J. Wörner. Spin-orbit delays in photoemission. *Physical Review A*, 95(1):013404, 2017.

[15] S. Haessler, B. Fabre, J. Higuet, J. Caillat, T. Ruchon, P. Breger, B. Carré, E. Constant, A. Maquet, E. Mével, P. Salières, R. Taïeb, and Y. Mairesse. Phase-resolved attosecond near-threshold photoionization of molecular nitrogen. *Phys. Rev. A*, 80:011404, 2009.

[16] M. Huppert, I. Jordan, D. Baykusheva, A. Von Conta, and H. J. Wörner. Attosecond delays in molecular photoionization. *Phys. Rev. Lett.*, 117(9):093001, 2016.

[17] S. Beaulieu, A. Comby, A. Clergerie, J. Caillat, D. Descamps, N. Dudovich, B. Fabre, R. Géneaux, F. Légaré, S. Petit, et al. Attosecond-resolved photoionization of chiral molecules. *Science*, 358(6368):1288–1294, 2017.

[18] L. Cattaneo, J. Vos, R. Y. Bello, A. Palacios, S. Heuser, L. Pedrelli, M. Lucchini, C. Cirelli, F. Martín, and U. Keller. Attosecond coupled electron and nuclear dynamics in dissociative ionization of h 2. *Nat. Phys.*, 14(7):733–738, 2018.

[19] J. Vos, L. Cattaneo, S. Patchkovskii, T. Zimmermann, C. Cirelli, M. Lucchini, A. Kheifets, A. S. Landsman, and U. Keller. Orientation-dependent stereo wigner time delay and electron localization in a small molecule. *Science*, 360(6395):1326–1330, 2018.

[20] R. Locher, L. Castiglioni, M. Lucchini, M. Greif, L. Gallmann, J. Osterwalder, M. Hengsberger, and U. Keller. Energy-dependent photoemission delays from noble metal surfaces by attosecond interferometry. *Optica*, 2(5):405–410, 2015.

[21] L. Kasmi, M. Lucchini, L. Castiglioni, P. Kliuiev, J. Osterwalder, M. Hengsberger, L. Gallmann, P. Krüger, and U. Keller. Effective mass effect in attosecond electron transport. *Optica*, 4(12):1492–1497, 2017.

[22] M. Schultze, M. Fieß, N. Karpowicz, J. Gagnon, M. Korbman, M. Hofstetter, S. Neppl, A. L. Cavalieri, Y. Komninos, T. Mercouris, C. A. Nicolaides, R. Pazourek, S. Nagele, J. Feist, J. Burgdörfer, A. M. Azzeer, R. Ernstorfer, R. Kienberger, U. Kleineberg, E. Goulielmakis, F. Krausz, and V. S. Yakovlev. Delay in photoemission. *Science*, 328:1658–1662, 2010.

[23] J. Itatani, J. Levesque, D. Zeidler, H. Niikura, H. Pépin, J. C. Kieffer, P. B. Corkum, and D. M. Villeneuve. Tomographic imaging of molecular orbitals. *Nature*, 432:867, 2004.

[24] G. Steinmeyer. A review of ultrafast optics and optoelectronics. *Journal of Optics A: Pure and Applied Optics*, 5(1):R1, 2002.

[25] D. Strickland and G. Mourou. Compression of amplified chirped optical pulses. *Opt. Commun.*, **56**:219, 1985.

[26] O. Martinez. 3000 times grating compressor with positive group velocity dispersion: Application to fiber compensation in 1.3-1.6 μm region. *Quantum Electronics, IEEE Journal of*, 23(1):59 – 64, 1987.

[27] K. C. Kulander, K. J. Schafer, and J. L. Krause. Dynamics of short-pulse excitation, ionization and harmonic conversion. In *Super-Intense Laser-Atom Physics*. Plenum Press, New York, 1993.

[28] P. B. Corkum. Plasma perspective on strong field multiphoton ionization. *Physical Review Letters*, 71(13):1994, 1993.

[29] M. Lewenstein, P. Balcou, M. Ivanov, A. L'Huillier, and P. Corkum. Theory of high-order harmonic generation by low-frequency laser fields. *Phys. Rev. A*, 49:2117, 1994.

[30] T. Popmintchev, M.-C. Chen, D. Popmintchev, P. Arpin, S. Brown, S. Ališauskas, G. Andriukaitis, T. Balciunas, O. Mücke, A. Pugzlys, A. Baltuska, B. Shim, S. Schrauth, A. Gaeta, C. Hernández-Garcia, L. Plaja, A. Becker, A. J.-B., M. Murnane, and H. Kapteyn. Bright coherent ultrahigh harmonics in the keV X-ray regime from mid-infrared femtosecond lasers. *Science*, 336(6086):1287–1291, 2012.

[31] J. Pupeikis, P.-A. Chevreuil, N. Bigler, L. Gallmann, C. R. Phillips, and U. Keller. Water window soft x-ray source enabled by a 25 w few-cycle 2.2 μm opcpa at 100 khz. *Optica*, 7(2):168–171, 2020.

[32] C. M. Heyl, C. L. Arnold, A. Couairon, and A. L'Huillier. Introduction to macroscopic power scaling principles for high-order harmonic generation. *J. Phys. B: At., Mol. Opt. Phys.*, 50(1):013001, 2017.

[33] C. G. Wahlström, J. Larsson, A. Persson, T. Starczewski, S. Svanberg, P. Salieres, P. Balcou, and A. L'Huillier. High-order harmonic generation in rare gases with an intense short-pulse laser. *Phys. Rev. A*, 48:4709, 1993.

[34] Y. Mairesse, A. de Bohan, L. J. Frasinski, H. Merdji, L. C. Dinu, P. Monchicourt, P. Breger, M. Kovačev, R. Taïeb, B. Carré, H. G. Muller, P. Agostini, and P. Salières. Attosecond synchronization of high-harmonic soft X-rays. *Science*, 302:1540, 2003.

[35] K. Varjú, Y. Mairesse, B. Carre, M. B. Gaarde, P. Johnsson, S. Kazamias, R. Lopez-Martens, J. Mauritsson, K. J. Schafer, P. Balcou, A. L'Huillier, and P. Salières. Frequency chirp of harmonic and attosecond pulses. *J. Mod. Opt.*, 52:379, 2005.

[36] L. Quintard, V. Strelkov, J. Vabek, O. Hort, A. Dubrouil, D. Descamps, F. Burgy, C. Péjot, E. Mével, F. Catoire, and E. Constant. Optics-less focusing of XUV high-order harmonics. *Science Advances*, 5(4):eaau7175, 2019.

[37] C. Guo, A. Harth, S. Carlström, Y.-C. Cheng, S. Mikaelsson, E. Mårsell, C. Heyl, M. Miranda, M. Gisselbrecht, M. B. Gaarde, K. J. Schafer, A. Mikkelsen, J. Mauritsson, C. L. Arnold, and A. L'Huillier. Phase control of attosecond pulses in a train. *J. Phys. B: At., Mol. Opt. Phys.*, 51(3):034006, 2018.

[38] H. Wikmark, C. Guo, J. Vogelsang, P. W. Smorenburg, H. Coudert-Alteirac, J. Lahl, J. Peschel, P. Rudawski, H. Dacasa, S. Carlström, S. Maclot, M. B. Gaarde, P. Johnsson, C. L. Arnold, and A. L'Huillier. Spatiotemporal coupling of attosecond pulses. *Proceedings of the National Academy of Sciences*, 2019.

[39] D. Kroon, D. Guénot, M. Kotur, E. Balogh, E. Larsen, C. Heyl, M. Miranda, M. Gisselbrecht, J. Mauritsson, P. Johnsson, et al. Attosecond pulse walk-off in high-order harmonic generation. *Opt. Lett.*, 39(7):2218–2221, 2014.

[40] E. Constant, D. Garzella, P. Breger, E. Mével, C. Dorrer, C. L. Blanc, F. Salin, and P. Agostini. Optimizing High Harmonic Generation in Absorbing Gases: Model and Experiment. *Phys. Rev. Lett.*, 82:1668, 1999.

[41] G. Farkas and C. Tóth. Proposal for attosecond light pulse generation using laser induced multiple-harmonic conversion processes in rare gases. *Phys. Lett. A*, **168**:447, 1992.

[42] S. E. Harris, J. J. Macklin, and T. W. Hänsch. Atomic scale temporal structure inherent to high-order harmonic generation. *Opt. Commun.*, **100**:487, 1993.

[43] E. Wigner. On the Quantum Correction For Thermodynamic Equilibrium. *Phys. Rev.*, **40**:749, 1932.

[44] J. Ville. Théorie et applications de la notion de signal analytique. *Cables et transmission*, 2A:61–74, 1948.

[45] L. Cohen. Time-frequency distributions-a review. *Proceedings of the IEEE*, 77(7):941–981, 1989.

[46] M. Wickenhauser, J. Burgdörfer, F. Krausz, and M. Drescher. Time Resolved Fano Resonances. *Phys. Rev. Lett.*, 94:023002, 2005.

[47] G. Cheriaux, P. Rousseau, F. Salin, J. P. Chambaret, B. Walker, and L. F. Dimauro. Aberration-free stretcher design for ultrashort-pulse amplification. *Opt. Lett.*, 21(6):414–416, 1996.

[48] F. Verluise, V. Laude, Z. Cheng, C. Spielmann, and P. Tournois. Amplitude and Phase Control of Ultrashort Pulses by Use of an Acousto-Optic Programmable Dispersive Filter: Pulse Compression and Shaping. *Opt. Lett.*, 25:575–577, 2000.

[49] . E. Martinez. Grating and prism compressors in the case of finite beam size. *J. Opt. Soc. Am. B*, 3:929, 1986.

[50] A. Moulet, S. Grabielle, C. Cornaggia, N. Forget, and T. Oksenhendler. Single-shot, high-dynamic-range measurement of sub-15 fs pulses by self-referenced spectral interferometry. *Opt. Lett.*, 35(22):3856–3858, 2010.

[51] T. Oksenhendler, D. Kaplan, P. Tournois, G. Greetham, and F. Estable. Intracavity acousto-optic programmable gain control for ultra-wide-band regenerative amplifiers. *Applied Physics B: Lasers and Optics*, 83(4):491–494, 2006.

[52] A. Sorokin, M. Wellhöfer, S. Bobashev, K. Tiedtke, and M. Richter. X-ray-laser interaction with matter and the role of multiphoton ionization: Free-electron-laser studies on neon and helium. *Phys. Rev. A*, 75(5):051402, 2007.

[53] N. A. Papadogiannis, L. A. A. Nikolopoulos, D. Charalambidis, G. D. Tsakiris, P. Tzallas, and K. Witte. Two-photon ionization of He through a superposition of higher harmonics. *Phys. Rev. Lett.*, **90**:133902, 2003.

[54] B. Manschwetus, L. Rading, F. Campi, S. Maclot, H. Coudert-Alteirac, J. Lahl, H. Wikmark, P. Rudawski, C. M. Heyl, B. Farkas, T. Mohamed, A. L'Huillier, and P. Johnsson. Two-photon double ionization of neon using an intense attosecond pulse train. *Phys. Rev. A*, 93:061402, 2016.

[55] B. Bergues, D. Rivas, M. Weidman, A. Muschet, W. Helml, A. Guggenmos, V. Pervak, U. Kleineberg, G. Marcus, R. Kienberger, et al. Tabletop nonlinear optics in the 100-ev spectral region. *Optica*, 5(3):237–242, 2018.

[56] K. Midorikawa, Y. Nabekawa, and A. Suda. Xuv multiphoton processes with intense high-order harmonics. *Progress in Quantum Electronics*, 32(2):43–88, 2008.

[57] D. Guénot, K. Klünder, C. L. Arnold, D. Kroon, J. M. Dahlström, M. Miranda, T. Fordell, M. Gisselbrecht, P. Johnsson, J. Mauritsson, E. Lindroth, A. Maquet, R. Taï eb, A. L'Huillier, and A. S. Kheifets. Photoemission-time-delay measurements and calculations close to the 3*s*-ionization-cross-section minimum in ar. *Phys. Rev. A*, 85:053424, 2012.

[58] J. M. Dahlström, D. Guénot, K. Klünder, M. Gisselbrecht, J. Mauritsson, A. L'Huillier, A. Maquet, and R. Taïeb. Theory of attosecond delays in laser-assisted photoionization. *Chem. Phys.*, 414:53–64, 2013.

[59] U. Fano. Propensity rules: An analytical approach. *Phys. Rev. A*, 32:617–618, 1985.

[60] J. W. Cooper. Photoionization from Outer Atomic Subshells. A Model Study. *Phys. Rev.*, 128:681, 1962.

[61] A. Jiménez-Galán, L. Argenti, and F. Martín. Modulation of Attosecond Beating in Resonant Two-Photon Ionization. *Phys. Rev. Lett.*, 113(26):263001, 2014.

[62] Á. Jiménez-Galán, F. Martín, and L. Argenti. Two-photon finite-pulse model for resonant transitions in attosecond experiments. *Physical Review A*, 93(2):023429, 2016.

[63] V. Véniard, R. Taïeb, and A. Maquet. Phase dependence of (N+1) - color (N>1) ir-uv photoionization of atoms with higher harmonics. *Phys. Rev. A*, **54**:721, 1996.

[64] H. Muller. Reconstruction of attosecond harmonic beating by interference of two-photon transitions. *Appl. Phys. B*, **74**:17, 2002.

[65] Y.-C. Cheng, S. Mikaelsson, S. Nandi, L. Rämisch, C. Guo, S. Carlström, A. Harth, J. Vogelsang, M. Miranda, C. L. Arnold, et al. Controlling photoionization using attosecond time-slit interferences. *Proceedings of the National Academy of Sciences*, 2020.

[66] R. Lopez-Martens, K. Varjú, P. Johnsson, J. Mauritsson, Y. Mairesse, P. Salieres, M. B. Gaarde, K. J. Schafer, A. Persson, S. Svanberg, et al. Amplitude and phase control of attosecond light pulses. *Physical Review Letters*, 94(3):033001, 2005.

[67] C. Bourassin-Bouchet, M. Stephens, S. De Rossi, F. Delmotte, and P. Chavel. Duration of ultrashort pulses in the presence of spatio-temporal coupling. *Opt. Express*, 19(18):17357, 2011.

[68] C. Bourassin-Bouchet, S. de Rossi, F. Delmotte, and P. Chavel. Spatiotemporal distortions of attosecond pulses. *JOSA A*, 27(6):1395–1403, 2010.

[69] C. Bourassin-Bouchet, M. M. Mang, F. Delmotte, P. Chavel, and S. de Rossi. How to focus an attosecond pulse. *Opt. Express*, 21(2):2506–2520, 2013.

[70] C. Bourassin-Bouchet and M.-E. Couprie. Partially coherent ultrafast spectrography. *Nat. Commun.*, 6(1):1–7, 2015.

[71] K. E. Priebe, C. Rathje, S. V. Yalunin, T. Hohage, A. Feist, S. Schäfer, and C. Ropers. Attosecond electron pulse trains and quantum state reconstruction in ultrafast transmission electron microscopy. *Nat. Phot.*, 11(12):793–797, 2017.

[72] D. Kroon. *Attosecond interferometry: techniques and spectroscopy*. Lund University, 2016.

[73] J. Vaughan, J. Bahder, B. Unzicker, D. Arthur, M. Tatum, T. Hart, G. Harrison, S. Burrows, P. Stringer, and G. M. Laurent. Design of an optically-locked interferometer for attosecond pump-probe setups. *Opt. Express*, 27(21):30989–31000, 2019.

[74] P. Kruit and F. H. Read. Magnetic field paralleliser for 2π electron-spectrometer and electron-image magnifier. *J. Phys. E*, 16:313, 1983.

[75] C.-Y. Cha, G. Ganteför, and W. Eberhardt. New experimental setup for photoelectron spectroscopy on cluster anions. *Rev. Sci. Instr.*, 63(12):5661–5666, 1992.

[76] J. H. Eland, O. Vieuxmaire, T. Kinugawa, P. Lablanquie, R. Hall, and F. Penent. Complete two-electron spectra in double photoionization: The rare gases ar, kr, and xe. *Physical review letters*, 90(5):053003, 2003.

[77] W. H. Richardson. Bayesian-based iterative method of image restoration*. *J. Opt. Soc. Am.*, 62(1):55–59, 1972.

[78] L. B. Lucy. An iterative technique for the rectification of observed distributions. *The astronomical journal*, 79:745, 1974.

[79] L. Rading, J. Lahl, S. Maclot, F. Campi, H. Coudert-Alteirac, B. Oostenrijk, J. Peschel, H. Wikmark, P. Rudawski, M. Gisselbrecht, and P. Johnsson. A versatile velocity map ion-electron covariance imaging spectrometer for high-intensity XUV experiments. *Applied Sciences*, 8(6):998, 2018.

[80] A. T. J. B. Eppink and D. H. Parker. Velocity map imaging of ions and electrons using electrostatic lenses: Application in photoelectron and photofragment ion imaging of molecular oxygen. *Rev. Sci. Instr.*, 68:3477, 1997.

[81] K. Zhao, T. Colvin, W. Hill III, and G. Zhang. Deconvolving two-dimensional images of three-dimensional momentum trajectories. *Rev. Sci. Instr.*, 73(8):3044–3050, 2002.

[82] M. J. J. Vrakking. An iterative procedure for the inversion of two-dimensional ion/photoelectron imaging experiments. *Rev. Sci. Instr.*, 72:4084, 2001.

[83] G. A. Garcia, L. Nahon, and I. Powis. Two-dimensional charged particle image inversion using a polar basis function expansion. *Rev. Sci. Instr.*, 75(11):4989–4996, 2004.

[84] A. Maquet, J. Caillat, and R. Taïeb. Attosecond delays in photoionization: time and quantum mechanics. *J. Phys. B: At. Mol. Opt. Phys.*, 47(20):204004, 2014.

[85] R. Pazourek, S. Nagele, and J. Burgdörfer. Attosecond chronoscopy of photoemission. *Rev. Mod. Phys.*, 87:765–802, 2015.

[86] J. M. Dahlström and E. Lindroth. Study of attosecond delays using perturbation diagrams and exterior complex scaling. *J. Phys. B*, 47(12):124012, 2014.

[87] J. Dahlström, T. Carette, and E. Lindroth. Diagrammatic approach to attosecond delays in photoionization. *Phys. Rev. A*, 86(6):061402, 2012.

[88] A. Kheifets. Time delay in valence-shell photoionization of noble-gas atoms. *Phys. Rev. A*, 87(6):063404, 2013.

[89] E. P. Wigner. Lower limit for the energy derivative of the scattering phase shift. *Phys. Rev.*, 98:145–147, 1955.

[90] L. D. Landau and E. M. Lifshitz. *Quantum mechanics: non-relativistic theory*, volume 3. Elsevier, 2013.

[91] A. S. Kheifets, A. W. Bray, and I. Bray. Attosecond time delay in photoemission and electron scattering near threshold. *Physical review letters*, 117(14):143202, 2016.

[92] E. Lindroth and J. M. Dahlström. Attosecond delays in laser-assisted photodetachment from closed-shell negative ions. *Phys. Rev. A*, 96(1):013420, 2017.

[93] J. Fuchs, N. Douguet, S. Donsa, F. Martin, J. Burgdörfer, L. Argenti, L. Cattaneo, and U. Keller. Time delays from one-photon transitions in the continuum. *Optica*, 7(2):154–161, 2020.

[94] D. Guénot, D. Kroon, E. Balogh, E. Larsen, M. Kotur, M. Miranda, T. Fordell, P. Johnsson, J. Mauritsson, M. Gisselbrecht, et al. Measurements of relative photoemission time delays in noble gas atoms. *J. Phys. B*, 47(24):245602, 2014.

[95] J. Itatani, F. Quéré, G. L. Yudin, M. Y. Ivanov, F. Krausz, and P. B. Corkum. Attosecond Streak Camera. *Phys. Rev. Lett.*, 88:173903, 2002.

[96] L. Cattaneo, J. Vos, M. Lucchini, L. Gallmann, C. Cirelli, and U. Keller. Comparison of attosecond streaking and rabbitt. *Opt. Express*, 24(25):29060–29076, 2016.

[97] U. Becker, R. Wehlitz, O. Hemmers, B. Langer, and A. Menzel. Observation of participator auger decay following valence photoionization with excitation. *Phys. Rev. Lett.*, 63:1054–1057, 1989.

[98] J. Feist, O. Zatsarinny, S. Nagele, R. Pazourek, J. Burgdörfer, X. Guan, K. Bartschat, and B. I. Schneider. Time delays for attosecond streaking in photoionization of neon. *Phys. Rev. A*, 89:033417, 2014.

[99] A. F. Starace. Photoionization of argon and xenon including final-state correlation. *Phys. Rev. A*, 2(1):118, 1970.

[100] W. Wijesundera and H. P. Kelly. Correlation satellites in the photoelectron spectrum of argon. *Phys. Rev. A*, 39(2):634, 1989.

[101] D. Azoury, O. Kneller, S. Rozen, B. D. Bruner, A. Clergerie, Y. Mairesse, B. Fabre, B. Pons, N. Dudovich, and M. Krüger. Electronic wavefunctions probed by all-optical attosecond interferometry. *Nat. Phot.*, 13(1):54–59, 2019.

[102] U. Fano. Effects of configuration interaction on intensities and phase shifts. *Phys. Rev.*, 124(6):1866, 1961.

[103] D. L. Ederer. Photoionization of the 4d electrons in xenon. *Phys. Rev. Lett.*, 13:760, 1964.

[104] J. W. Cooper. Interaction of maxima in the absorption of soft x rays. *Phys. Rev. Lett.*, 13:762–764, 1964.

[105] M. Sabbar, S. Heuser, R. Boge, M. Lucchini, T. Carette, E. Lindroth, L. Gallmann, C. Cirelli, and U. Keller. Resonance effects in photoemission time delays. *Phys. Rev. Lett.*, 115:133001, 2015.

[106] L. Argenti, A. Jiménez-Galán, J. Caillat, R. Taïeb, A. Maquet, and F. Martín. Control of photoemission delay in resonant two-photon transitions. *Phys. Rev. A*, 95:043426, 2017.

[107] J. W. Cooper, U. Fano, and F. Prats. Classification of two-electron excitation levels of helium. *Phys. Rev. Lett.*, 10:518–521, 1963.

[108] J.-E. Rubensson, C. Såthe, S. Cramm, B. Kessler, S. Stranges, R. Richter, M. Alagia, and M. Coreno. Influence of the radiative decay on the cross section for double excitations in helium. *Phys. Rev. Lett.*, 83:947–950, 1999.

[109] M. Domke, K. Schulz, G. Remmers, G. Kaindl, and D. Wintgen. High-resolution study of $^1p^o$ double-excitation states in helium. *Phys. Rev. A*, 53:1424–1438, 1996.

[110] S. Sorensen, T. Åberg, J. Tulkki, E. Rachlew-Källne, G. Sundström, and M. Kirm. Argon 3s autoionization resonances. *Phys. Rev. A*, 50(2):1218, 1994.

[111] R. P. Madden and K. Codling. New autoionizing atomic energy levels in he, ne, and ar. *Phys. Rev. Lett.*, 10:516–518, 1963.

[112] R. P. Madden, D. L. Ederer, and K. Codling. Resonances in the photo-ionization continuum of ar i (20-150 ev). *Phys. Rev.*, 177:136–151, 1969.

[113] H. D. Morgan and D. L. Ederer. Photoionization cross section of helium for photon energies 59-67 ev: The (s p, 2 n+) p 0 1 rydberg series of autoionizing resonances. *Phys. Rev. A*, 29(4):1901, 1984.

[114] H. Kossmann, B. Krassig, and V. Schmidt. New determination of beutler-fano parameters for the 3s3p 1p1 resonance in helium. *J. Phys. B: At. Mol. Opt. Phys.*, 21(9):1489, 1988.

[115] N. Berrah, B. Langer, J. Bozek, T. Gorczyca, O. Hemmers, D. W. Lindle, and O. Toader. Angular-distribution parameters and r-matrix calculations of ar resonances. *J. Phys. B*, 29(22):5351, 1996.

[116] S. E. Canton-Rogan, A. A. Wills, T. W. Gorczyca, M. Wiedenhoeft, O. Nayandin, C.-N. Liu, and N. Berrah. Mirroring doubly excited resonances in argon. *Phys. Rev. Lett.*, 85:3113–3116, 2000.

[117] S. Gilbertson, M. Chini, X. Feng, S. Khan, Y. Wu, and Z. Chang. Monitoring and controlling the electron dynamics in helium with isolated attosecond pulses. *Phys. Rev. Lett.*, 105:263003, 2010.

[118] H. Wang, M. Chini, S. Chen, C.-H. Zhang, F. He, Y. Cheng, Y. Wu, U. Thumm, and Z. Chang. Attosecond time-resolved autoionization of argon. *Phys. Rev. Lett.*, 105(14):143002, 2010.

[119] C. Ott, A. Kaldun, P. Raith, K. Meyer, M. Laux, J. Evers, C. H. Keitel, C. H. Greene, and T. Pfeifer. Lorentz meets fano in spectral line shapes: A universal phase and its laser control. *Science*, 340(6133):716–720, 2013.

[120] C. Ott, A. Kaldun, L. Argenti, P. Raith, K. Meyer, M. Laux, Y. Zhang, A. Blättermann, S. Hagstotz, T. Ding, et al. Reconstruction and control of a time-dependent two-electron wave packet. *Nature*, 516(7531):374–378, 2014.

[121] Z. X. Zhao and C. D. Lin. Theory of laser-assisted autoionization by attosecond light pulses. *Phys. Rev. A*, 71:060702, 2005.

[122] C. Bourassin-Bouchet, L. Barreau, J.-F. Gruson, V. abd Hergott, F. Guéré, P. Salières, and T. Ruchon. Quantifying decoherence in attosecond metrology. *accepted in Phys. Rev. X*, 2020.

[123] A. Bärnthaler, S. Rotter, F. Libisch, J. Burgdörfer, S. Gehler, U. Kuhl, and H.-J. Stöckmann. Probing decoherence through fano resonances. *Phys. Rev. Lett.*, 105:056801, 2010.

[124] A. Desrier, A. Maquet, R. Taïeb, and J. Caillat. Ionization dynamics through a fano resonance: Time-domain interpretation of spectral amplitudes. *Physical Review A*, 98(5):053406, 2018.

[125] M. Zürch, H.-T. Chang, L. J. Borja, P. M. Kraus, S. K. Cushing, A. Gandman, C. J. Kaplan, M. H. Oh, J. S. Prell, D. Prendergast, et al. Direct and simultaneous observation of ultrafast electron and hole dynamics in germanium. *Nat. Commun.*, 8(1):1–11, 2017.

[126] J. Dehmer, D. Dill, and S. Wallace. Shape-resonance-enhanced nuclear-motion effects in molecular photoionization. *Physical Review Letters*, 43(14):1005, 1979.

[127] U. Becker, D. Szostak, H. Kerkhoff, M. Kupsch, B. Langer, R. Wehlitz, A. Yagishita, and T. Hayaishi. Subshell photoionization of xe between 40 and 1000 ev. *Physical Review A*, 39(8):3902, 1989.

[128] Ž. Crljen and G. Wendin. Many-body theory of effective local potentials for electronic excitations. iii. application to giant dipole resonances. *Phys. Rev. A*, 35:1571–1581, 1987.

[129] K. T. Cheng and W. R. Johnson. Orbital collapse and the photoionization of the inner $4d$ shells for xe-like ions. *Phys. Rev. A*, 28:2820–2828, 1983.

[130] S. A. Aseyev, Y. Ni, L. J. Frasinski, H. G. Muller, and M. J. J. Vrakking. Attosecond Angle-Resolved Photoelectron Spectroscopy. *Phys. Rev. Lett.*, 91:223902, 2003.

[131] I. Ivanov and A. Kheifets. Angle-dependent time delay in two-color xuv+ ir photoemission of he and ne. *Physical Review A*, 96(1):013408, 2017.

[132] A. W. Bray, F. Naseem, and A. S. Kheifets. Simulation of angular-resolved rabbitt measurements in noble-gas atoms. *Physical Review A*, 97(6):063404, 2018.

[133] P. Hockett. Angle-resolved rabbitt: theory and numerics. *J. Phys. B: At. Mol. Opt. Phys.*, 50(15):154002, 2017.

[134] D. Villeneuve, P. Hockett, M. Vrakking, and H. Niikura. Coherent imaging of an attosecond electron wave packet. *Science*, 356(6343):1150–1153, 2017.

[135] E. Arnous, S. Klarsfeld, and S. Wane. Angular distribution in the two-quantum atomic photoeffect. *Phys. Rev. A*, 7:1559–1568, 1973.

[136] S. H. Southworth, A. C. Parr, J. E. Hardis, J. L. Dehmer, and D. M. Holland. Calibration of a monochromator/spectrometer system for the measurement of photoelectron angular distributions and branching ratios. *Nuclear Instruments and Methods in Physics Research Section A: Accelerators, Spectrometers, Detectors and Associated Equipment*, 246(1-3):782–786, 1986.

[137] T. Carette, J. Dahlström, L. Argenti, and E. Lindroth. Multiconfigurational hartree-fock close-coupling ansatz: Application to the argon photoionization cross section and delays. *Phys. Rev. A*, 87(2):023420, 2013.

[138] A. Maquet and R. Taïeb. Two-colour ir+ xuv spectroscopies: the soft-photon approximation. *Journal of Modern Optics*, 54(13-15):1847–1857, 2007.

[139] D. Smithey, M. Beck, J. Cooper, M. Raymer, and A. Faridani. Complete experimental characterization of the quantum state of a light mode via the wigner function and the density matrix: application to quantum phase distributions of vacuum and squeezed-vacuum states. *Physica Scripta*, 1993(T48):35, 1993.

[140] A. I. Lvovsky and M. G. Raymer. Continuous-variable optical quantum-state tomography. *Rev. Mod. Phys.*, 81:299–332, 2009.

[141] P. Hamm and M. Zanni. *Concepts and methods of 2D infrared spectroscopy*. Cambridge University Press, 2011.

[142] S. Yan and H.-S. Tan. Phase cycling schemes for two-dimensional optical spectroscopy with a pump–probe beam geometry. *Chemical Physics*, 360(1-3):110–115, 2009.

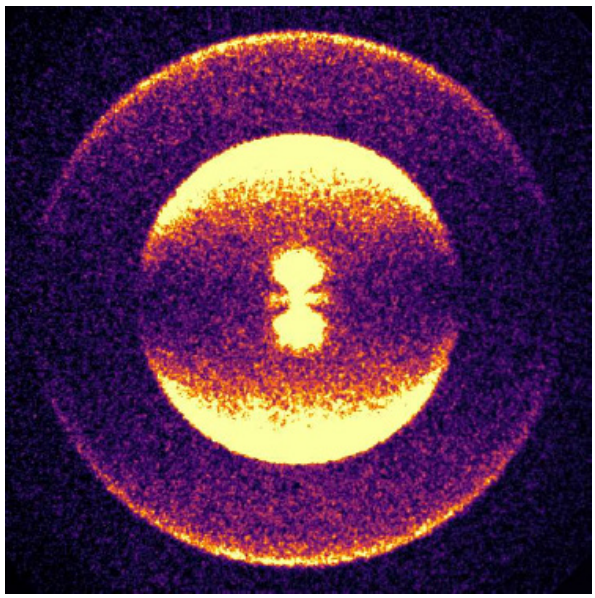

Printed by Media-Tryck, Lund 2020 NORDIC SWAN ECOLABEL 3041 0903

Lund University
Faculty of Engineering
Department of Physics
ISBN 978-91-7895-559-6
ISSN 0281-2762
Lund Reports on Atomic Physics, LRAP 565 (2020)